Contents

Preface

Before the discovery of τ lepton in 1975, physicists already thought about a heavy lepton, l, in a sequential series of $e, \mu, l \ldots$. The calculation of the partial and total decay rates of l for various values of M_l was done by Y.-S. Tsai in 1971 [1]. Tsai's work was realized in the heavy lepton search of the MARK I collaboration, started in 1973, at SPEAR in Stanford. In the MARK I detector, one of the first large-solid-angle general purpose detectors built for colliders, the third lepton, named as τ, was discovered in 1975 by observing $e\mu$ events from e^+e^- annihilation [2].

After the discovery of the τ, the DASP experiment at the DORIS e^+e^- storage ring and the DELCO experiment at SPEAR reported the tau mass, $m_\tau = 1807 \pm 20\mathrm{MeV/c^2}$ and $m_\tau = 1782^{+2}_{-7}\mathrm{MeV/c^2}$, respectively [9] [10]. Due to its large mass, now known to 10^{-4} precision ($m_\tau = 1771.1^{+0.4}_{-0.5}\mathrm{MeV/c^2}$), the tau is the only lepton decaying into hadrons as well as into leptons.

From the end of the 1970's τ was studied at higher energies, at the PETRA e^+e^- collider at DESY, at the PEP collider at SLAC. In the 1980's experiments at PETRA [1] and at PEP [2] reported a number of results on τ properties. More extensive studies on τ lepton were followed by the ARGUS and Crystal Ball experiments at DORIS II, by the MARK III experiment at SPEAR, by the CLEO and CLEO II experiments at CESR, by the experiments[3] at TRISTAN, by the MARK II and SLD experiments at SLC, also, from BES at the BEPC storage ring.

The most energetic ($\sim$ 45 GeV) tau pairs up to now, which are emitted via $e^+e^- \rightarrow$

[1] CELLO, JADE, MARK-J, PLUTO and TASSO

[2] DELCO, HRS, MAC, MARK II and TPC

[3] AMY, TOPAZ, and VENUS

$Z^0 \to \tau^+\tau^-$, have been studied by the 4 experiments [4] of LEP at CERN. LEP which was built for electroweak studies provides also excellent environment for tau physics because it gives high efficiency ($\sim 78\%$) and high purity ($\sim 99\%$) τ samples.

The τ events with energy above threshold allow the measurement of the tau lifetime. The first published measurement showed meaningful non-zero lifetime, $\tau_\tau = 4.6 \pm 1.9 \times 10^{-13} sec$ [16]. A number of τ lifetime measurements were followed by the MAC experiment, by the CELLO experiment, etc. [18] [19]. Since 1990, precise measurements of the τ lifetime have been reported by LEP experiments with the appearance of *vertex detectors*.

The precise measurement of the τ lifetime yields an important result together with τ lepton branching ratio and τ mass when the value is compared with the muon lifetime. The lifetime measurement allows a direct test of the lepton universality ($g_e = g_\mu = g_\tau$) by checking the standard model expectation, $(g_\tau/g_\mu)^2 = (\tau_\mu/\tau_\tau)(m_\mu/m_\tau)^5 B_e$. Tau physics, as a tool for checking the standard model, needs a precise lifetime measurement since the uncertainty of the test is limited ($\sim 60\%$ of total uncertainty) by the precision of τ_τ ($\sim 0.6\%$), compared with B_l ($\sim 0.3\%$) and m_τ ($\sim 0.03\%$) according to a recent summary report [67].

This thesis, named *"Precise measurement of tau lifetime in ALEPH experiment at LEP"*, was started in 1992 with the excellent experimental conditions in the ALEPH Collaboration and presents a new technique for the tau lifetime measurement. It is shown that the new method is one of the most promising techniques due to its stability against systematic uncertainties and self-calibrating characteristics.

The outline of this thesis is as follows: Chapter 1 is dedicated to a brief description of the standard model and the theoretical view of τ lepton physics as well as the status of experimental results on the tau properties. Chapter 2 is devoted to a simple description of the performances of the ALEPH detector with the emphasis on the tracking of the charged particle and the granularity of the calorimeters. Some utilities for the τ physics in the ALEPH experiment are introduced and their algorithms are explained with their performances and efficiencies in chapter 3.

The motivation for the development of a new method is explained in Part II. Chapter 4 will introduce various methods for the tau lifetime measurement from a methodological

[4] ALEPH, DELPHI, L3, and OPAL

point of view. Chapter 5 introduces new notations to treat the kinematics of the hadronic tau decay event and shows a new way to determine the tau direction, by-product of this thesis.

Part III is the core of this thesis. The new method, named as 3DIP, to measure tau lifetime will be developed in Chapter 6. Chapter 7, "Event Selection", contains detector-dependent technical tricks to apply this new technique to the ALEPH data. Many new algorithms and cuts are introduced in this chapter because this new method is realized in 3-dimensional space and only in the hadronic-hadronic $\tau^+\tau^-$ decay events. The result and the systematic uncertainty of the τ lifetime measurement using this method are given in chapter 8. Also some checks of the method and the statistical correlations with other methods appear in that chapter. Finally, this thesis will end in chapter 9 with a new tau lifetime result and with the summary of the advantages and the prospects of the 3DIP method.

Part I

TAU PHYSICS AND ALEPH

Chapter 1

The τ Lepton in the Standard Model

Nature seems to be governed by four kinds of interactions: strong, electromagnetic, weak and gravitational. A principal achievement of physics is the discovery of symmetry principle: invariance under transformation, *i.e. symmetry*, leads to corresponding conserved physical quantity, *e.g.* symmetries under time, translation, and rotation, yield conservations of energy, momentum, and angular momentum, respectively. Invariance under a gauge transformation, we say "gauge" symmetry, gives its corresponding conserved current and introduces a gauge field. Electromagnetic interaction is successfully described by a gauge theory where charged particles interact via a gauge boson (photon). Furthermore, the electromagnetic and weak interactions are described by a gauge theory based on $SU(2)_L \times U(1)_Y$ and unified into the same theoretical formalism: 3 weak gauge bosons ($W^{\pm}, Z^0$) are introduced as well as photon.

Force	Gauge Boson	Symbol	Charge (e)	Spin	Mass (GeV)
Strong	gluon	g	0	1	0
Electromagnetic	photon	γ	0	1	0
Weak	$W^{\pm}$ boson	$W^{\pm}$	± 1	1	80.2
	Z^0 boson	Z^0	0	1	91.2
Gravitational	graviton	G	0	2	0

Table 1.1: Fundamental interactions and gauge bosons

The present belief is that the 4 kinds of interactions may be described by the *gauge theory* using higher level of internal symmetry. Tab. 1.1 shows the 4 kinds of fundamental interactions and the properties of their gauge bosons.

In this chapter we will give an outline of the standard model of electroweak interaction and introduce some tests of the model using the tau decays. In addition, the tau properties, m_τ, τ_τ, and $B(\tau \to X\bar{\nu})$, and a simple description of each measurement are given. Finally, one of the crucial points in the Standard Model, *lepton universality*, will be discussed.

1.1 Outline of the standard model

1.1.1 Electroweak interaction

Gauge theory of electromagnetic interaction

Quantum electrodynamics (QED) is the first renormalizable quantum field theory. To ensure charge conservation, the Lagrangian is requested to be invariant under the local phase transformation of particle field $\psi(x)$ (gauge transformation)

$$\psi(x) \to e^{-ie\alpha(x)Q}\psi(x)$$

where $\alpha(x)$ is an arbitrary function and Qe the charge of the particle. The phase transformation $e^{-ie\alpha(x)Q}$ belongs to the symmetry group $U(1)$. The Lagrangian describing a free Dirac particle, $\bar{\psi}(i\gamma^\mu\partial_\mu - m)\psi$, is not invariant under this phase transformation. Its invariance is achieved by introducing a gauge field A_μ which transforms as

$$A_\mu(x) \to A_\mu(x) + \partial_\mu\alpha(x)$$

Then the full invariant Lagrangian is written as

$$\mathcal{L} = -\frac{1}{4}F^{\mu\nu}F_{\mu\nu} + \bar{\psi}(i\gamma^\mu\partial_\mu - m)\psi - e\bar{\psi}\gamma^\mu Q\psi A_\mu$$

where $-\frac{1}{4}F^{\mu\nu}F_{\mu\nu}$ represents the kinematic energy of A_μ ($F_{\mu\nu} = \partial_\mu A_\nu - \partial_\nu A_\mu$). The third term, $-e\bar{\psi}\gamma^\mu Q\psi A_\mu$, in the Lagrangian describes the interaction between the particle and the gauge field. $\bar{\psi}\gamma^\mu Q\psi$ is the conserved electromagnetic current (J^μ_{em}) and e is the coupling between this current J^μ_{em} and the gauge field A_μ.

Gauge theory of electroweak interaction

The generalization of QED to other interactions can be done by looking for other symmetry groups. Low energy weak processes, such as β decay, are well described by the Fermi's current-current interaction where the V-A structure of the weak current ensures parity violation. To preserve these results, the basic assumption of a gauge theory is the existentce of a conserved weak isospin. Left-handed fermions form isospin doublets, ψ_L. One thus requests the Lagrangian be invariant under the transformation

$$\psi_L(x) \to e^{-ig\boldsymbol{\alpha}(x)\cdot\boldsymbol{T}}\psi_L(x)$$

where the constant g corresponds to e in QED and $\boldsymbol{T}$ is the weak isospin operator corresponding to the charge operator Q: the transformation belongs to the symmetry group $SU(2)$. Three massless gauge bosons, W^1, W^2, and W^3, arise by gauge invariance with coupling g. However, this simple approach for the weak interaction was found not to be renormalizable.

The electromagnetic and weak interactions were unified as the $SU(2)_L \times U(1)_Y$ symmetry group by Glashow, Weinberg and Salam in the 1960s. The Glashow-Weinberg-Salam (GWS) theory is based on the invariance under the different gauge transformations for the left-handed and right-handed fermions:

$$\begin{aligned}\psi_L &\to e^{-ig\boldsymbol{\alpha}(x)\cdot\boldsymbol{T}-ig'\beta(x)Y/2}\psi_L \\ \psi_R &\to e^{-ig'\beta(x)Y/2}\psi_R\end{aligned}$$

where two couplings g and g' arise from $SU(2)_L$ and $U(1)_Y$ groups. The left-handed fermions and right-handed fermions form isospin-doublets and isospin singlets, respectively:

$$\begin{aligned}\psi_L &= \begin{pmatrix}\psi_{\nu_e,\nu_\mu,\nu_\tau} \\ \psi_{e,\mu,\tau}\end{pmatrix}_L, \begin{pmatrix}\psi_{u,c,t} \\ \psi_{d,s,b}\end{pmatrix}_L \\ \psi_R &= (\psi_{e,\mu,\tau})_R,\ (\psi_{u,c,t})_R \text{ or } (\psi_{d,b,s})_R\end{aligned}$$

Invariance requests four massless gauge bosons, $W^{1,2,3}$ from $SU(2)$ and B from $U(1)$, and makes the Lagrangian contain the interaction terms:

$$\begin{aligned}-ig\boldsymbol{J}^\mu\cdot\boldsymbol{W}_\mu \equiv &\ -ig\bar{\psi}_L\gamma^\mu\boldsymbol{T}\cdot\boldsymbol{W}_\mu\psi_L && \text{for left handed fermions} \\ -i\frac{g'}{2}j_Y^\mu B_\mu \equiv &\ -ig'\bar{\psi}\gamma^\mu\tfrac{Y}{2}\psi B_\mu && \text{for left or right handed fermions}\end{aligned}$$

Since we know that weak interactions are meditated by massive bosons, and the electromagnetic interaction is by the massless photon, it is necessary to find a way to give masses to the gauge bosons without loosing renormalizability. This is done by the Higgs mechanism : when introducing an adequate potential using a complex scalar field doublet(Higgs field), symmetry breaking provides the mechanism giving masses to the bosons through their couplings to the scalar field. This results in 3 massive gauge boson fields

$$\begin{aligned} W^{\pm} &= \frac{1}{\sqrt{2}}(W^1 \mp iW^2) \\ Z^0 &= W^3 \cos\theta_W - B \sin\theta_W \end{aligned}$$

and one massless gauge boson field (photon),

$$A = W^3 \sin\theta_W + B \cos\theta_W$$

The mixing angle θ_W becomes another parameter of the theory related to the $W^{\pm}$ and Z^0 masses by $\sin\theta_W = M_W/M_Z$.

The Lagrangian describing electroweak interactions expressed in terms of gauge bosons $W^{\pm}$, Z^0, and γ, becomes

$$\begin{aligned} \mathcal{L}_{int} = & \quad -ig\boldsymbol{J}^{\mu} \cdot \boldsymbol{W}_{\mu} - i\tfrac{g'}{2} j_Y^{\mu} B_{\mu} \\ = & \quad -i\tfrac{g}{\sqrt{2}}(J_+^{\mu} W_{\mu}^+ + J_-^{\mu} W_{\mu}^-), \\ & -i(g\cos\theta_W J_3^{\mu} - \tfrac{g'}{2}\sin\theta_W j_Y^{\mu}) Z_{\mu}^0, \\ & -i(g\sin\theta_W J_3^{\mu} + \tfrac{g'}{2}\cos\theta_W j_Y^{\mu}) A_{\mu} \end{aligned}$$

The third term, electromagnetic interaction, is identical to $-iej_{em}^{\mu} A_{\mu}$ where $j_{em}^{\mu} = J_3^{\mu} + j_Y^{\mu}/2$. Therefore,

$$g \sin\theta_W = g' \cos\theta_W = e$$

Then we can express the second term as

$$-i\frac{g}{\cos\theta_W}(J_3^{\mu} - \sin^2\theta_W j_{em}^{\mu}) Z_{\mu}^0$$

and $J_3^{\mu} - \sin^2\theta_W j_{em}^{\mu} (\equiv J_{NC})$ is identified as neutral weak current. Finally,

$$\begin{aligned} \mathcal{L}_{int} = & \ -\tfrac{g}{2\sqrt{2}}\bar{\psi}\gamma^{\mu}(1-\gamma^5)(T^+ W_{\mu}^+ + T^- W_{\mu}^-)\psi, && \text{charged weak interaction part} \\ & -\tfrac{g}{2\cos\theta_W}\bar{\psi}\gamma^{\mu}(g_V - g_A\gamma^5) Z_{\mu}^0 \psi, && \text{neutral weak interaction part} \\ & -e\bar{\psi}\gamma^{\mu} Q A_{\mu}\psi && \text{electromagnetic interaction part} \end{aligned}$$

where $T^{\pm}$ are the weak isospin raising and lowering operators and

$$\begin{aligned} g_V &\equiv T^3 - 2\sin^2\theta_W Q \\ g_A &\equiv T^3 \end{aligned}$$

Hence, the Standard Model of electroweak interaction has three parameters to be determined; the first and second parameters are the gauge coupling constants, g and g', corresponding to the gauge bosons $W^i_\mu, i = 1, 2, 3$, and B_μ for the $SU(2)$ and $U(1)$ parts, respectively, the third one is the $SU(2)$ and $U(1)$ mixing angle $\sin\theta_W$. These parameters, however, are not direct physical observables and therefore 3 following variables are taken instead of g, g', and $\sin\theta_W$:

1 fine structure constant, α : $\alpha(\equiv e^2/4\pi) = \frac{1}{4\pi}\frac{g^2 g'^2}{g^2+g'^2}$.
$\alpha(= 1/137.036)$ was determined from the quantum Hall effect with $\sim 5 \times 10^{-7}$ uncertainty.

2 Fermi constant, G_F : $\sqrt{2}g^2/8M_W^2$.
$G_F(= 1.1664\times10^{-5}\text{GeV}^{-2})$ is determined from the muon lifetime measurement with $\sim 2 \times 10^{-5}$ uncertainty.

3 mass of the Z^0 boson, M_Z : $M_Z(= M_W/\cos\theta_W)$
$M_Z(= 91.187\text{GeV/c}^2)$ is known to $\sim 10^{-4}$ uncertainty.

The weak mixing angle, $\sin^2\theta_W(= 0.2319)$, is determined best from the measurement of M_Z:

$$\sin\theta_W\cos\theta_W = (\frac{\pi\alpha}{\sqrt{2}G_F})^{1/2}/M_Z$$

1.1.2 Universality

Considering the 3 generations of fermions, the Lagrangian describing the interactions of charged weak currents, *i.e.* interactions of particle field doublets (ψ_i) via charged weak bosons ($W^\pm$), is just a sum over the families with coupling g independent of the family:

$$-\frac{g}{\sqrt{2}}\sum_i \bar{\psi}_i\gamma^\mu\frac{1}{2}(1-\gamma^5)(T^+W^+_\mu + T^-W^-_\mu)\psi_i$$

On the other hand the Lagrangian describing the interaction of neutral weak current, *i.e.* via neutral weak boson (Z^0), is

$$-\frac{g}{\cos\theta_W}\sum_i \bar{\psi}_i\gamma^\mu\frac{1}{2}(g_V - g_A\gamma^5)\psi_i Z^0_\mu$$

This *universality* of couplings, a consequence of a unique $SU(2)_L \times U(1)_Y$ gauge group, is a fundamental assumption of the Standard Model.

This prediction can be readily checked experimentally at least in the leptonic part:

$$\begin{aligned} g_e &= g_\mu = g_\tau \\ g_V^e &= g_V^\mu = g_V^\tau (= -\frac{1}{2} + 2\sin^2\theta_W) \\ g_A^e &= g_A^\mu = g_A^\tau (= -\frac{1}{2}) \end{aligned}$$

The universality of g_V and g_A can be checked by the study of *neutral weak interactions*, and the universality of g can be checked by the study of *charged weak interactions*.

g_V and g_A universality check from τ

g_V and g_A universality can be checked by the measurement of the width of the leptonic Z^0 decay (Γ_l) or polarization asymmetries $\mathcal{A}_l$ in LEP experiments. At Z^0 pole, these quantities are related to g_V^l and g_A^l as follows:

$$\begin{aligned} \Gamma_l &= \frac{G_F M_Z^3}{6\sqrt{2}\pi}({g_V^l}^2 + {g_A^l}^2) \\ \mathcal{A}_l &= \frac{2 g_V^l g_A^l}{(g_V^l)^2 + (g_A^l)^2} \end{aligned}$$

where $\mathcal{A}_l$ are deduced from the measurements of charge asymmetries and forward-backward asymmetries of e^+e^-, $\mu^+\mu^-$, and $\tau^+\tau^-$ productions.

Tau events are especially interesting because $\mathcal{A}_\tau$ can be extracted directly from the polarization measurement and in addition $\mathcal{A}_e$ can be measured from the $\mathcal{A}_{FB}^{pol}$. Fig. 1.1 shows four different $\tau\tau$ production states with respect to forward-backward direction and helicity. One can make 3 asymmetries as follows

$$\begin{aligned} P_\tau &\equiv \frac{\sigma(h_\tau > 0) - \sigma(h_\tau < 0)}{\sigma_{total}} = -\mathcal{A}_\tau \\ \mathcal{A}_{FB}^\tau &\equiv \frac{\sigma(\cos\theta_\tau > 0) - \sigma(\cos\theta_\tau < 0)}{\sigma_{total}} = \frac{3}{4}\mathcal{A}_e\mathcal{A}_\tau \\ \mathcal{A}_{FB}^{pol} &\equiv \frac{\sigma(h_\tau\cos\theta_\tau > 0) - \sigma(h_\tau\cos\theta_\tau < 0)}{\sigma_{total}} = -\frac{3}{4}\mathcal{A}_e \end{aligned}$$

Here, we put a superscript τ on $\mathcal{A}_{FB}$ to distinguish from other asymmetries, $\mathcal{A}_{FB}^e$ and $\mathcal{A}_{FB}^\mu$ measured from $Z^0 \to e^+e^-$ and $Z^0 \to \mu^+\mu^-$ events. The measured values by 4 LEP

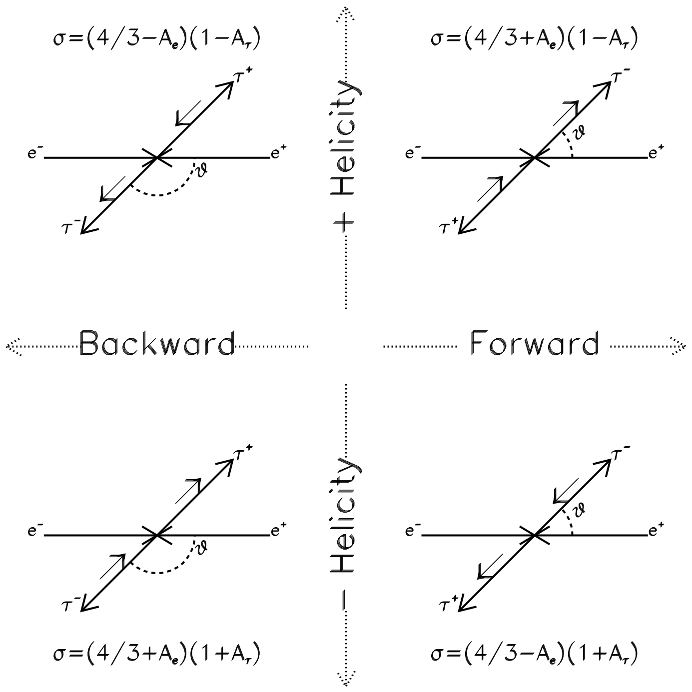

Figure 1.1: $\tau^+\tau^-$ production states. Angles and helicities are defined by the τ^- and e^- directions

experiments of $\mathcal{A}_\tau$ and $\mathcal{A}_e$ are 0.145 ± 0.009 and 0.137 ± 0.011, respectively. The measured $\mathcal{A}^\tau_{FB}$ is 0.0228 ± 0.0026 [7].

Tab. 1.2 shows the current status of the g_V and g_A universality according to all measurements of Γ_l and $\mathcal{A}_l$ done by 4 LEP experiments.

	g_V		g_A	
e	- 0.0370	$\pm$ 0.0021	-0.50093	$\pm$ 0.00064
μ	- 0.0308	$\pm$ 0.0051	-0.50164	$\pm$ 0.00096
τ	- 0.0386	$\pm$ 0.0023	-0.5026	$\pm$ 0.0010
l	- 0.0366	$\pm$ 0.0013	-0.50128	$\pm$ 0.00054

Table 1.2: Current measured values of g_V and g_A by the experiments at LEP

g_l universality checks from τ decay

The g_l universality can be checked also with the tau decays. In particular leptonic tau decays, $\tau \rightarrow e\bar{\nu}_e\nu_\tau$ and $\tau \rightarrow \mu\bar{\nu}_\mu\nu_\tau$, can be directly compared with the muon decay

$\mu \to e\bar{\nu}_e\nu_\mu$ of which properties are very precisely measured:

$$\begin{aligned} m_\mu &= 105.658389 \pm 0.000034\mathrm{MeV/c^2} \\ \tau_\mu &= 2.19703 \pm 0.00004\mu s \end{aligned}$$

Comparison of the tau leptonic decay width, $\Gamma(\tau \to l\nu_l\nu_\tau)$, with the muon decay width, $\Gamma(\mu \to e\bar{\nu}_e\nu_\mu)$, provides a check of the lepton universality in the charged current sector. We will discuss the universality test in detail in the next section.

1.2 Lepton universality check from τ leptonic decay

Fig. 1.2 shows the Feynman diagram for tau decay to electron. The invariant amplitude

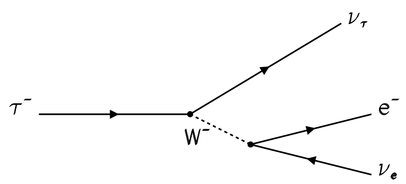

Figure 1.2: Feynman diagram for tau decay to electron

for tau decay to electron mediated by a W^- boson is expressed as

$$\mathcal{M} = [\frac{g_\tau}{2\sqrt{2}}\bar{u}(\nu_\tau)\gamma^\mu(1-\gamma^5)u(\tau)]\frac{1}{M_W^2}[\frac{g_e}{2\sqrt{2}}\bar{u}(e)\gamma_\mu(1-\gamma^5)v(\nu_e)]$$

where $q^\mu q^\nu/M_W^2$ and q^2 contributions are omitted since both terms are negligible, $\sim 10^{-4}$. Identifying this equation with its classical Fermi's expression,

$$\mathcal{M} = \frac{G_F}{\sqrt{2}}J^\mu(\tau)J_\mu(e)$$

one gets $g_e g_\tau/2M_W^2 = 4G_F/\sqrt{2}$. We will denote Fermi constant G_F as G_τ in order to insist that this constant comes from the tau decay.

The tau-to-electron decay width, $\Gamma(\tau \to e\bar{\nu}_e\nu_\tau)$, is then,

$$d\Gamma = \frac{1}{2E}\overline{|\mathcal{M}|^2}\frac{d^3p_e}{(2\pi)^3 2E_e}\frac{d^3p_{\nu_e}}{(2\pi)^3 2E_{\nu_e}}\frac{d^3p_{\nu_\tau}}{(2\pi)^3 2E_{\nu_\tau}}(2\pi)^4\delta^{(4)}(p_T - p_e - p_{\nu_e} - p_{\nu_\tau})$$

where $\overline{|\mathcal{M}|^2}$ is the spin-averaged probability. Neglecting the electron mass ($\sim 0.0003 m_\tau$), the decay rate is

$$\Gamma(\tau \to e\bar{\nu}_e\nu_\tau) = \frac{G_\tau^2 m_T^5}{192\pi^3} = \frac{g_e^2 g_\tau^2}{192\pi^3}\frac{m_T^5}{32M_W^4} \tag{1.1}$$

For the tau decay to muon, since muon mass is not negligible anymore ($\sim 0.06 m_\tau$), the mass correction term is needed.

$$\Gamma(\tau \to \mu\bar{\nu}_\mu\nu_\tau) = \frac{G_\tau^2 m_T^5}{192\pi^3}(1 - 8y + 8y^2 - y^4 - 12y^2 \ln y) \tag{1.2}$$

where $y \equiv (m_\mu/m_\tau)^2$. This mass correction, $F(y) \equiv 1-8y+8y^2-y^4-12y^2 \ln y$, is negligible for the tau to electron decay, but not for the tau to muon decay ($F(m_\mu^2/m_T^2) \sim 0.973$).

More generally, the leptonic decay width of the tau can be expressed as follows considering the W mass effect and the radiative corrections:

$$\Gamma(\tau \to l\nu_l\nu_\tau) = \frac{G_\tau^2 m_\tau^5}{192\pi^3} F(\frac{m_l^2}{m_\tau^2})[1 + \frac{3}{5}\frac{m_\tau^2}{M_W^2}][1 + \frac{\alpha(m_\tau)}{2\pi}(\frac{25}{4} - \pi^2)] \tag{1.3}$$

where $\alpha^{-1}(m_\tau) \cong 133.3$ and the corrections in the brackets have 0.03% and 0.4% effects respectively. For simplicity, we will replace all the correction terms with a constant $C_{l\tau}$.

$$C_{l\tau} \equiv F(\frac{m_l^2}{m_\tau^2})[1 + \frac{3}{5}\frac{m_\tau^2}{M_W^2}][1 + \frac{\alpha(m_\tau)}{2\pi}(\frac{25}{4} - \pi^2)]$$

We find $C_{e\tau} = 0.996$, $C_{\mu\tau} = 0.969$.

By the definitions of the electron and muon branching ratios,

$$\begin{aligned} B_e &\equiv \frac{\Gamma(\tau \to e\bar{\nu}_e\nu_\tau)}{\Gamma_{tot}} \\ B_\mu &\equiv \frac{\Gamma(\tau \to \mu\bar{\nu}_\mu\nu_\tau)}{\Gamma_{tot}} \end{aligned}$$

the tau lifetime is therefore related to the leptonic branching ratios as follow

$$\begin{aligned} \tau_\tau &= \frac{1}{\Gamma_{tot}} \times \hbar \\ &= \frac{Be}{\Gamma(\tau \to e\bar{\nu}_e\nu_\tau)} \quad (= \frac{B\mu}{\Gamma(\tau \to \mu\bar{\nu}_\mu\nu_\tau)}) \times \hbar \\ &= (\frac{G_\tau^2 m_\tau^5}{192\pi^3})^{-1} C_{e\tau}^{-1} Be \times \hbar \end{aligned}$$

where $\hbar = 6.5821 \times 10^{-25}$ GeV s.

On the other hand, since $B(\mu \to e\bar{\nu}_e\nu_\mu) = 100\%$, the muon lifetime is

$$\tau_\mu = (\frac{G_\mu^2 m_\mu^5}{192\pi^3})^{-1} C_{e\mu}^{-1} \times \hbar$$

where $G_\mu = \sqrt{2} g_\mu g_e / 8M_W^2$ and $C_{e\mu} \sim 0.9956$.

Combining τ_τ and τ_μ,

$$(\frac{G_\tau}{G_\mu})^2 = (\frac{g_\tau}{g_\mu})^2 = (\frac{\tau_\mu}{\tau_\tau})(\frac{m_\mu}{m_\tau})^5 B(\tau \to e\bar{\nu}_e\nu_\tau) \tag{1.4}$$

where g_e terms in both G_τ and G_μ cancel out, the correction term $(C_{e\mu}/C_{e\tau})$ is negligible (~ 0.9996).

Using the events $\tau \to \mu\nu\nu$ we can deduce the same equation for (g_τ/g_e):

$$(\frac{g_\tau}{g_e})^2 = (\frac{\tau_\mu}{\tau_\tau})(\frac{m_\mu}{m_\tau})^5 B(\tau \to \mu\bar{\nu}_\mu\nu_\tau)(\frac{C_{e\mu}}{C_{\mu\tau}}) \tag{1.5}$$

where $\frac{C_{e\mu}}{C_{\mu\tau}} \sim 1.0277$.

We will discuss the check of the lepton universality based on above equations with the experimental results on m_τ, τ_τ, and $B_e(B_\mu)$, in the following sections.

1.3 Experimental properties of τ lepton

After the discovery of the tau lepton, its properties have been studied by many experiments. When we started this thesis, it seemed that tau made some puzzles as if it were not *standard*: 1-prong problem, non-universal coupling G_τ [14] [15]. Tau physics has been studied extensively and precision measurements of tau properties, now available, may give the answers.

We summarize here the experimental properties of τ lepton, m_τ, branching fractions, and lifetime, at the time we started the thesis (1992). This discussion will be continued in Chap. 9 with the new results in LEP experiments including the analysis of this thesis.

1.3.1 Tau mass : m_τ

There are two general approaches to measure the tau mass:

- scanning threshold: searching the minimum beam energy to produce tau pairs at e^+e^- collider.

- pseudo τ mass fit: fitting the tau pseudomass (because tau mass can not be directly measured from the reconstructed particles due to the missing 4 momenta of neutrino) with the assumption that the tau direction is parallel to the multi-pions (denote "h") direction. The pseudo tau momentum, $|p^*_\tau|$, is $|p_h| + |p_{\nu_\tau}|$. Using $E_{\nu_\tau} = E_\mathcal{T} - E_h$, the tau pseudo mass

$$(m^*_\tau)^2 = 2(E_\tau - E_h)(E_h - |\vec{p}_h|) + m_h^2$$

where E_τ is the beam energy. One gets the tau mass from the characteristic sharp edge of the pseudomass distribution [8].

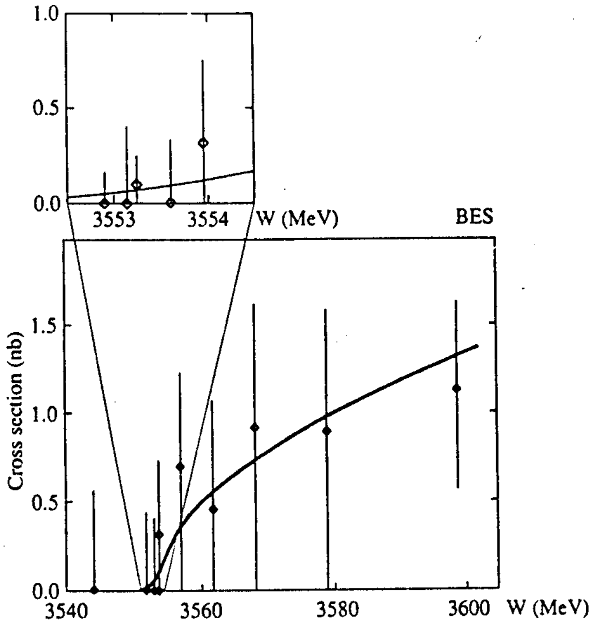

Figure 1.3: cross section $\sigma(e^+e^- \to \tau^+\tau^-)$ around threshold in BES experiment.

The world average $1784.1^{+2.7}_{-3.6}$MeV/c^2 dominated by the DELCO measurement [1] was outdated by the precise measurement of BES collaboration in 1992 [11]. The BES measurement was done by fitting $\sigma(e^+e^- \to \tau^+\tau^-)$ near threshold using 7 $e^\pm\mu^\mp$ events, Fig. 1.3 The tau mass determined by BES is $1776.9^{+0.4}_{-0.5} \pm 0.2$ MeV.

[1] DELCO measurement was done by scanning the threshold using 346 $e^\pm X^\mp$ events produced by e^+e^- collisions in 1978.

The two measurements from ARGUS and CLEO in 1992 agree with the BES results: $m_\tau^{ARGUS} = 1776.3 \pm 2.4 \pm 1.4 \mathrm{MeV/c^2}$ from mass fit using $\tau \to 3\pi\nu_\tau$ assuming $m_\nu = 0$, $m_\tau^{CLEO} = 1777.6 \pm 0.9 \pm 1.5 \mathrm{MeV/c^2}$ from kinematics using 1-1 topology events with π^0s.

The new values agree with each other and give the corrected world average:

$$m_\tau = 1777.1 \pm 0.5 \mathrm{MeV/c^2}$$

The uncertainty on the tau mass is about 3×10^{-4}. Fig. 1.4 shows the measurements of the tau mass.

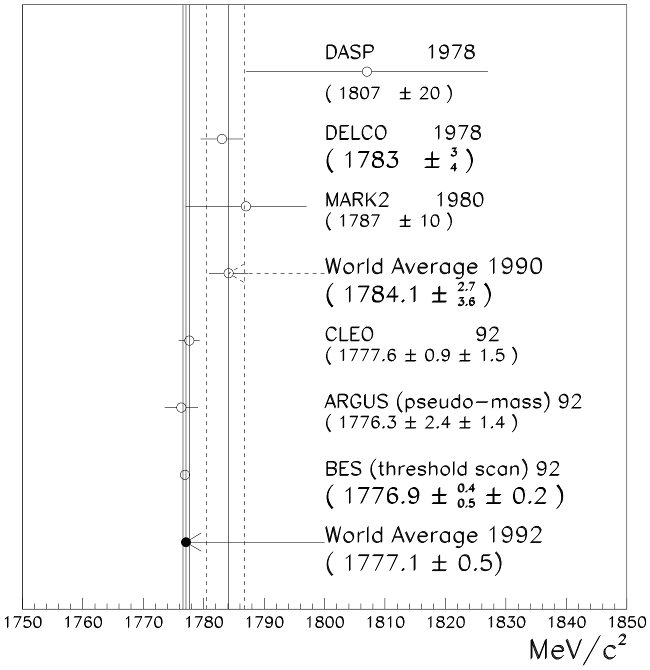

Figure 1.4: Tau mass measurements

1.3.2 Tau branching ratios : $B.R.(\tau \to X\nu_\tau)$

Unlike the muon, the tau lepton can decay to hadrons as well as to electron or muon due to its large mass. About 85 % of taus decay to 1 charged track, $e, \mu, \pi, \rho(\to \pi\pi^0), a_1(\to \rho\pi^0), \pi + n\pi^0$. 15% decay to 3 charged tracks, $a_1(\to 3\pi), 3\pi + n\pi^0$. The branching fraction to 5 prong and other modes is only about 0.1 %.

Tab. 1.3 shows the tau branching ratios for important decay modes using the data collected up to 1992 [22].

Decay Mode	$B.R.^{WA}$ (%)
e	17.76 ± 0.15
μ	17.53 ± 0.19
h	12.79 ± 0.29
$+\pi^0$	25.53 ± 0.31
$+2\pi^0$	8.86 ± 0.32
$+\geq 3\pi^0$	1.26 ± 0.14
$3h$	8.62 ± 0.19
$+\geq 1\pi^0$	5.45 ± 0.22
$5h \geq 0\pi^0$	0.13 ± 0.03

Table 1.3: Tau branching ratios

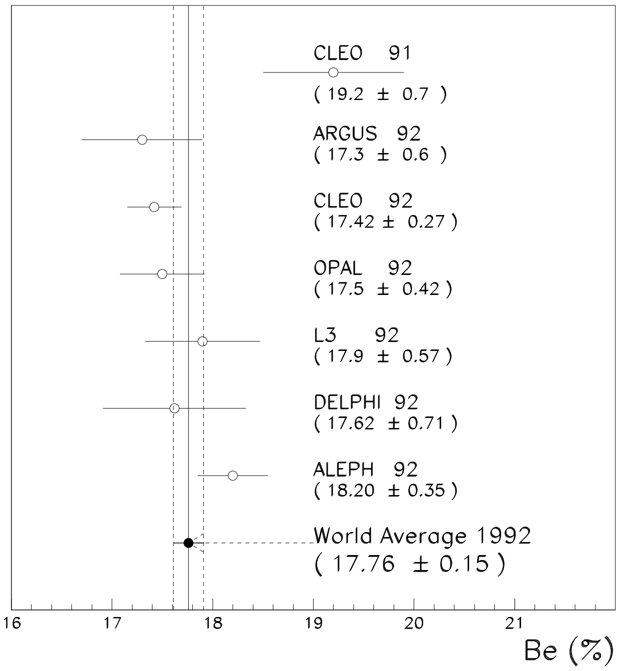

Figure 1.5: Tau electron branching ratio measurements: errors are the combined uncertainty of statistic and systematic

Tau leptonic branching ratio is especially interesting since it gives a tool to check lepton universality when it is combined with the tau lifetime measurement as seen in the previous section.

Fig. 1.5 shows the measurements of the electron branching ratio. The combined result is

$$B(\tau \to e\nu\bar{\nu}) = 17.76 \pm 0.15\% \tag{1.6}$$

For the muon decays, the measured branching fraction is

$$B(\tau \to \mu\nu\bar{\nu}) = 17.53 \pm 0.19\% \tag{1.7}$$

The ratio $B_\mu/B_e = 0.987 \pm 0.014$ is consistent with $C_{\mu\tau}/C_{e\tau} \sim 0.973$.

1.3.3 Tau lifetime : τ_τ

The τ lifetime is measured from the observed decay length, extracted from the *tau production position* (approximated to the beam position) and either of two tracking informations: the *tau decay vertex* (reconstructed common vertex of the tau decay products) or the *impact parameter* (transverse decay length in the xy plane). We will describe the methods in detail in Chap. 4.

The τ lifetime was first measured in 1982 by the MARK II collaboration with $\tau_\tau = (4.6 \pm 1.9) \times 10^{-13}$ sec [16]. A number of τ lifetime measurements have been done by the MAC experiment [18], by the CELLO experiment [19], etc.. Fig. 1.6 shows the 7 lifetime measurements and the world average before the LEP starting.

The precise measurements of the τ lifetime have been reported from the starting of experiments, like LEP experiments, in which the tracking resolution is much improved with the appearance of *vertex detectors*. Also, many new techniques have been developed in the meanwhile, and have produced statistically and/or systematically precise results. These new techniques will also be introduced in Chap. 4.

Fig. 1.7 shows the tau lifetime measurements after the LEP start.

The significant change of the tau mass by the BES measurement tells all measurements before 1992 had had a bias of $\sim 1.2fs$. The world average from combining all the experiments up to 1992 is with mass correction:

$$\tau_\tau = 295.7 \pm 3.2\text{fs}$$

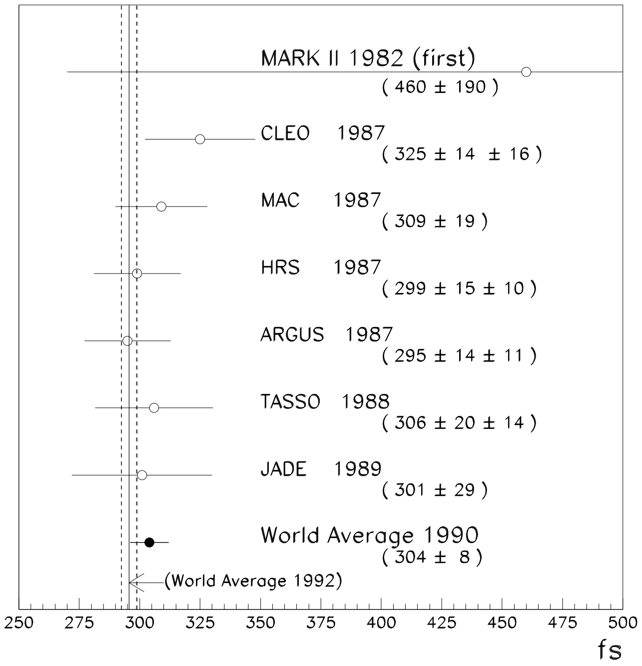

Figure 1.6: τ lifetime measurements before LEP starting and the world average in 1990. Measurements are plotted according to the order of time.

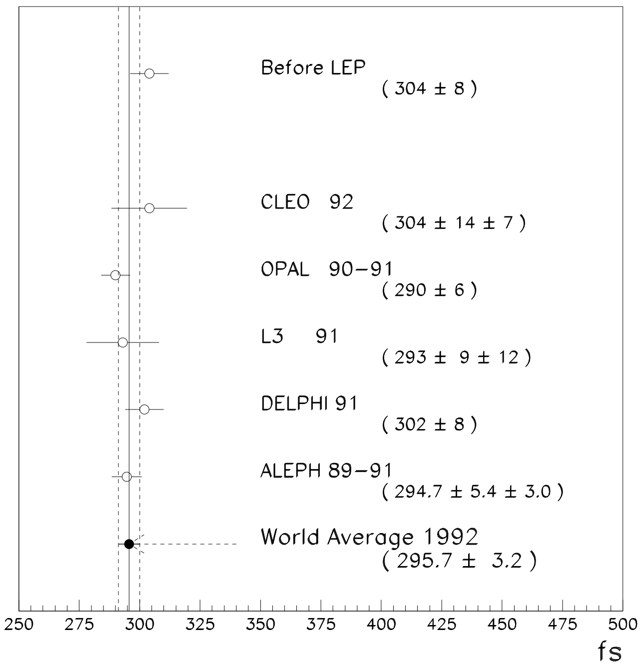

Figure 1.7: τ lifetime measurements after the LEP start.

1.4 Status of the lepton universality

Let us recall Eq.1.4.

$$(\frac{G_\tau}{G_\mu})^2 = (\frac{g_\tau}{g_\mu})^2 = (\frac{\tau_\mu}{\tau_\tau})(\frac{m_\mu}{m_\tau})^5 B(\tau \to e\bar{\nu}_e\nu_\tau)$$

With the old values of $m_\tau(= 1.7841\text{GeV/c}^2)$, $\tau_\tau(= 304\text{fs})$, and $B_e(= 17.93\%)$, one had

$$(\frac{g_\tau}{g_\mu}) = 0.972 \pm 0.016$$

which gave a 1.8 σ deviation from universality.

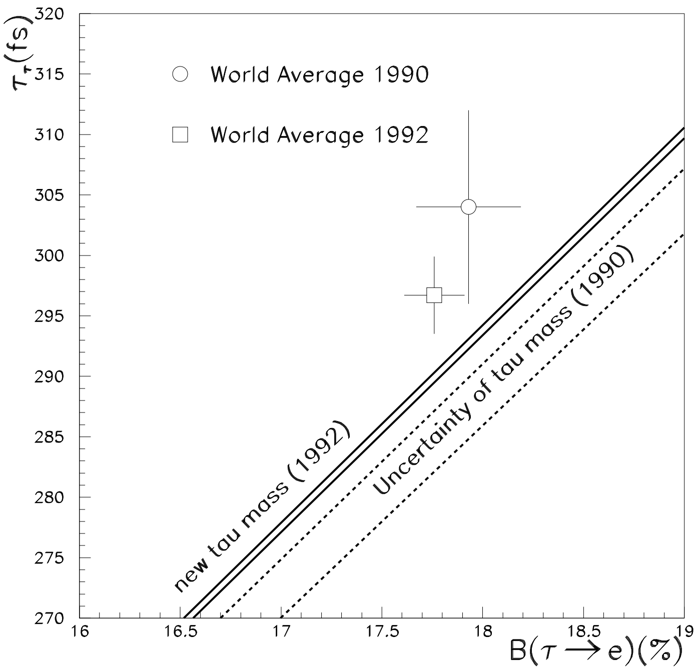

Figure 1.8: Status of lepton universality checks from τ decay in 1992.

Fig. 1.8 shows the status of the universality in 1990 and 1992. The new measurements of $m_\tau(= 1.7771 \pm 0.5\text{GeV/c}^2)$, $\tau_\tau(= 295.7 \pm 3.2\text{fs})$, and $B_e(= 17.76 \pm 0.15\%)$, in 1992 yield:

$$(\frac{g_\tau}{g_\mu})^2 = 0.9803 \pm 0.0108(\tau_\tau) \pm 0.0014(m_\tau) \pm 0.0084(B_e)$$

where the errors are separately quoted in order to show the source. The uncertainty on the tau lifetime measurement (0.0108) is the main contribution in the lepton universality check. The result:

$$(\frac{g_\tau}{g_\mu}) = 0.990 \pm 0.007$$

still shows 1.4 σ deviation from lepton universality.

However, if one uses the tau to muon branching ratio, $B_\mu = 17.53 \pm 0.19\%$, then

$$(\frac{g_\tau}{g_e}) = 0.997 \pm 0.008$$

which fairly agrees with lepton universality.

The largest contribution in the uncertainty of the check comes from the measurements of the lifetime and the leptonic branching ratio: $\sigma_{\tau_\tau}/\tau_\tau \sim 1.1\%$ and $\sigma_{B_l}/B_l \sim 0.8\%$. For the latter, the error is still dominated by statistics. Therefore, as data increase the uncertainty on B_l should decrease. On the other hand, the lifetime measurement may less benefit from the increasing statistics than B_l measurement since the precision is directly related to the detector resolution and suffers from difficult systematic control. A precise and systematic free method to measure the tau lifetime is mandatory to check lepton universality.

To break through the limitation on the lifetime uncertainty, especially on the systematic error, one can simply think about a high performance detector or a new method less affected by the detector resolution. The precise measurement of the tau lifetime by a new technique is the main motivation of this thesis. We will discuss again the universality check in the last chapter with the new measurements of tau leptonic branching ratio and tau lifetime including the result of this thesis.

Chapter 2

Performances of the ALEPH Detector

The present work is based on τ data taken with the ALEPH detector at the LEP ring. The LEP, Large Electron and Positron storage ring, is a collider built especially for the measurements of various electroweak parameters (Fig. 2.1). LEP was started in 1989

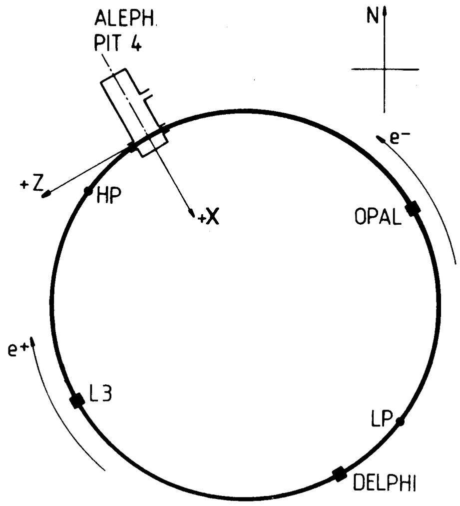

Figure 2.1: LEP ring and 4 points of interaction. The circumference of LEP is about 27 km.

with the center of mass energy around 91 GeV, the energy corresponding to the Z^0 boson mass.

This chapter describes the characteristics of the ALEPH detector and its performances.

Overall descriptions of the detector components are in Sec. 2.1. The details of the detector can be found elsewhere [23] [25] [26].

The tau lifetime measurement depends mainly on the tracking resolution of the detector. Especially in this thesis, since 3-dimensional tracking is needed to carry out the new method (3DIP), the tracking performance on z component (along the beam axis) is emphasized as well as $r\phi$ component (in Sec. 2.2). The performances of the calorimeters, ECAL and HCAL, play also an important role in the energy and direction measurement of the neutrals and will be described in some details in Sec. 2.3.

2.1 Overall structure and components

Fig. 2.2 shows the overall view of the ALEPH detector.

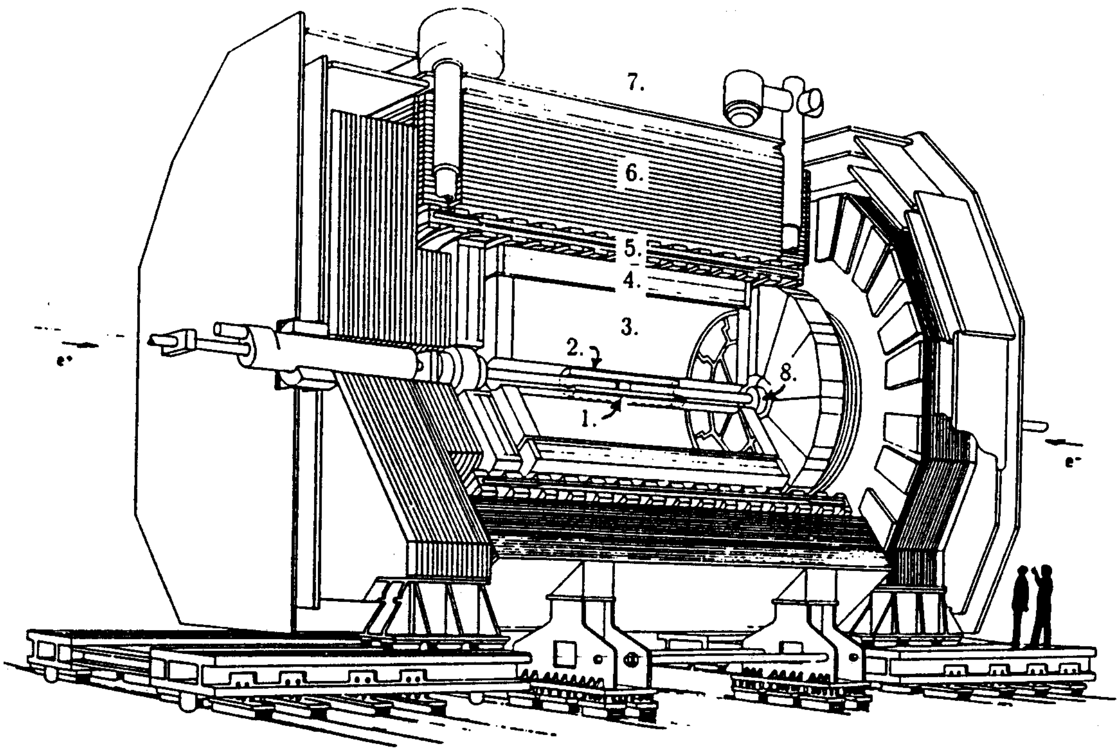

Figure 2.2: Overall view of the ALEPH detector: 1) VDET, 2) ITC, 3) TPC, 4) ECAL, 5) Superconducting coil, 6) HCAL, 7) Muon chamber, 8) Luminosity monitor

From inside to outside, particles emitted from the beam crossing point encounter:

1. Beam Pipe : a hybrid cylindrical pipe made of beryllium ($|z| < 38$cm), connecting material ($38 < |z| < 50cm$), and aluminum part ($50 < |z| < 269.5$cm). The central part made of beryllium has an inner radius of $5.30cm$, an outer radius of 5.41cm, and amounts to 0.00312 X_0 radiation length at 90°.
2. Vertex Detector (VDET) : a silicon wafer detector with 2 concentric layers.
3. Inner Tracking Chamber (ITC) : a cylindrical drift chamber with 8 layers of axial wires.
4. Time Projection Chamber (TPC) : a large cylindrical time projection chamber.

The three tracking devices (VDET, ITC and TPC) will be described in details in Sec. 2.2

5. Electromagnetic Calorimeter (ECAL) : a sampling device consisting of lead sheets and wire chambers.
6. Superconducting Solenoid : aluminum around NbTi/Cu coil cooled by liquid helium. It has a cryostat volume of $R_{inner} = 2.48m$, $R_{outer} = 2.92m$, and 7 m long. The total radiation length is 1.6 X_0. It creates a magnetic field of 1.5 T parallel to the beam axis of the detector with a 5 kA current. Measured field fluctuations, $\Delta B_z/B_z$, are less than 0.2 %. Radial field component and azimuthal component are small: $B_r/B_z < 0.4\%$ and $B_\phi/B_z < 0.04\%$.
7. Hadronic Calorimeter : a iron based hadronic calorimeter. It also serves as yoke for the magnetic flux and as a muon filter.

The two calorimeters (ECAL and HCAL) will be described in details in Sec. 2.3

8. Muon Chambers : a double layer wire counter made of carbon coated plastic tubes. The barrel part has 12 double layers (each layer covers 30°). The middle-angle part has 9 double layers overlapped with each other and 1 layer in the bottom. Two end-caps consist of 4 double layers.

The ALEPH detector has three subdetectors for luminosity measurement: i) Solid-state Luminosity Calorimeter (SICAL) [1] consisting of 12 tungsten sheets and silicon pad

[1] from Sep. 1992

layers ($R_{inner} = 6, R_{outer} = 14.6$cm and $250 < |z| < 262$), ii) Luminosity Calorimeter (LCAL) consisting of lead sheets and wire chambers ($R_{inner} = 10, R_{outer} = 52$cm and $262.5 < |z| < 305$), iii) Very small angle Luminosity Monitor (BCAL) consisting of 10 tungsten sheets and plastic scintillators ($R_{inner} = 6.5, R_{outer} = 8.5$cm and $770 < |z| < 784$).

2.2 Tracking Devices

The lifetime of a particle is deduced from the measurement of its decay length. Since a decay length of a short lived ($\sim 10^{-13} - 10^{-15}$ s) particle like τ lepton, charmed mesons, bottom meson etc. can only be obtained from the (track) reconstruction of its daughter particles, tracking is an essential part of the lifetime measurement. Here we will describe the ALEPH tracking devices from the point of view of 3 dimensional tracking performances.

2.2.1 TPC: Time Projection Chamber

Structure

The TPC is a cylindrical drift chamber of which dimensions are $R_{outer} = 1.8$ m, $R_{inner} = 31$ cm and length = 4.7 m and its axis is parallel to the magnetic and electric fields. The TPC volume is divided into two cages by a graphite coated mylar membrane (thickness = 25μm) which acts as a high voltage electrode (Fig. 2.3). It operates in a gas mixture of 91% Ar and 9% CH_4 at atmospheric pressure.

When a charged particle traverses the TPC volume, it ionizes the gas. Electrons from ionization are accelerated by the electric field of 11 kV/m, parallel to the magnetic field, and drift to the end-plates (maximum drift length = 2.2 m). The end-plate is a wire chamber where the electrons produce avalanches on the sense wires. The location of the avalanche along the wire is measured by the segmentation of the cathode plane into small areas, so-called *pad*. The $r\phi$ coordinate is measured from the pad position and the z coordinate is measured from the drift time with the known drift velocity. Each end-plate

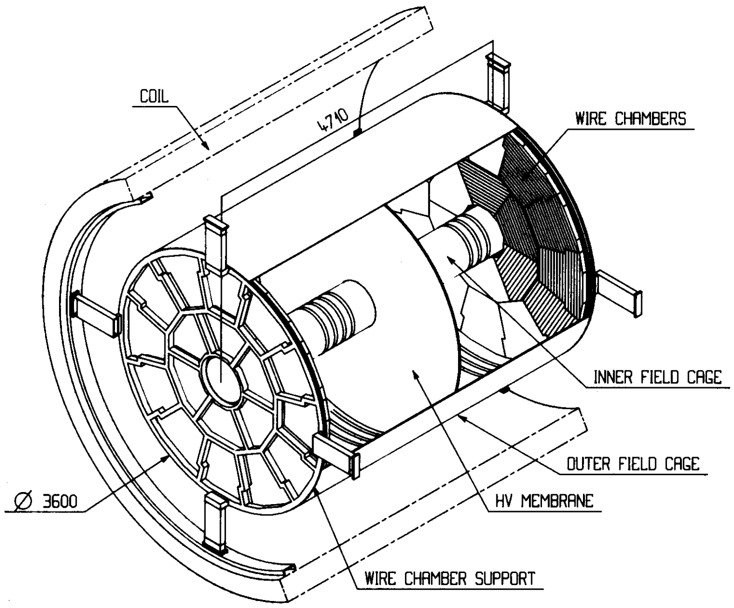

Figure 2.3: TPC overall view

has 6 inner sectors (type K) and 12 outer sectors (type M, W) which have concentric 9 and 12 rows of pads ($3cm \times 6.2mm$), respectively, for 3 dimensional coordinate measurement (Fig. 2.4). Thus TPC allows a maximum of 21 $r\phi$ and z coordinate measurement. There are also 8 (11) rows of trigger pads ($6.8mm \times 15°$) in each inner (outer) sector.

Coordinate resolution

The $r\phi$ coordinate resolution depends on several factors, such as the magnetic field and the angles of the track segment with respect to wires and pads, etc.. When the pad crossing angle is 0°, the typical spatial $r\phi$ resolution is about 180μm. Fig. 2.5 shows the TPC $r\phi$ hit resolution.

The z coordinate resolution has been measured with di-muons and cosmic-rays by studying the drift length assuming that the trajectory is a straight line in $r - z$ plane. Using the pad information 0.8 mm spatial resolution is achieved for tracks with polar angle around 90° (Fig 2.5). This becomes twice as large at polar angle about 20°(160°).

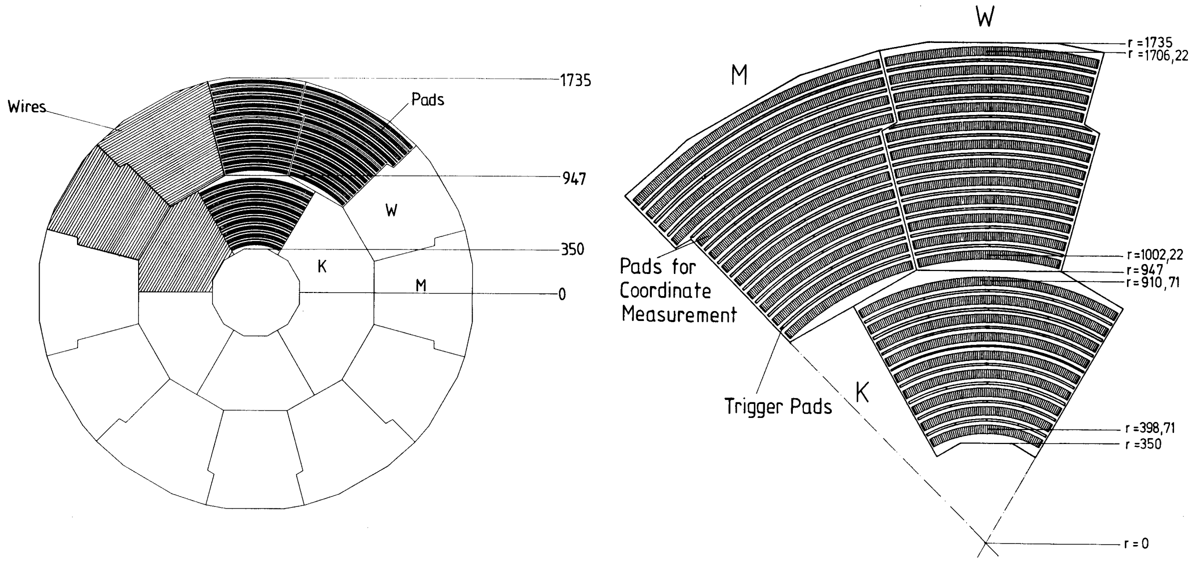

Figure 2.4: Overall view of TPC end-plate and M, W, K sector

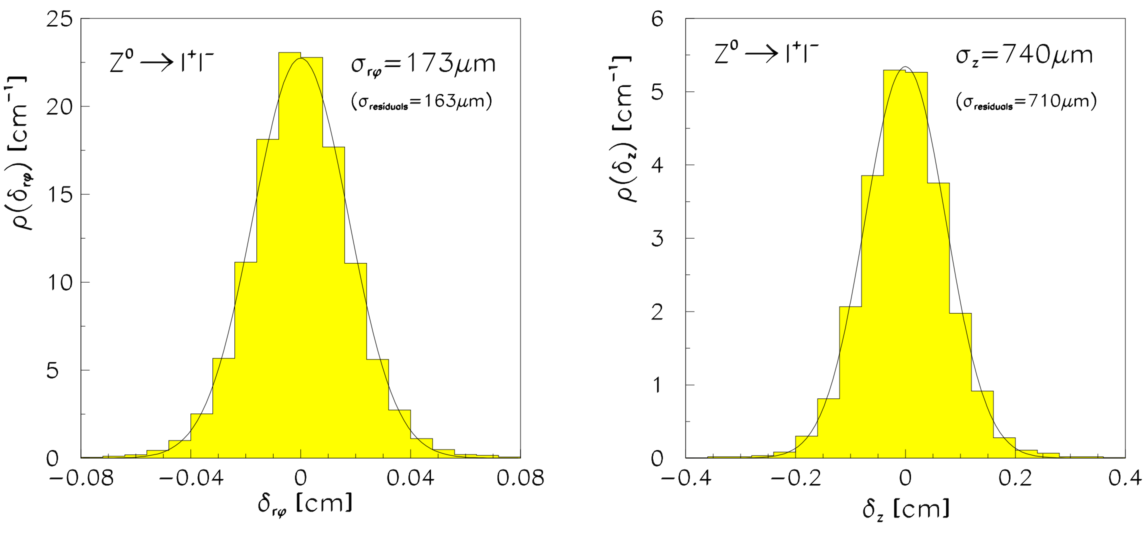

Figure 2.5: TPC $r\phi$ and z coordinate resolutions measured with the tracks from leptonic Z^0 decays

The z coordinate can also be measured with the wires when there is no confusion due to another track intersecting. The space resolution of z from wire measurement is of the order of 1 mm.

Alignment and calibration

The sectors of TPC end-plates are aligned relatively to each other within $\pm 40 \mu$m precision mechanically. The possible misalignment of the 18 sectors (6 inners + 12 outers) for each end-plate can be checked with laser beams, cosmic ray events and two track events like $e^+e^- \rightarrow \mu^+\mu^-$ [30]. Assuming infinitesimal deviation from the perfectly aligned detector, the relative positions between the inner and outer end-caps can be described in a rectangular coordinate system by 6 parameters: 3 offsets along the axes and 3 rotation angles. These parameters are obtained with $Z^0 \rightarrow \mu\mu$ events by fitting the muon tracks using TPC inner sector and outer sector independently.

On the other hand, the TPC has a laser calibration system to provide information on the residual inhomogeneities of the electric and magnetic fields. The laser calibration provides thus a geographical map of drift velocity in order to correct the distortions of tracks in the TPC volume. The drift velocity is determined from the reconstructed polar angles of tracks using the laser beam.

Particle identification : dE/dx

The TPC is not only the main tracking device of ALEPH but also a particle identifier. The measurement of the particle specific energy loss by ionization, dE/dx, allows the identification of particles. The dE/dx is measured from the sense wire pulse. Since the distance between neighboring sense wires is 4 mm, a charged track can have a maximum of 340 sense wire pulses. Fig. 2.6 shows the scatter plot of the reconstructed dE/dx as a function of reconstructed track momentum for all tracks with at least 150 associated wire hits in a sample of about 40,000 tracks from data. dE/dx is an important observable for identification of electrons when it is used together with the ECAL information.

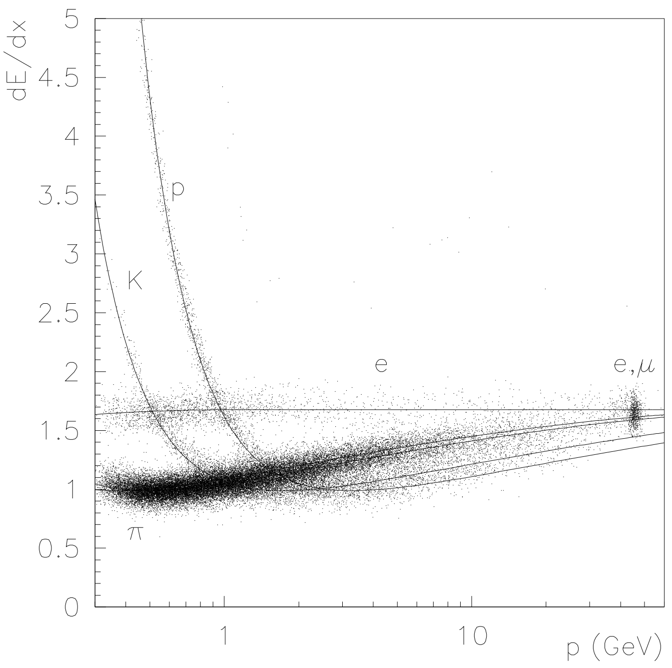

Figure 2.6: dE/dx versus momentum. The values of dE/dx are normalized to 1 at the minimum ionization. The solid curves give the expected mean dE/dx for kaon, proton, electron, muon, and pion.

2.2.2 ITC: Inner Tracking Chamber

Structure

The ITC is a conventional cylindrical drift chamber with eight concentric layers of sense wires parallel to the beam axis (Fig. 2.7). It serves mainly two roles in ALEPH: one

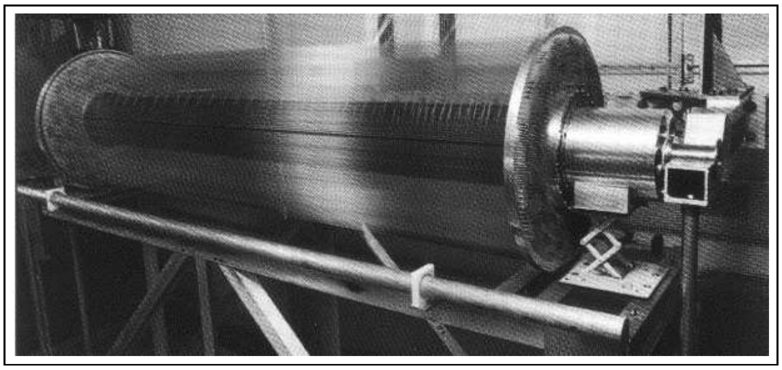

Figure 2.7: Overall view of ITC end-plate

is to provide a maximum of eight accurate $r\phi$ points for tracking and the second is to give the only tracking information for the Level-1 trigger. The dimensions of ITC are $R_{outer} = 28.8$ cm, $R_{inner} = 12.8$ cm and length = 2 m. Tracks with $-0.97 < \cos\theta < 0.97$

traverse all eight layers. The ITC is filled with a mixture of 50% Ar and 50% ethane (C_2H_6) at 1 bar.

Coordinate measurement

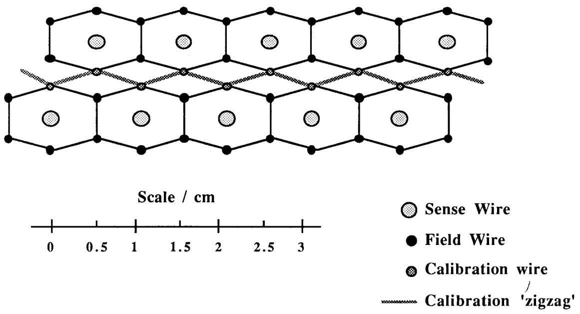

Figure 2.8: ITC cross sectional view of wires

The $r\phi$ coordinate is obtained by measuring the drift time in the cell, giving a precision of about 150 μm. The z coordinate is measured from the time difference of the signals at the two ends of each sense wire, but the resolution of z coordinate ($\sim$ 7 cm) is not sufficient for 3 dimensional tracking.

Alignment

The alignment of the ITC with respect to the TPC has been measured by using the cosmic events with a precision of $\sim 100\mu$m in $r\phi$. The relative offset along the x axis and the y axis are about $450 \pm 100\mu$m and $0 \pm 50\mu$m, respectively, and the rotation angles are very small, $\sim$ 0.1mrad. The values are taken into account in the track reconstruction. The misalignment along the beam axis is not important because the ITC z coordinates are not used in the track reconstruction.

2.2.3 VDET: Micro Vertex Detector

The VDET consists of 2 concentric layers of double side silicon wafers aligned along the beam axis. A silicon strip detector is a specialized application of a p-n diode. The coordinate resolution totally depends on the pitch between the neighboring diodes (normally it is about 20 to 50 μm).

The main difference of the ALEPH VDET installation plan [31] in 1982 compared with those of other experiments (MARK II, DELPHI, OPAL and CDF) was that ALEPH considered to install a silicon strip detector with readouts on *both* sides ($r\phi$ and z) of the *same* wafer essentially from the start aiming for 3 dimensional position information for each particle hit [33] [2]. Fig. 2.9 shows the VDET. The inner layers of VDET are placed

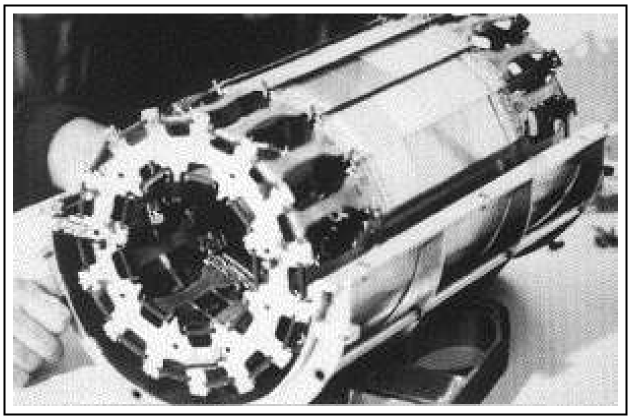

Figure 2.9: Overall view of VDET

at $R = 6.3$ cm and the outer layers are located 11 cm away from the beam axis. The inner (outer) layers consist of 9 (15) modules. Two layers give a thickness of 0.041 X_0 at 90°.

The thickness of a silicon wafer is about 300μm and the size is $5.12 \times 5.12\text{cm}^2$. Each silicon wafer has 1024 readout strips on z side and 512 strips on ϕ side. The effective strip pitch is 100 μm on $r\phi$ side and 50 μm on z side. Fig. 2.10 shows one module of the VDET.

The active detector areas of adjacent wafers overlap by 2mm to ensure full ϕ coverage. The overlapping area is about 4% of the full coverage. Since both layers cover only 20 cm along the beam pipe, the tracks with $\theta < 50°$ or $\theta > 130°$ are beyond the VDET acceptance.

[2] In 1989 a few prototype modules were installed, in 1990 a complete inner layer and about 50% of outer layer were installed and finally in 1991 the installation of a complete inner and outer layers was finished.

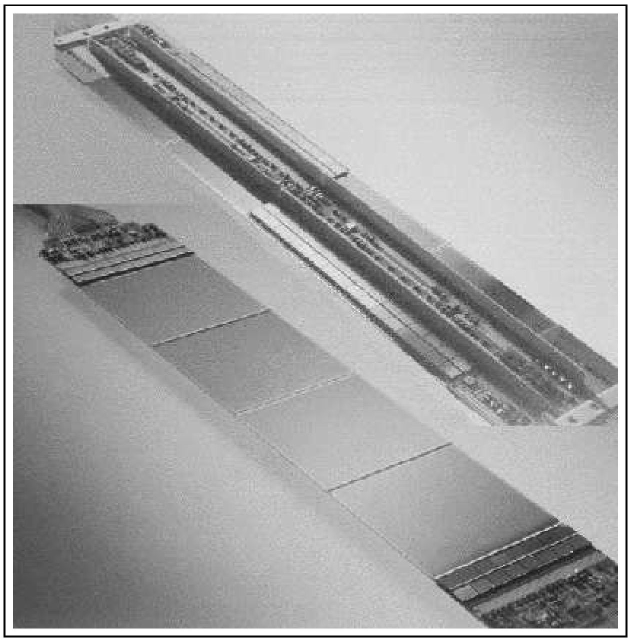

Figure 2.10: A VDET module containing 4 double-sided silicon wafers

Coordinate measurement

The reconstructed track by the TPC and the ITC is refitted using a maximum of 2 accurate 3-dimensional VDET hits. The coordinate resolutions are about 12 μ both in $r\phi$ and in z. Fig 2.11 shows the single VDET hit resolutions of $r\phi$ and z readouts using dimuon events (dividing by $\sqrt{2}$ gives a single hit uncertainty).

Alignment

The alignment of the Si strips can be measured optically with a precision better than 2μm and the alignment of the plates each carrying 4 Si wafers is known to $\pm 20\mu$m. Also the relative alignment of each wafer is obtained by looking at the separation of hits in the overlapped area using the dimuon events.

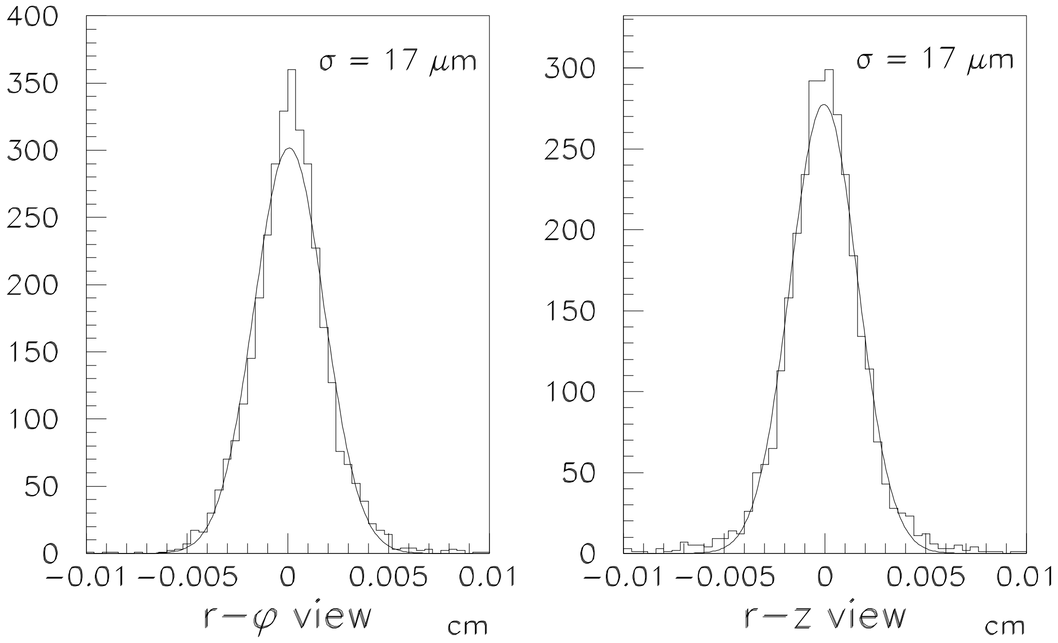

Figure 2.11: Single VDET hit resolutions of $r\phi$ and z components.

Pattern recognition problem

The ALEPH VDET is not a tracking device by itself, but it plays a very important role in the lifetime measurement because it adds 2 high precision 3-D coordinates to the reconstructed track from TPC/ITC and finally allows a precision of the order of 20μm in both $r\phi$ and z components of the impact parameter.

Not all tracks with VDET have such a good spatial resolution. Since the positional uncertainty of the extrapolation to the VDET layer is so big ($\sim 100\mu$m in $r\phi$ and $\sim 800\mu$m in z) with respect to the VDET coordinate resolutions, it is possible that VDET hits are incorrectly associated to non-related tracks when the tracks are close compared with their resolution. The overall mismatched tracks amount to 3% of the total associated tracks [34] in the hadronic Z^0 decay events. About 2% of mis-associations happen when tracks have 2 VDET hits. This value becomes much larger, $\sim 10\%$, when tracks are associated with only one VDET hit. The pattern recognition problems also happen frequently in the 3-prong tau decays where the 3 tracks are very close to each other due to the large boost.

2.2.4 Tracking performance

Charged track reconstruction uses VDET, ITC and TPC hits (a maximum of 31 three dimensional points for each charged track, 21 points from TPC, 8 from ITC, 2 from VDET). Track reconstruction means finding 5 helix parameters: curvature (R), polar angle (θ or $\tan\lambda$), azimuthal angle (ϕ_0), and impact parameters (d_0 and z_0) (App. A).

Momentum resolution

The errors on the polar angle and the azimuthal angle measurement using the 21 TPC points are

$$\Delta \tan\theta \approx 6 \times 10^{-4}$$

$$\Delta\phi \approx 4 \times 10^{-4} \oplus \frac{0.0028}{p(\mathrm{GeV/c})}$$

Since the error on the polar angle is small, the relative error on the momentum coincides with the relative error on the transverse momentum. For a track with 21 TPC coordinates, a circle fit in the $r\phi$ plane yields:

$$\frac{\Delta p_T}{p_T} \approx 10^{-3} p_T(\mathrm{GeV/c})(\frac{\bar{\sigma}}{150\mu\mathrm{m}})(\frac{1.5T}{B}) \oplus 0.003$$

where $\bar{\sigma}$ is the average TPC coordinate error and the last term, 0.003, is the contribution of the multiple scattering in the gas of the TPC. However the transverse momentum measurement error depends indirectly on the polar angle, because a track with large $|\cos\theta|$ has normally less TPC hits and smaller arc length in the $r\phi$ plane.

With ITC and TPC a particle momentum can be measured with $\Delta p/p^2 \sim 0.8 \times 10^{-3}(GeV/c)^{-1}$ in case of 45 GeV particles. With the help of VDET, the addition of two very high precision points on the helix of a given charged track improves the particle's momentum by a factor of about 25 %.

Fig. 2.12 shows the final momentum resolution using the track reconstructed by full (TPC, ITC, and VDET) tracking devices.

Tab. 2.1 summarizes the momentum resolutions with different sets of detectors.

Figure 2.12: Beam energy over track momentum of the muon tracks reconstructed with full tracking devices in $Z^0 \rightarrow \mu\mu$ events

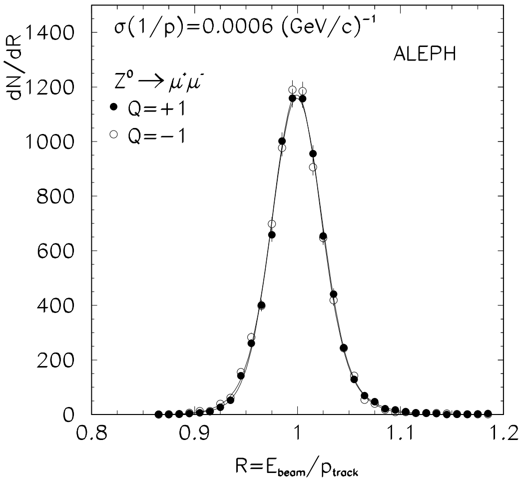

Detector	Momentum resolution $\Delta p/p^2(\mathrm{GeV/c})^{-1}$
TPC only	1.2×10^{-3}
TPC+ITC	0.8×10^{-3}
TPC+ITC+VDET	0.6×10^{-3}

Table 2.1: Momentum resolutions of ALEPH tracking devices

Impact parameter resolution

What is important in the lifetime measurement is not the resolution of coordinates itself but the impact parameter (d_0, z_0) resolution. For tracks with TPC hits only, the resolutions of the impact parameters, d_0 and z_0, when the track has 21 TPC points are

$$\sigma_{d_0} \approx 100 \oplus \frac{840}{p(\mathrm{GeV/c})}\mu\mathrm{m}$$

$$\sigma_{z_0} \approx 500 \oplus \frac{840}{p(\mathrm{GeV/c})}\mu\mathrm{m}$$

Typically they are $\sim 300\mu$m and $\sim 800\mu$m respectively.

The impact parameter resolution of tracks with VDET hits is much more precise than that of tracks with ITC and TPC hits only (Tab. 2.2).

Detector	Impact parameter resolution	
	$r\phi(\mu\mathrm{m})$	$rz(\mu\mathrm{m})$
TPC only	300	800
TPC+ITC	100	800
TPC+ITC+VDET	23	28

Table 2.2: Impact parameter resolution of ALEPH tracking devices

For high momentum tracks, the resolutions of d_0 and z_0 are about 23 μm and 28 μm, respectively. Fig 2.13 shows the $\sum d_0$ and $\Delta z_0 \cos\lambda$ distributions for $Z^0 \to \mu\mu$ events (dividing by $\sqrt{2}$ gives single track resolutions). In these events where the two muons are produced at the same position and are emitted back-to-back, $\sum d_0$ width measures directly the tracking resolution.

The impact parameter resolution for low momentum tracks can be measured by the hadronic Z^0 decay events after subtracting the smearing from mis-measured impact parameters due to secondary vertices. Fig. 2.14 shows the d_0 and z_0 resolutions for track with VDET hits in both layers as a function of momentum. Both d_0 and z_0 resolutions can be parameterized as

$$\sigma_{d_0} = \sigma_{z_0} = 25 + \frac{95}{p(\mathrm{GeV})}(\mu\mathrm{m})$$

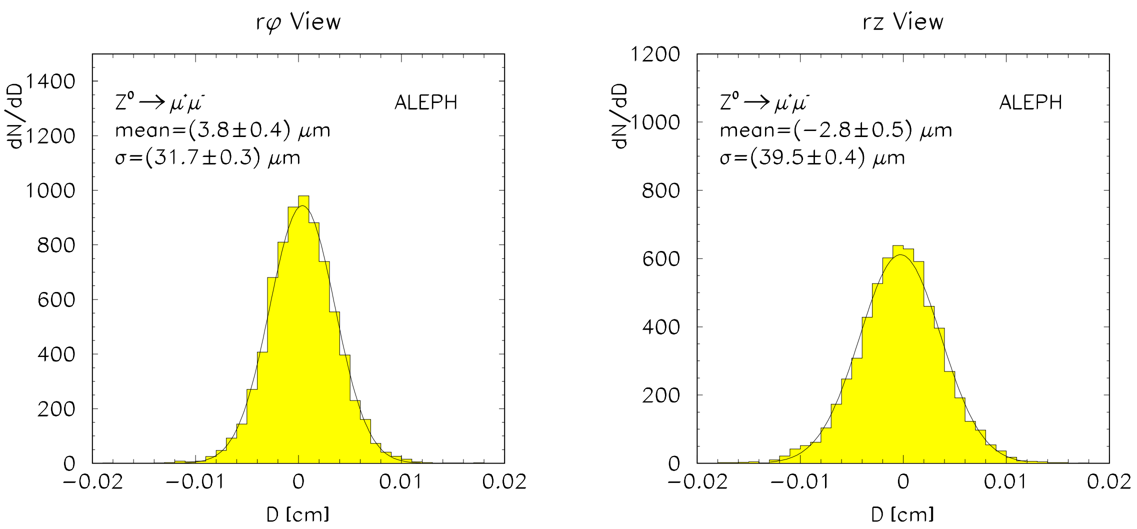

Figure 2.13: Resolutions of $\sum d_0$ and $\Delta z_0 \cos\lambda$ in $Z^0 \to \mu\mu$ events

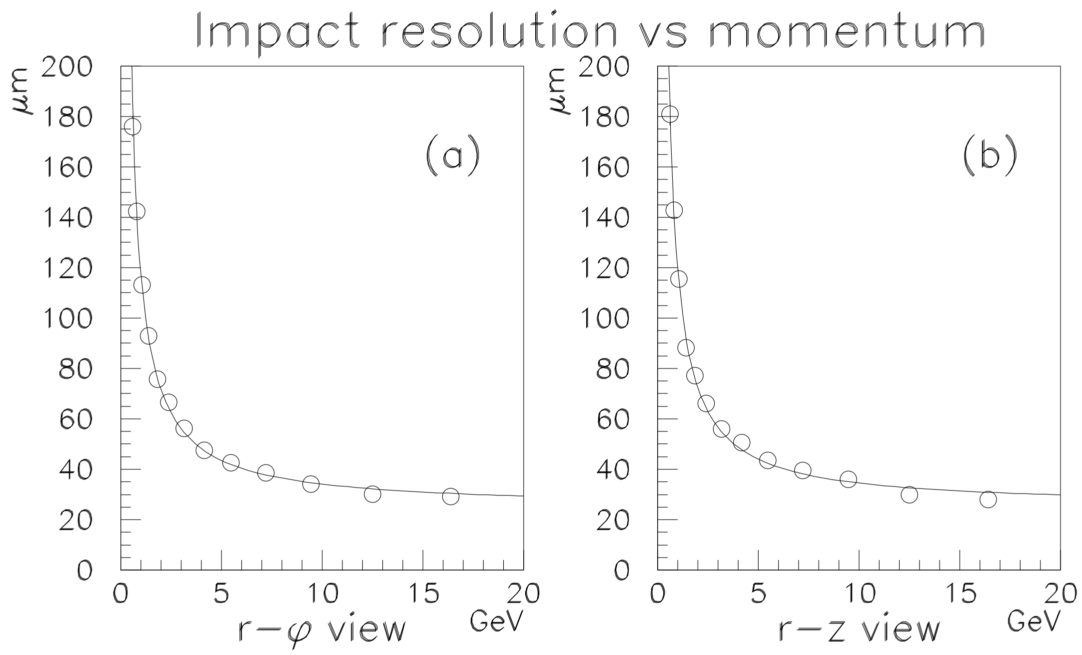

Figure 2.14: Impact parameters, d_0 and z_0 resolutions for the low momentum region

2.3 Calorimeters

Full reconstruction of tau decay products, charged tracks and neutrals, is an important factor in the new method developed in this thesis for the lifetime measurement. Charged tracks are precisely reconstructed, as seen in the previous section. Considering that more than 40% of tau decays have at least one π^0's, the precise reconstruction of full decay products of tau events depends on the performance of the calorimeters.

2.3.1 ECAL: Electromagnetic Calorimeter

The Electromagnetic Calorimeter (ECAL) is a lead/wire-chamber sampling device installed inside the solenoid. Fig. 2.15 shows the overall view of the ECAL. The overall

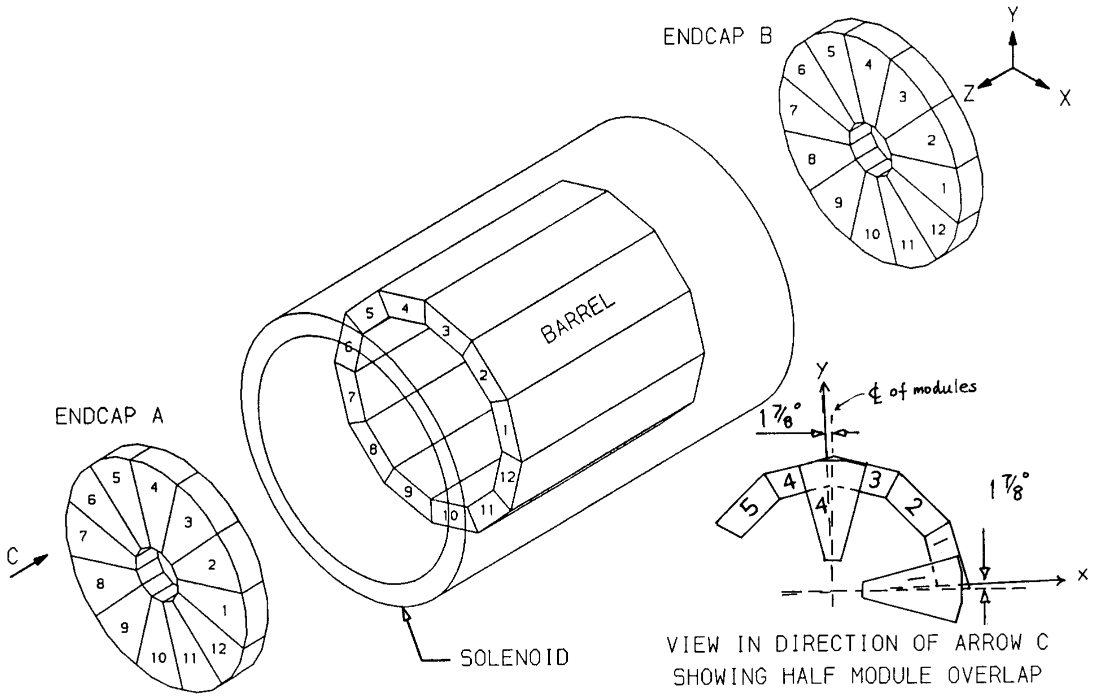

Figure 2.15: Overall view of ECAL

sizes are $R_{inner} = 1.85m$ and $R_{outer} = 2.25m$ for the barrel and $R_{inner} = 54$cm and $R_{outer} = 2.35m$ for the end-cap. The barrel and each end-cap consist of 12 modules. ECAL covers a very large solid angle ($0 < \phi < 2\pi$ and $|\cos\theta| < 0.98$) and has only 2%

cracks in the barrel and 6% in the end-cap. The range $0.71 < |\cos\theta| < 0.79$ is an overlap region between barrel and end-cap modules.

Fig. 2.16 shows the lead/wire-chamber of ECAL. Showers developed in the lead sheets are measured in the proportional wire chambers. The total energy and the position of the showers are measured using very finely segmented ($\sim 3 \times 3\text{cm}^2$) cathode pads.

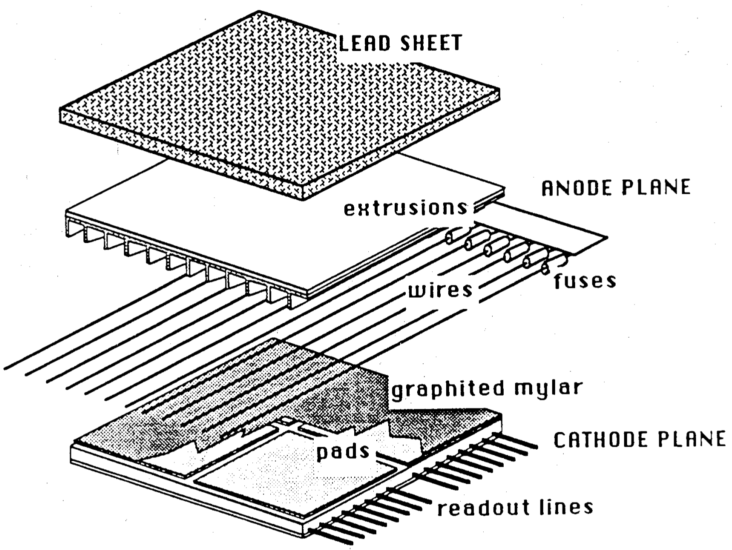

Figure 2.16: Typical ECAL layer of lead/wire-chamber

The longitudinal shower development is measured by 45 layers grouped into 3 storeys containing 10 (2 mm), 23 (2 mm), and 12 (4 mm) lead/wire chambers, corresponding to 4, 9, and 9 radiation lengths for a total of 22 X_0. The cathode pads are connected internally to form *towers* pointing to the detector origin. The granularity varies from $17 \times 17\text{mrad}^2$ at $\theta = 90°$ in the barrel to $9 \times 10\text{mrad}^2$ at $\theta = 40°$ in the end-cap.

The direction (θ, ϕ) measurement is done by the calculation of the shower center of gravity, from the four leading towers:

$$\theta = \frac{\sum_{i=1}^{4} E_i \theta_i}{\sum_{i=1}^{4} E_i}, \phi = \frac{\sum_{i=1}^{4} E_i \phi_i}{\sum_{i=1}^{4} E_i}$$

where E_i is the energy deposit in the tower number i with coordinates θ_i and ϕ_i. The measured resolutions of θ and ϕ are:

$$\Delta\theta/\sin\theta = \Delta\phi = 0.32 + \frac{2.7}{\sqrt{E}(\mathrm{GeV})}\mathrm{mrad}$$

The energy measurement resolution is

$$\frac{\Delta E}{E} = 2\% + \frac{0.18}{\sqrt{E}}$$

Particle identification

Different particle types give different responses in ECAL. This makes it possible to separate one particle from the other. For example, electrons and photons deposit 99% of their energy in the ECAL volume by making electromagnetic showers starting in the first storey. On the other hand, normally muons go through without interaction in the ECAL volume and hadrons make showers starting in the second or third storeys. Thus, variables describing the longitudinal and transverse shower sizes, R_L and R_T, are used as identifiers.

2.3.2 HCAL: Hadronic Calorimeter

The large iron structure supporting the ALEPH detector plays two different roles; it serves as yoke for the magnetic flux return and as absorber for all hadrons produced from the e^+e^- collision. The main structure is subdivided into a central barrel and two end-caps (Fig. 2.17).

The barrel ($R_{inner} \sim 3$m, $R_{outer} \sim 4.68$m and $L \sim 7.24$m) consists of 12 modules, each one has 22 slabs 5 cm thick except the last slab (10 cm). The intervals (2.2 cm) between two slabs are filled with streamer tube detectors that consist of finely segmented plastic comb profiles ($0.9 \times 0.9\mathrm{cm}^2$). The total thickness of the calorimeter is 120 cm at 90°, corresponding to 7.16 interaction lengths.

Each end-cap consists of 6 petals which cover 60° each. End-caps and barrel cover 93 % of total solid angle.

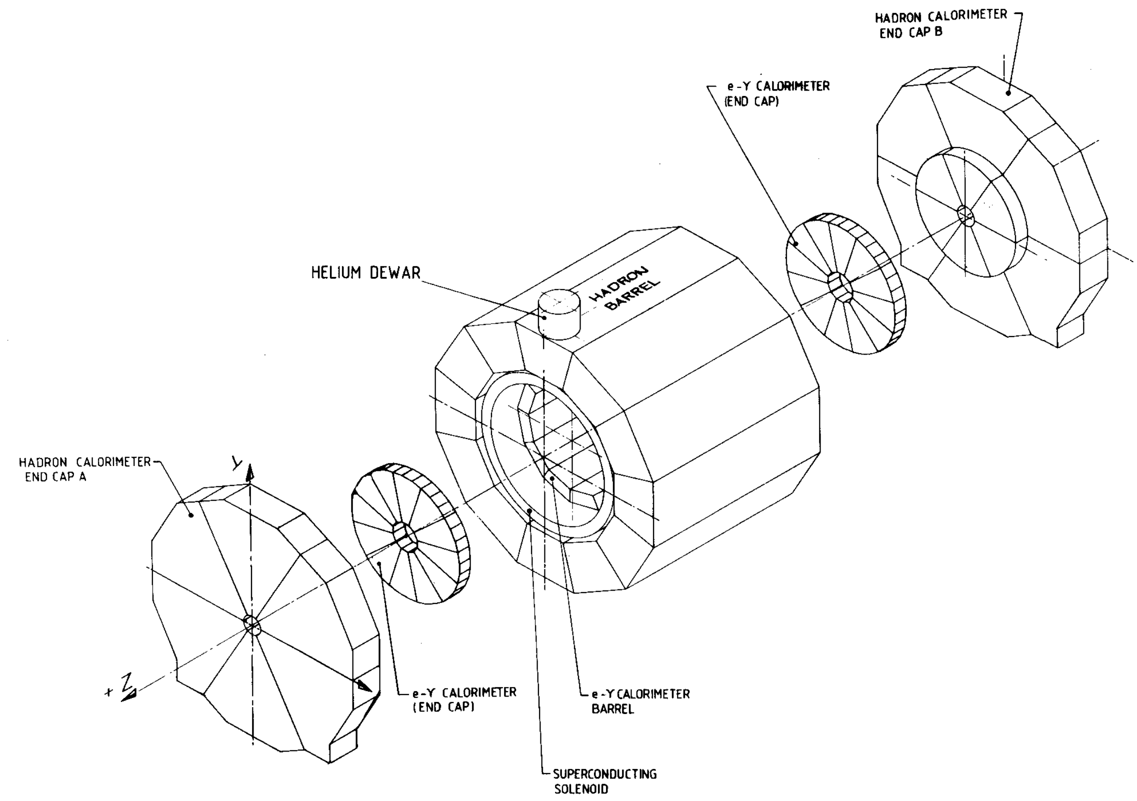

Figure 2.17: Overall view of HCAL

The pads of each layer are connected together in order to form towers pointing to the detector origin like ECAL. About 12 ECAL towers($\sim 0.97^\circ \times 0.97^\circ$) are covered by 1 HCAL tower($\sim 3.7^\circ \times 3.0^\circ$) at 90°.

The resolution of energy measurement is poor ($\sigma_E/E \sim 0.84/\sqrt{E}$) but the digital pattern of HCAL fired tubes from a particle is essential for muon/hadron separation: muons have a line shape but pions have a fireworks shape (Fig. 2.18).

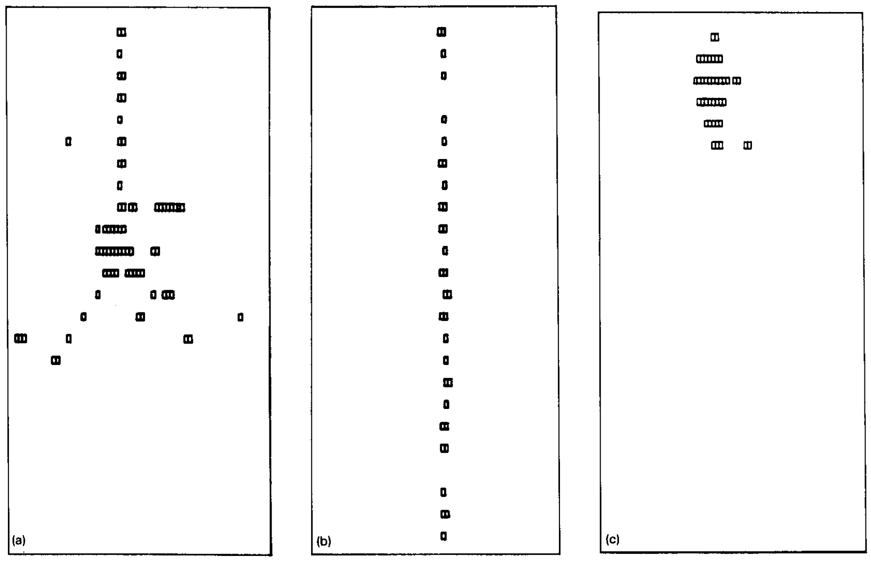

Figure 2.18: Typical HCAL digital patterns of 10 GeV (a) pion, (b) muon, and (c) electron test beams

2.4 Beam position measurement : GET_BP

The beamspot position and beam envelope size are used in many analyses, especially in the lifetime measurements, to define an approximate event origin in the x-y plane and to know the uncertainty of the interaction position. The measurements of the beamspot position and the beam envelope size are done by the GET_BP algorithm in the ALEPH.

Since the tracking resolution with VDET is about 25 μ, at least the same level of accuracy is needed on beam position. To get the resolution of the beamspot position with the precision of 10 μm, about 400 qualified tracks are needed considering the resolution of the tracking. Since a Z^0 hadronic decay event has about 4-5 well qualified tracks (with some restrictions on the numbers of VDET, ITC, TPC hits), events are grouped in "chunks" of about 100 events.

The beam position is obtained by plotting the distances of closest approach to the nominal beam position of tracks in the $r\phi$ plane versus their ϕ angles at that points, and fitting the resulting curve to a sinusoid. The sinusoid can be parameterized in terms of the average beam position as:

$$< d_0 >= \sin\phi < x_{BP} > - \cos\phi < y_{BP} > + d_{off}$$

The beam size measurement is done by using the $Z^0 \to \mu^+\mu^-$ events. By plotting the impact parameters versus the ϕ angles with many events, one can reconstruct the beam envelope.

As the results, ALEPH has good enough information of the beam position and size: $\sigma_x^{BP} \sim 30\mu$m, $\sigma_y^{BP} \sim 10\mu$m, and the x size of the beam is about 145μm and the y size is about 5μm [69]. The size of the beam envelope along the z-axis is very large ($\sim$ 1cm).

Chapter 3

Algorithms for τ Physics

The procedures for the τ lifetime measurement can be divided into three steps: 1) selection of τ decay events to be free from backgrounds 2) selection within the tau data sample to reject badly reconstructed tracks and/or badly reconstructed tau direction, etc. 3) extraction of τ lifetime from the tau sample by using a likelihood method, or a least square fit, or a trimmed mean, etc..

Usually, above 3 steps contain time dependent factors because the experimental environment changes each year, for example, VDET installation, TPC short-circuit problems, changes of the reconstruction algorithms, etc.. Since the τ lifetime measurement in this thesis is based on the ALEPH tau events collected in 1992 runs, we will describe the selection of tau events (TSLT) and some identification/reconstruction algorithms (TAUPID, PEGASUS, TOPCLAS) according to their 1992 setting.

3.1 Tau event selection : TSLT

A typical $\tau\tau$ event is characterized by $i)$ event shape : two back-to-back collimated jets with low charged track multiplicity and $ii)$ kinematics : large missing energy taken away by neutrinos. These characteristics are roughly enough to cut away the non-τ backgrounds like $\gamma\gamma \to f\bar{f}$, $e^+e^- \to e^+e^-$ $Z^0 \to q\bar{q}$, and $Z^0 \to \mu^+\mu^-$ (Fig. 3.1). Events not related to the e^+e^- collisions, like cosmic ray events, are distinguishable by localizing the position of charged tracks in the small region around the e^+e^- interaction point.

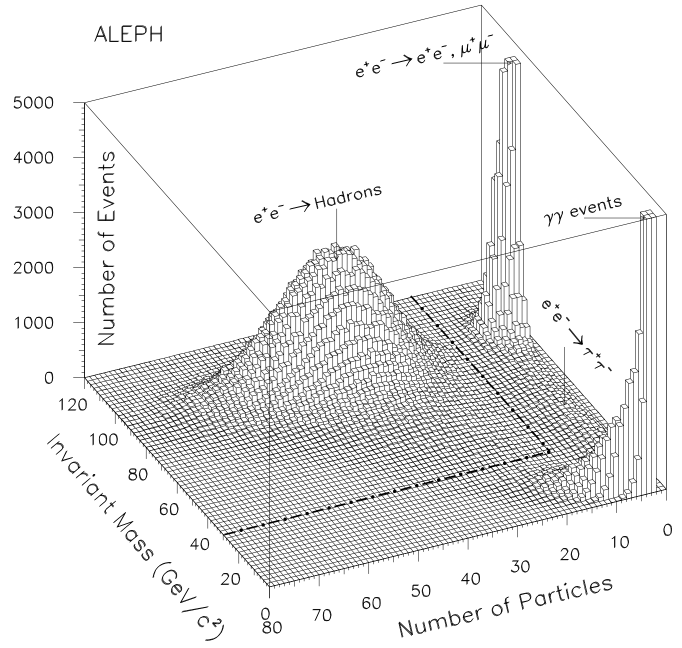

Figure 3.1: Invariant mass versus number of particles for all events with at least two charged tracks in 1992 data

The $Z^0 \to \tau\tau$ events are selected by using TSLT algorithm in ALEPH which is based on the above tau event characteristics and some more criteria [37]. In a given event, TSLT proceeds in the 3 following steps and checks the various criteria to be a tau event (Subsec. 3.1.1):

1 A tau event is divided into 2 hemispheres by the plane perpendicular to the event thrust axis.

2 The 4 momenta of the two jets, charged tracks and neutrals of a hemisphere, are summed up to compute the total energy, acollinearity, etc..

3 Electron or muon tracks are identified by the QEIDO and QMUIDO algorithms, developed in ALEPH for general purpose.

3.1.1 Selection criteria: Rejection of non-$\tau\tau$ events

Rejection of $Z^0 \to q\bar{q}$ events

All leptonic decay events $Z^0 \to l^+l^-$ are characterized by the low multiplicity of charged tracks compared with hadronic decays $Z^0 \to q\bar{q}$ that yield about 20 to 60 charged tracks.

Since $Z^0 \to \tau\tau$ events usually have 2 or 4 tracks in the final state via 1-prong and/or 3-prong τ decays, the number of *good* charged tracks of an event, N_{chg}^{event}, is requested to satisfy: $2 \leq N_{chg}^{event} \leq 8$. Only *good* charged tracks are counted to avoid fake tracks from beam-gas interactions or interactions with detector material, cosmic rays, secondary decay products, etc.. They are defined as tracks having $|d_0| \leq 2$cm, $|z_0| \leq 10$cm, and $|\cos\theta| \leq 0.95$ and reconstructed with at least 4 TPC hits.

$Z^0 \to q\bar{q}$ events have large jet masses compared to τ mass and have large opening angles, where the opening angle is defined as the maximum angle between combination of 2 *good* tracks in the jet. These characteristics are used to reject the $q\bar{q}$ backgrounds. In addition, since the number of total reconstructed charged tracks and neutrals in a tau event is limited even in multiple π decays, the total number of objects becomes another criterion to separate hadronic events.

Rejection of $\gamma\gamma$ events

Events from $\gamma\gamma$ processes, $\gamma\gamma \to l^+l^-, q\bar{q}$, are characterized by a small visible energy and a large acollinearity. Thus to be selected as a tau event, the total reconstructed energy of a given event must not be too small, the acollinearity must be small, and the transverse momenta of the two jets must be balanced.

Rejection of $Z^0 \to e^+e^-$ and $Z^0 \to \mu^+\mu^-$ events

There are at least two tau neutrinos in the final states of $Z^0 \to \tau^+\tau^-$ events because the tau is a short lived particle decaying to $l\bar{\nu}_l\nu_\tau$ or $h\nu_\tau$ in the detector volume. In $Z^0 \to e^+e^-$ or $Z^0 \to \mu^+\mu^-$ events, all the beam energy is carried out by the two leptons with equal momenta if there is no radiation. Therefore, the energy carried by the two charged tracks are used as a criterion to reject the $Z^0 \to e^+e^-$ or $Z^0 \to \mu^+\mu^-$ events. Alternatively, this rejection can be done on the basis of the missing mass of the event.

Rejection of cosmic ray events

Cosmic ray events can be rejected simply by the *good* track definition that demands at least 1 *good* track originating from the beam-beam interaction region, for instance, ($|d_0| \leq 1$cm and $|z_0| \leq 5$cm).

3.1.2 Selection efficiency

The total efficiency can be defined as follows.

$$\varepsilon_{\tau\tau} = \varepsilon_{acc} \cdot \varepsilon_{trig} \cdot \varepsilon_{sel}$$

where ε_{acc} is the geometrical acceptance, ε_{trig} is the trigger efficiency, and ε_{sel} is the selection efficiency.

The geometrical acceptance is found to be $\varepsilon_{acc} = 0.8254 \pm 0.0013$ using both data and Monte Carlo. No trigger inefficiency is found in the $e^+e^- \to \tau^+\tau^-$ events at the level of 10^{-4}. The selection efficiency, $\varepsilon_{sel} = 0.9468 \pm 0.0019$, is found after the study of each selection criterion efficiency [39] [40]. The total tau event selection efficiency, $\varepsilon_{\tau\tau}$, is therefore,

$$\varepsilon_{\tau\tau} = 78.15 \pm 0.23(\%)$$

Background sources	(%)	
$q\bar{q}$	0.29	± 0.03
$\gamma\gamma$	0.27	± 0.02
e^+e^-	0.62	± 0.07
$\mu^+\mu^-$	0.05	± 0.03
l^+l^-V	0.07	± 0.02
cosmic ray	0.02	± 0.01
total	1.32	± 0.09

Table 3.1: Estimation of remaining backgrounds in the tau sample in 1992 data

Estimated backgrounds in the 1992 data are summarized in Tab. 3.1 [41].

3.2 Tau decay particle identification : TAUPID

In order to identify particles from τ decays with large efficiency, a likelihood method was introduced by M. Davier and Z. Zhang in ALEPH [42]. Five characteristic variables are used in the ALEPH experiment in order to identify a particle:

- TPC information : dE/dx
- ECAL information : R_T and R_L, transverse and longitudinal shower sizes
- HCAL information : $\bar{W}$ and N_{10}, the average shower width over the fired planes and the number of fired planes in the last ten planes respectively.

The usual way of particle identification is to cut away the particles off the criteria (i.e. to assign an identification flag to a particle when the characteristic variables are all inside the criteria).

The basic procedure of the likelihood method is as follow:

- make a reference distribution, $f_i^j(x)$, for a characteristic variable i and a particle j.
- for the particle to be identified, calculate the probabilities P^j to be a type j:

  $$P^j = \frac{\varepsilon^j}{\sum_j \varepsilon^j}$$

  where ε^j is an estimator defined as

  $$\prod_i \frac{f_i^j(x)}{\sum_j f_i^j(x)}$$

- assign an identification flag to the particle corresponding to the largest probability

Since the characteristic variables are found to be uncorrelated with each other and this method does not loose statistics by the cuts on each variable, the method gets higher efficiency than the usual cut methods.

Tab. 3.2 shows the identification efficiencies from the likelihood identification algorithm TAUPID for particles with $p > 2\text{GeV}$. The main backgrounds of identified electrons and

true ($\rightarrow$) identified ($\downarrow$)	e	μ	π
e	99.60 ± 0.03	< 0.01	0.61 ± 0.03
μ	< 0.01	99.46 ± 0.03	0.87 ± 0.03
π	0.40 ± 0.03	0.54 ± 0.03	98.52 ± 0.04

Table 3.2: Identification matrix on $\tau\tau$ Monte Carlo for $p > 2$GeV/c (in %)

muons are the misidentified pions at 0.5 % level. Conversely, misidentified electrons and muons contribute to the pion background at the level of 0.5% each.

Low momentum muons (less than 2GeV/c) are not distinguished from pions since they can not reach the muon detector and both have nearly the same value of dE/dx. Therefore, a cut at 2GeV/c is applied and this cut leads to 5% inefficiency.

3.3 π^0 reconstruction : PEGASUS

About 40 % of τ decays have at least one π^0 in the final state. Since the lifetime measurement using kinematics not only needs the 4 momenta of charged tracks but also those of neutrals, the momentum of π^0's is an important factor in the analysis.

π^0 decay final states can be two photons ($\pi^0 \rightarrow \gamma\gamma$), one photon and two electrons from conversion ($\pi^0 \rightarrow \gamma\gamma \rightarrow \gamma e^+e^-$) or four electrons from conversions ($\pi^0 \rightarrow \gamma\gamma \rightarrow e^+e^-e^+e^-$) in the detector volume. Thus, π^0 reconstruction is started with reconstructing pair conversions and finding photons in ECAL.

In the clusters made by the energy deposits in the ECAL storeys, a sub-cluster is regarded as a photon when this photon candidate has more than 0.25 GeV energy and if there is no associated track at a distance of less than 2 cm away from the barycenter of the cluster. The energy is measured by the energy deposit in the central 4 towers corrected from the expected energy deposit fraction in the 4 towers. The position of the photon impact on the surface of ECAL is calculated from the energy barycenter of the 4 towers and corrected.

π^0's are reconstructed by pairing two photons. The π^0 tagging efficiency depends on the energy of π^0. For low energy π^0, the efficiency is limited due to missing photons, and for high energy π^0, it is limited due to non resolved two photon clusters.

The resolution of π^0 energy measurement, limited by the photon energy resolution, can be improved by the π^0 mass constraint. For low energy π^0's, this π^0 mass constraint plays an important role since the two photons are normally well separated: their opening angle is well measured, so it compensates for the relatively large errors on the energy measurements. For high energy π^0's, both opening angle and energies are fitted to have a mass compatible with π^0. Fig. 3.2 shows the improvement of the resolution of π^0 energy measurement by the mass constraint. The resulting resolution, $\sigma(E)/E$, is about 6.5%,

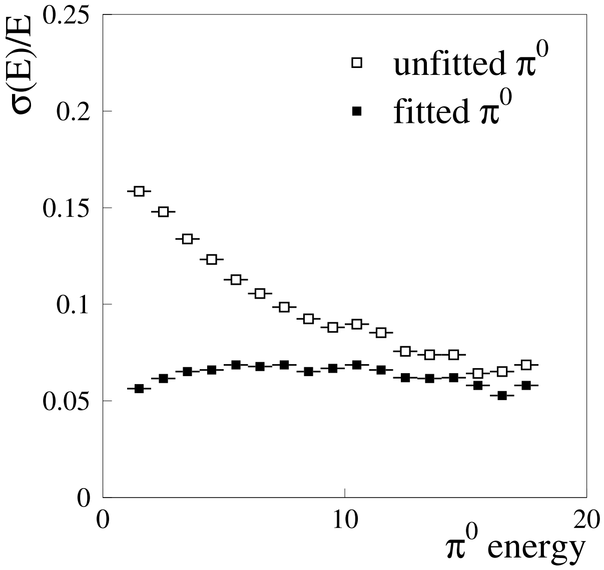

Figure 3.2: Resolution of the π^0 energy before and after fit

is nearly independent of energy.

3.4 Classification of tau decay : TOPCLAS

TOPCLAS, designed for the study of τ branching ratio measurement, classifies the decays into 12 classes according to the particle identification and the number of π^0's [44]. The identification of hadronic decay channels is especially interesting in the 3DIP analysis, since 3DIP method uses the hadronic-hadronic $\tau^+\tau^-$ decay events. Tab. 3.3 shows the hadronic channel identification efficiency and the leptonic channel backgrounds (e and μ). For the hadronic-hadronic $\tau^+\tau^-$ decay events, we estimate about 1% non hadronic-

true ($\rightarrow$) identified ($\downarrow$)	*leptonic*	*hadronic*
leptonic	99.2	0.8
hadronic	0.5	99.5

Table 3.3: Hadronic channel identification matrix on τ Monte Carlo (in %)

hadronic decay backgrounds.

In 3DIP analysis, we use the package to select the hadronic-hadronic $\tau\tau$ decay events and we cut again the leptonic decay contribution using kinematic properties of tau hadronic decay event (Chap. 7). Final leptonic backgrounds are less than 0.3 % of the hadronic-hadronic $\tau\tau$ sample used in lifetime analysis.

3.5 Monte Carlo and detector simulation

3.5.1 τ Monte Carlo simulation : KORALZ

The analysis in this thesis was done with help of the Monte Carlo τ events generated by KORALZ [45]. The production $e^+e^- \rightarrow \tau^+\tau^-$ at the Z^0 pole includes γ and Z^0 contributions with full electroweak radiative corrections.

τ decays are simulated by the library TAUOLA. All known decay modes are simulated and longitudinal polarization effects are taken into account. The input tau mass is 1.777GeV/c^2 and the lifetime is 296fs.

3.5.2 Detector simulation : GALEPH

The generated MC events are processed by the detector simulation program GALEPH (GEANT+ALEPH). After the simulation is tuned to selected real data samples, MC events show excellent agreement with real data.

Part II

TAU LIFETIME AND KINEMATICS IN HADRONIC TAU DECAY

Chapter 4

Review of the Methods for the Tau Lifetime measurement

Tau lifetime measurements have been done using various methods: 1) Decay Length Method, 2) Classical Impact Parameter Method, and first developped in ALEPH, 3) Impact Parameter Difference Method (IPD), 4) Impact Parameter Sum Method (IPS, MIPS). In this chapter we will summarize them briefly and give the motivation why we developed a new method to measure the tau lifetime.

4.1 Introduction : statistics and precision

The tau lifetime is determined by the measurement of the mean decay length of tau. The proper decay length, $c\tau$, of a tau is related to the decay length in the laboratory system, l, as

$$c\tau = \frac{1}{\gamma\beta} l = \frac{m_\tau}{p_\tau} l$$

where p_τ is the tau momentum. Then for mono-energetic τ's, the lifetime is determined by

$$\tau_\tau = \frac{m_\tau}{p_\tau} \frac{l_0}{c}$$

where l_0 is the mean decay length, while the measured decay lengths l ideally show an exponential distribution, $\exp(-l/l_0)$.

The error on the decay length measurement, δl, is characteristic of the tracking devices, and does not depend on the decay length itself but depends on the momentum, the number of VDET hits, and the tau direction measurement, etc.. Fig. 4.1 shows the expected decay length distribution of tau events smeared by the tracking resolutions $\sigma = l_0$, $0.75 l_0$, $0.5 l_0$, $0.25 l_0$. In the case of ALEPH tracking system, the tracking error corresponds to $\sim 0.33 l_0$.

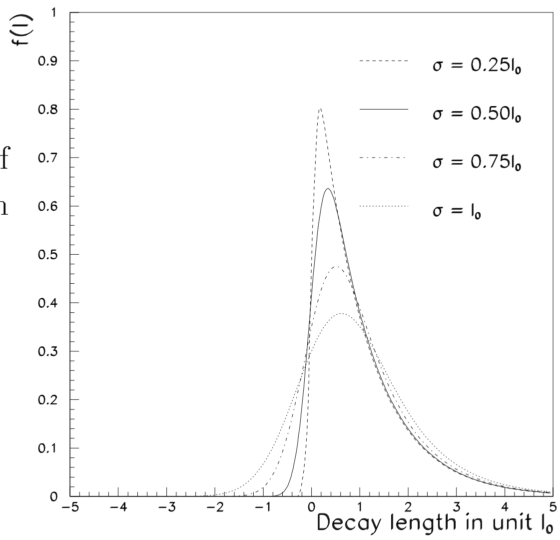

Figure 4.1: Expected length distribution of tau events smeared by the detector resolution

Statistical precision

The precision of the measurement depends both on the τ event sample size and on the uncertainties inherent to the methods. The expected decay length distribution is an exponential (mean $= l_0$), smeared by the detector resolution (δl) as we saw in Fig. 4.1. The statistical precision of the measurement is related to the resolution of the measurement and the sample size N_τ [46]:

$$\frac{\sigma_{\tau_\tau}}{\tau_\tau} = \frac{\sigma_{l_0}}{l_0} = \frac{1}{\sqrt{N_\tau}} \sqrt{1 + (\frac{\delta l}{l})^2}$$

For example when the uncertainty of the decay length measurement is almost equal to the decay length itself, the statistical precision will be $1.4/\sqrt{N_\tau}$ and about 20000 τ events are needed to reach 1% statistical error.

In methods using tau pair events as in $e^+e^- \to \tau^+\tau^-$, the statistical precision of the measurement is

$$\frac{\sigma_{\tau_\tau}}{\tau_\tau} = \frac{0.707}{\sqrt{N_{\tau\tau}}}\sqrt{1+(\frac{\delta l}{l})^2}$$

where $N_{\tau\tau}$ is the number of τ pairs.

Fig. 4.2 (Fig. 4.3) shows the statistical error versus the total number of selected taus (tau pairs). Arrows in figures indicate the numbers of total taus (or tau pairs) produced at one site of LEP ring. The acceptance of each method must be further taken into account. Considering the acceptance of usual IP method using 1-prong and the statistical precision,

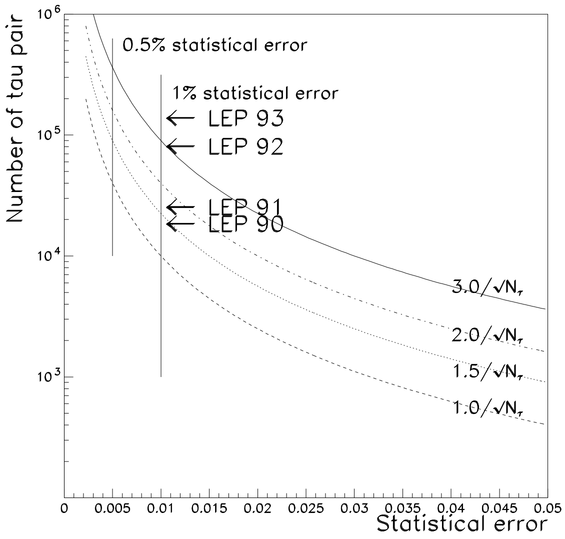

Figure 4.2: Statistical error versus number of taus

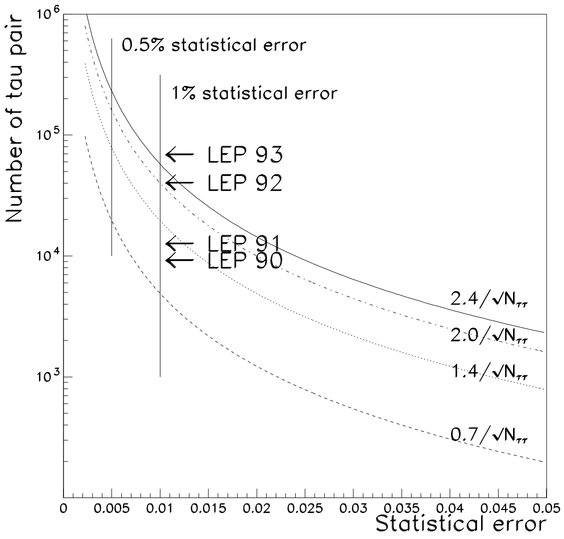

Figure 4.3: Statistical error versus number of tau pairs

$\sim 3.4/\sqrt{N_\tau}$, we can see that one needs at least 120K $\tau^+\tau^-$ events to reach 1% statistical error. In the case of DL method, the statistical precision ($\sim 1.05/\sqrt{N_\tau}$) is much better than that of IP method, but the branching fraction ($\sim 15\%$) of 3-prong decay and the efficiency of the vertex fit ($< 70\%$) limit the sample size, and one needs about 100K $\tau^+\tau^-$ events to reach 1 % statistical error.

4.2 Methods using single τ

4.2.1 Decay Length Method: DL

The Decay Length method applies to 3-prong decays and is the most direct way to measure the lifetime. The decay length method (DL) consists of the reconstruction of the primary vertex (= tau production point), the secondary vertex (= tau decay vertex)), and the tau direction (Fig. 4.4).

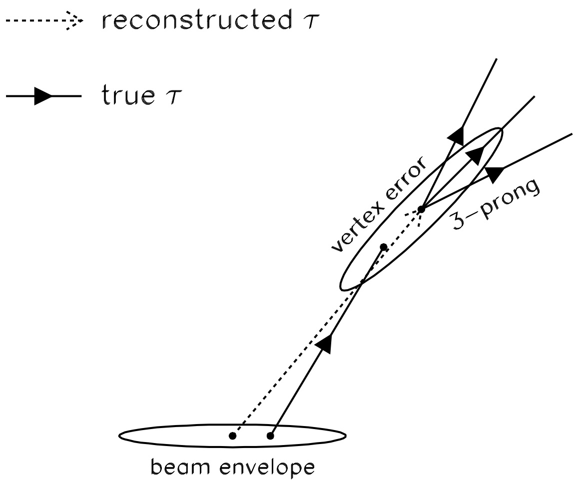

Figure 4.4: Sketch of a three-prong τ decay illustrating the variables used in decay length method. The size of beam is exaggerated compared to the tau decay length.

These 3 quantities are extracted from the following physical observables:

- Tau production point : approximated by the *beam position*. The *beam size* and *position uncertainty* become the uncertainty of the tau production point.

- Tau decay vertex : reconstructed *common vertex* of the measured trajectories of the tau charged daughters. Its error is driven by the *tracking resolution*. The common vertex is normally determined by minimizing the following χ^2,

$$\chi^2 = \sum_{i=1}^{3}(h_i - h(v,p_i))^T C_i^{-1}(h_i - h(v,p_i)) + (v_0 - v)C_{v_0}^{-1}(v_0 - v)$$

where h_i and C_i are the ith track helix parameters and their covariant error matrix, $h(v, p_i)$ is the helix models which are recalculated to contain the vertex v, and v_0 and C_{v_0} are the *a priori* vertex position and its covariant matrix.

- Tau direction : approximated by the *momentum vector* of the tau decay products or the event *thrust axis*. The intrinsic tau direction error due to the missing neutrino momentum gives an additional error in the tau direction estimation.

The production and, in many cases, decay points are determined only in the $r\phi$ plane because of the large uncertainty of the beam size along the z direction and the worse resolution of the tracking in z component [1]. Therefore the 3D decay length l measurement needs also the tau direction information to compensate for the large uncertainty of the beam size along the z direction. The three dimensional tau flight path is obtained from:

$$l = \frac{l_{xy}}{\sin\theta}$$

where θ is the tau polar angle with respect to the beam axis.

The decay length, l, is fitted by minimizing the following χ^2,

$$\chi^2 = (\vec{v}_d - (\vec{v}_o + l\hat{\tau}))^T (C_{oo} + C_{dd} + C_{pp})^{-1} (\vec{v}_d - (\vec{v}_o + l\hat{\tau}))$$

where C_{oo} is the primary vertex error matrix, C_{dd} is the fitted vertex's, and C_{pp} is the error matrix of the tau direction (p denotes the sum vector or thrust axis). Since the smearing from the tau direction error is proportional to the decay length, C_{pp} is given by $C_{pp} = l^2\sigma_p^2 \cdot (\delta_{ij} - \hat{p}_i\hat{p}_j)$ where σ_p is the direction error.

Fig. 4.5 shows the decay length distribution of ALEPH analysis.

Likelihood : Gaussian convoluted exponential function

Considering the exponential distribution of tau decay length and assuming a gaussian error on the decay length measurements, we get the event density function, $\mathcal{F}$, to be used in the estimation of the maximum likelihood as the exponential distribution convoluted with a gaussian:

$$\mathcal{F}(l, \sigma; l_0) \quad = \quad \int_0^\infty (\frac{1}{l_0} exp(-\frac{x}{l_0})) \frac{1}{\sqrt{2\pi}\sigma} \exp(-\frac{(x-l)^2}{2\sigma^2}) dx$$

[1] ALEPH has a good enough resolution in z to have 3-dimensional vertex

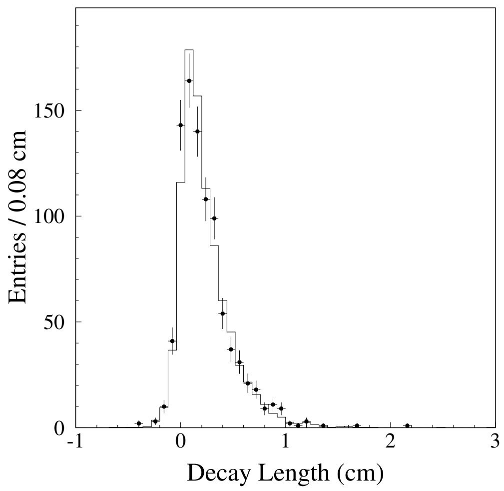

Figure 4.5: Decay length distribution of ALEPH 1991 measurement

$$= \frac{1}{2l_0}\exp(\frac{\sigma^2}{2l_0^2} - \frac{l}{l_0})\,\mathrm{erfc}[\frac{1}{\sqrt{2}}(\frac{\sigma}{l_0} - \frac{l}{\sigma})] \tag{4.1}$$

where l is a measured decay length and σ is an estimated error of the decay length.

Results and comments

Since DL method uses 3-prong tau decays, it suffers from low statistics due to the low branching fraction ($\sim$ 15%). Strong requirements on track and vertex qualities [2] make another factor reducing the sample size. The low efficiency comes from various reasons: backgrounds, fake 3-prong like $\pi ee\gamma$ from conversion, and most of all, pattern recognition problems in VDET hit association, etc..

Tab.4.1 summarizes the recent results from the LEP experiments [47], [48] [63]. We see that the statistical precision $2.0/\sqrt{N_\tau}$ in 1989 and 1990 ALEPH measurement is highly improved in 1991 and 1992 by the VDET installation: $1.01/\sqrt{N_\tau}$ and $1.05/\sqrt{N_\tau}$ respectively. These values are consistent with the expected statistical precision $P = 1.05/\sqrt{N_\tau}$ when we consider that the decay length measurement error is about 33% (760μm) of the mean decay length (2300μm) in ALEPH.

[2] $\sim$ 40 % in ALEPH, $\sim$ 25 % in DELPHI, $\sim$ 70 % in OPAL. ALEPH uses full (3-dim.) decay vertex in analysis.

	ALEPH		DELPHI		OPAL	
Year	τ_τ	N_τ	τ_τ	N_τ	τ_τ	N_τ
1989+1990	$288 \pm 23 \pm 12$	629	-	-	-	-
1991	$295 \pm 10 \pm 5$	901	$303 \pm 13 \pm 7$	823	$283.5 \pm 7.4 \pm 4.8$	2050†
1992	$290.0 \pm 5.8 \pm 2.1$	2793	$291 \pm 8 \pm 8$	1200	$284.5 \pm 4.8 \pm 2.2$	4671
1993	-	-	-	-	$292.6 \pm 5.3 \pm 2.2$	4417

†1990+1991

Table 4.1: Tau lifetime measurements using DL method

4.2.2 Classical Impact Parameter method: IP

Conceptually the impact parameter method is similar to the decay length method since it measures the transverse decay length l_{xy} and extracts a tau flight path from $l = \frac{l_{xy}}{\sin\theta}$. The difference in the impact parameter method is in the calculation of l_{xy}. The transverse decay length is determined by the impact parameter of a track as follow

$$l_{xy} = \frac{d_0}{\sin\psi_{xy}}$$

where ψ_{xy} is the projected angle between the track and the τ direction. This technique does not need to fit a vertex, so it is used generally in 1 prong tau decay events. It benefits from high statistics of 1-prong decays ($\sim 85\%$ of tau decays).

Fig.4.6 illustrates the physical observables and the true quantities in the IP method. The d_0 measurement is smeared not only by the tracking resolution but also by the beam size and position uncertainty (the uncertainty on the tau production position is $\sim 110\mu$ on x, $\sim 10\mu$ on y). In addition the term ψ_{xy} induces a large smearing on the decay length measurement because of the large error on the tau direction from the thrust axis and the smallness of the decay angle ψ_{xy}.

Results and comments

Tab.4.2 summarizes the recent results from the LEP experiments using the impact parameter method [47] [58] [62]. ALEPH and DELPHI stopped the analysis because they moved to new methods using τ^+ and τ^- pairs as a whole. The statistical precisions achieved by OPAL in 1993 is about $3.4/\sqrt{N_\tau}$ [3] With this precision, more than 110K

[3] The statistical precision achieved in 1992 data is better than that of 1993 due to smaller beam size.

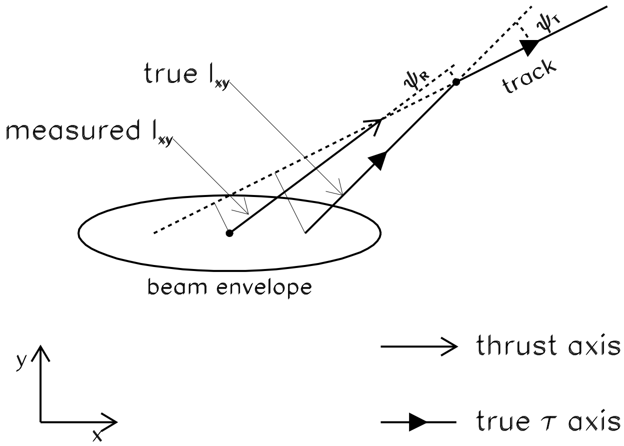

Figure 4.6: Illustration of IP method: The size of beam is exaggerated compared to the tau decay length.

	ALEPH/DELPHI		L3		OPAL	
Year	τ_τ	N_τ	τ_τ	N_τ	τ_τ	N_τ
1989+1990	$286 \pm 18 \pm 11$	$6954^{a)}$	-	-	-	-
1991	$304 \pm 11 \pm 6$	$6113^{b)}$	$288 \pm 21 \pm 12$	$5227^{c)}$	$295.5 \pm 6.9 \pm 3.3$	$25653^{d)}$
1992	-	-	$291.1 \pm 8.5 \pm 4.1$	11122	$288.1 \pm 4.4 \pm 2.7$	35168
1993	-	-	$303.2 \pm 9.7 \pm 4.7$	10839	$286.0 \pm 5.3 \pm 2.5$	32703

$^{a)}$ ALEPH, $^{b)}$ DELPHI, $^{c)}$ $\tau \to l\nu\nu + \tau \to 1hn\pi^0\nu$, $^{d)}$ 1990+1991

Table 4.2: Tau lifetime measurements using IP method

accepted tau pairs in this method are needed to reach 1 % statistical error.

4.3 Methods using the tau pairs

Both methods explained above use the tau production position, the tau direction, and the tau decay vertex or the impact parameter to measure the tau decay length in a given event. Thus, uncertainties affecting any of these 3 variables introduce errors in the measurement of the decay length.

Since we know τ^+ and τ^- are produced back-to-back at an e^+e^- collider like LEP, we may hope to remove at least one or two uncertainties using this characteristic, to be left only with tracking resolution.

The methods we explain in this section are the methods recently developed, and allowing the tau lifetime measurements with the best statistical error (IPS) or the best systematic error (IPD).

4.3.1 Impact Parameter Difference method: IPD

The first attempt to overcome the limitations of the classical impact parameter method started with S. Wasserbaech in ALEPH, who developed the IPD technique [49] [50]. He noticed that the back-to-back nature of tau pair produced in the e^+e^- collider makes the quantity IPD, $d_0^+ - d_0^-$, independent of the tau direction.

In the x-y plane, the impact parameter is related to the projected decay length (l_{xy}) and the projected tau decay angle (ψ_{xy}) by $d_0 = l_{xy} \sin\psi_{xy}$. Considering two tau decays, the impact parameter difference, $d_0^+ - d_0^-$, is

$$d_0^+ - d_0^- = l_{xy}^+ \sin\psi_{xy}^+ - l_{xy}^- \sin\psi_{xy}^-$$

For given ψ_{xy}^+ and ψ_{xy}^-, the average IPD is,

$$< d_0^+ - d_0^- >=< l_{xy} > (\sin\psi_{xy}^+ - \sin\psi_{xy}^-)$$

The tau decay angle, ψ, is small enough ($\sim$ 25mrad at LEP) to allow the approximation, $\sin\psi_{xy} \sim \psi_{xy}$:

$$< d_0^+ - d_0^- >=< l_{xy} > (\psi_{xy}^+ - \psi_{xy}^-)$$

Under the assumption that the τ^+ and τ^- are back-to-back in the x-y projection, $\psi^+_{xy} - \psi^-_{xy}$ becomes the azimuthal angle difference between the two charged tracks ($\psi^+_{xy} - \psi^-_{xy} = \Delta\phi_0 \equiv \phi^+_0 - \phi^-_0 \pm \pi$). Thus, the tau lifetime is determined by scaling l_{xy} using tau polar angle (θ) as in the IP method and measuring the slope of the linear plot $< d^+_0 - d^-_0 >$ as a function of $\sin\theta\Delta\phi_0$.

$$< d^+_0 - d^-_0 > = < l_{xy} > \Delta\phi_0 = (\beta\gamma c\tau_\tau)\sin\theta\Delta\phi_0 \tag{4.2}$$

Fig. 4.7(a) shows the 2 dimensional distribution of $d^+_0 - d^-_0 (\equiv Y)$ and $\sin\theta\Delta\phi_0 (\equiv X)$. Fig. 4.7(b) shows the y-axis profile of Fig. 4.7(a). The decline of Fig. 4.7(b) determines the lifetime.

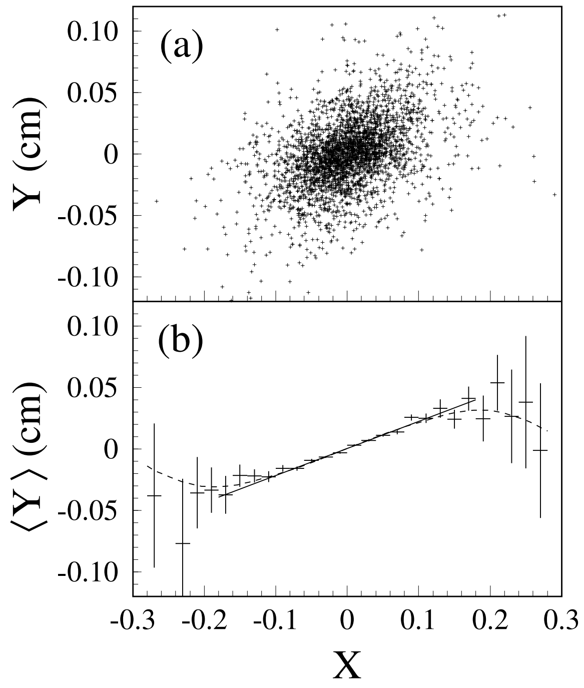

Figure 4.7: (a) Y versus X (b) $< Y >$ versus X. The line shows the fit result within $|X| < 0.18$

Results

Tau lifetime measurements using this technique have been done mainly by ALEPH and DELPHI collaborations at LEP. Tab.4.3 summarizes the results [49] [50] [61]. The statistical precision is about $2.0/\sqrt{N_{\tau\tau}}$ both in ALEPH and DELPHI. When we transform this statistical precision into the form used in the classical IP method, this value corresponds to $2.8/\sqrt{N_\tau}$. [4]

	ALEPH		DELPHI	
Year	τ_τ	$N_{\tau\tau}$	τ_τ	$N_{\tau\tau}$
1989+1990	$285 \pm 17 \pm 6$	3470	-	-
1991	$316 \pm 12 \pm 3$	3343	$299 \pm 11 \pm 6$	2873
1992	$288.1 \pm 5.4 \pm 1.2$	10983	$295.9 \pm 7.0 \pm 3.3$	5965
1993	-	-	$289.0 \pm 7.2 \pm 4.5$	5789

Table 4.3: Tau lifetime measurements using IPD methods

4.4 Impact Parameter Sum method: IPS

Another approach, IPS, was started also by ALEPH, noticing that the uncertainty on the production position cancels out in the quantity $d_0^+ + d_0^-$ (Impact Parameter Sum) for parallel tracks [52]. IPS smearing in the case of non parallel tracks is given by Eq. 4.3:

$$\sigma_\delta = 2\sigma_x^{BS} \sin\bar{\phi} \sin\Delta\phi \oplus 2\sigma_y^{BS} \cos\bar{\phi} \sin\Delta\phi \tag{4.3}$$

where ϕ is an azimuthal angle of the track, $\bar{\phi} = (\phi_1 + \phi_2)/2$, and $\Delta\phi = \phi_1 - \phi_2 - \pi$. The beam size along the x axis is large ($\sim 180\mu$m) but it contributes only few microns to the IPS smearing since angular difference between two charged tracks is small, $\Delta\phi \sim 40$mrad. However IPS technique suffers from the poor estimation of the decay angle ψ_{xy}.

Likelihood function

Different decay topologies make different true IPS distributions. When $\psi_1' > 0$ and

[4] The statistical precision is worse in 1993 analyses due to enlarged beam size.

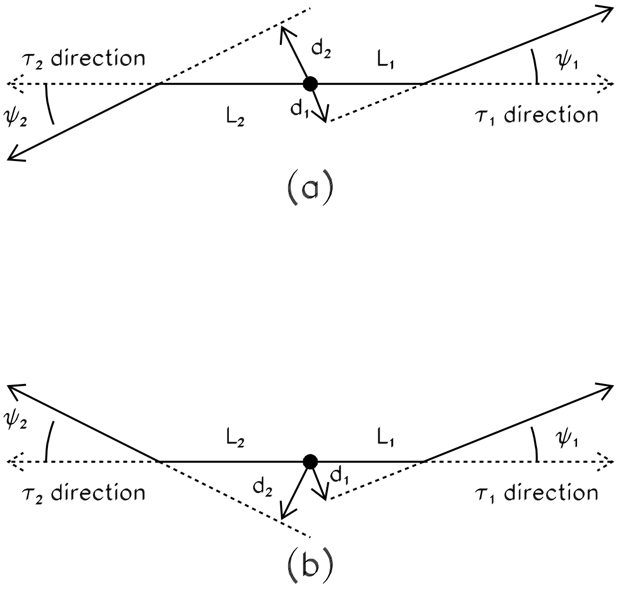

Figure 4.8: Illustration of 1-1 tau decay projected to the xy plane: a) $\psi_1' > 0$ and $\psi_2' > 0$, b) $\psi_1' > 0$ and $\psi_2' < 0$. Angles are defined as $\phi_{track} - \phi_{tau}$.

$\psi_2' > 0$ as shown in Fig 4.8(a), the true IPS distribution is:

$$\mathcal{D}(\Sigma d_0, \psi_1', \psi_2', \theta; l) = \begin{cases} \dfrac{\exp(-\delta'/l\sin\theta\sin\psi_1') - \exp(-\delta'/l\sin\theta\sin\psi_2')}{l\sin\theta(\sin\psi_1' - \sin\psi_2')} & \delta' > 0 \\ \\ 0 & \delta' < 0 \end{cases}$$

where $\delta'(\equiv \sum d_0)$ is true IPS, θ denotes the tau polar angle. On the other hand if $\psi_1' > 0$ but $\psi_2' < 0$ as shown in Fig 4.8(b), the distributions become:

$$\mathcal{D}(\Sigma d_0, \psi_1', \psi_2', \theta; l) = \begin{cases} \dfrac{\exp(-\delta'/l\sin\theta\sin\psi_1')}{l\sin\theta(\sin\psi_1' - \sin\psi_2')} & \delta' > 0 \\ \\ \dfrac{\exp(-\delta'/l\sin\theta\sin\psi_2')}{l\sin\theta(\sin\psi_1' - \sin\psi_2')} & \delta' < 0 \end{cases}$$

The expected IPS distribution in the real experiment is obtained by convolving the true δ' distribution with an IPS resolution function, $\mathcal{R}$, assumed to be a gaussian. Additional smearings from the decay angles ($\psi_{1,2}$) measurements however must be considered, (so called h function), which have to be integrated numerically.

Finally, the tau lifetime is extracted by searching the maximum likelihood of the IPS density function:

$$\mathcal{F}(\delta', \psi_1, \psi_2, \theta_{thr}, \sigma_{ips}; l_0) = \int d\psi_1' d\psi_2' h(\psi_1, \psi_2, \psi_1', \psi_2') \int d\delta' \mathcal{R}(\delta, \delta', \sigma) \mathcal{D}(\delta', \psi_1', \psi_2', \theta_{thr})$$

Results

Tau lifetime measurements using IPS technique have been performed by ALEPH and DELPHI collaborations at LEP. Tab. 4.4 summarizes the results [52] [53] [56] [60]. In

	ALEPH		DELPHI	
Year	τ_τ	$N_{\tau\tau}$	τ_τ	$N_{\tau\tau}$
1991	$290 \pm 6 \pm 6$	2557	$304 \pm 9 \pm 6$	-
1992	$295.0 \pm 3.9 \pm 4.4$	10464	$296.8 \pm 7.1 \pm 3.5$	2823
1993	$-$		$296.6 \pm 6.5 \pm 4.1$	4350

Table 4.4: Tau lifetime measurements using IPS methods

the case of DELPHI, the statistical precision $\sim 1.4/\sqrt{N_{\tau\tau}}$ is slightly worse than that of ALEPH ($\sim 1.3/\sqrt{N_{\tau\tau}}$) because DELPHI does not use the information of tau direction. The statistical precision of IPS method corresponds to $1.9/\sqrt{N_\tau}$ which is much more pricise than that of IPD method. But the method confronts with the limit of systematic control due to the uncertainties on the tracking resolution and the non-gaussian tails.

Momentum dependent IPS method: MIPS

A modified version of the IPS technique (MIPS) was developed by H.W. Kim [54] also in ALEPH collaboration. Instead of measuring ψ from the charged track and the thrust axis, the MIPS uses the track momentum which is kinematically correlated with the decay angle. The statistical error $1.3/\sqrt{N_{\tau\tau}}$ obtained in the original IPS is reduced to $1.2/\sqrt{N_{\tau\tau}}$ by using MIPS but the method suffers also from the same systematic limit as in IPS.

4.5 Another new method?

Tab. 4.5 summarizes the acceptances, statistical precisions, and systematic errors of the various methods:

Method	Acceptance†($N_{\tau\tau}^{prod}$)	Precision	Systematic error (%)
DL	~ 0.08	$\sim 1.1/\sqrt{N_\tau}$	$\sim 0.7\%$
IP	~ 1.00	$\sim 3.4/\sqrt{N_\tau}$	$\sim 0.9\%$
IPD	~ 0.34	$\sim 2.0/\sqrt{N_{\tau\tau}}$	$\sim 0.4\%$
IPS(MIPS)	~ 0.32	$\sim 1.3/\sqrt{N_{\tau\tau}}$	$\sim 1.5\%$

†$\tau\tau$ event selection efficiency $\times$ branching fraction $\times$ acceptance of cuts ($\times$ 2 for DL and IP method)

Table 4.5: Acceptance, statistical precision, and systematic error of the tau lifetime measurements

Tab. 4.6 shows the observed or expected numbers of tau data events in ALEPH according to the TSLT efficiency and acceptances of DL, IPD, IPS methods. The acceptance of IP method and corresponding sample sizes ($N_\tau^{1-prong}$) are taken from OPAL analysis. We assumed the analysis on 1993 and 1994 data will be performed as 1992 analysis with

Year	$\int Ldt\ (pb^{-1})$	$N_{Z^0\rightarrow q\bar{q}}$	$N_{\tau\tau}^{prod}$	$N_{\tau\tau}^{sel}$	$N_\tau^{1-prong}$	$N_\tau^{3-prong}$	N_τ^{1-1}
1989+1990	8.1	179K	8.7K	6.5K	7K	0.6K	3.3K
1991	12.2	294K	14K	11K	10K	0.9K	3.4K
1992	23.4	711K	34K	25K	35K	2.8K	11.5K
1993	33.2	675K	33K	24K	33K	2.7K	11K
1994	58.7	1.76M	65K	50K	65K	5.2K	21K
Total	136	3.62M	155K	116K	150K	12.2K	50.2K

Table 4.6: Number of ALEPH tau data. $N_\tau^{1-prong}$, $N_\tau^{3-prong}$, and N_τ^{1-1} are the expected sizes of data samples after their specific selections.

the same detector performances.

Using up to 1994 data, statistical errors of the tau lifetime will approach

- DL : 0.95 %
- IP : 0.89 %
- IPD : 0.94 %
- IPS : 0.58 %

The tau lifetime is likely to be measured with a statistical uncertainty as small as 1.3 fs. However the measurement will be limited by the systematic error ($\sim$ 3fs) if the systematic uncertainties of IPS like methods are not reduced.

To overcome the systematic limit on the lifetime uncertainty and to profit from the increasing statistics, it is worth developing a new method less affected by systematical uncertainty and more precise. There have been some attempts and many ideas for improvement using the z readout of VDET, energy measurement of neutrals, and/or the kinematics in hadronic decay channels. Also there have been continuing demands to extract tau lifetime from 1-prong side in 1-3 tau decays, which give statistically independent result from the DL method since the latter uses only 3-prong tau decays. This thesis gives an answer, *3DIP method*, to the above ideas and questions. The 3DIP method uses the z readout of VDET and full reconstruction of tau decay products, charged and neutral. In addition, the method uses 1-3 tau decays as well as 1-1 decays, and measures the lifetime from 1-prong decays. The last part of this thesis is devoted to the 3DIP analysis.

Chapter 5

Kinematics of Hadronic-hadronic $\tau\tau$ Decay Events

5.1 Tau decay angle in hadronic channels

For non-leptonic tau decay modes, there is only one neutrino in the final state and the kinematics of the tau decay can be considered as a 2-body problem. These events are mainly $\tau \to \pi\nu_\tau$, $\tau \to \rho\nu_\tau$, and $\tau \to a_1\nu_\tau$, $\tau \to (n\pi)\nu_\tau$ and appear as 1-prong or 3-prong $+n\pi^0$. The kinematics can be applied in 1-prong as well as 3-prong decays. From now on, each hadronic final state, π, ρ, a_1, $(n\pi)$, ..., etc., is called just "*hadron*" for simplicity and will be denoted as "h".

The 4-momentum of the hadron can be reconstructed as the sum of the 4-momenta of its charged and neutral daughters:

$$h^\mu = \sum c^\mu + \sum \pi^{0\mu} + \sum \gamma^\mu$$

For a hadronic tau decay, the tau to hadron decay angle can then be reconstructed using 2-body kinematics:

$$\cos\psi = \frac{2E_\tau E_h - m_\tau^2 - m_h^2}{2P_\tau P_h} \tag{5.1}$$

where E, P, m are energy, momentum and mass of τ or h. The tau energy is equal to the beam energy ignoring radiative corrections and m_τ is set to 1.777GeV/c^2.

Fig. 5.1 shows the difference between the reconstructed decay angle and the true one. The superimposed curve is a fit with three gaussians. The decay angle resolution is about

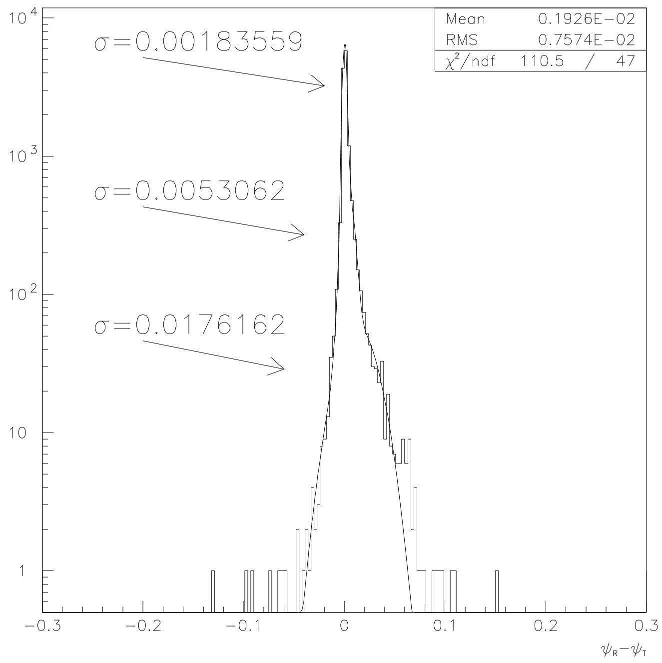

Figure 5.1: Difference between the reconstructed decay angle and the true decay angle

2 to 5 mrad in the two central gaussian peaks. The events in tails ($\sim$ 18mrad) come mainly from bad reconstructions of hadrons. There is also a small contribution ($\sim 11\%$) from hard non-collinear $\tau\tau$ events. [1]

5.2 Tau axis solutions in momentum space

The unknown tau axis must lie on a cone around the hadron direction with opening angle equal to the tau decay angle, ψ. In the following, this will be called the decay angle constraint. In the momentum space, two equations are obtained from the decay angle constraints in both hemispheres:

$$\begin{aligned} \hat{\tau}^+ \cdot \hat{h}^+ &= \cos\psi^+ \\ \hat{\tau}^- \cdot \hat{h}^- &= \cos\psi^- \end{aligned} \tag{5.2}$$

[1] The distribution is not symmetric because there exists a mathematical limit on the reconstructed decay angle ψ, $\psi = 0$, when $\cos\psi > 1$. $\cos\psi$ defined as Eq. 5.1 can be larger than 1 ($\sim 5\%$ of tau events).

When the two taus are back-to-back as generated in $Z^0 \to \tau^+\tau^-$ at Z^0 pole, $\hat{\tau} \equiv \hat{\tau}^+ = -\hat{\tau}^-$, the decay angle constraint equations are rewritten as

$$\hat{\tau} \cdot \hat{h}^+ = \cos\psi^+$$

$$\hat{\tau} \cdot \hat{h}^- = -\cos\psi^-$$

Combining the two equations and using the vector identity $\vec{A} \times (\vec{B} \times \vec{C}) = \vec{B}(\vec{A} \cdot \vec{C}) - \vec{C}(\vec{A} \cdot \vec{B})$,

$$(\hat{h}^+ \times \hat{h}^-) \times \hat{\tau} = \hat{h}^+ \cos\psi^- + \hat{h}^- \cos\psi^+$$

The term, $\hat{h}^+ \cos\psi^- + \hat{h}^- \cos\psi^+$, will be defined as $\vec{H}$ and called the perpendicular axis. The cross vector $\hat{h}^+ \times \hat{h}^-$ will be defined as $\vec{h}_\perp$. The above equation is then written:

$$\vec{h}_\perp \times \hat{\tau} = \vec{H} \tag{5.3}$$

Since $|\hat{\tau}| = 1$, finally we get,

$$\tau_z^2 |h_\perp|^2 - 2(\vec{H} \times \vec{h}_\perp)_z \tau_z + H^2 - H_z^2 - h_{\perp z}^2 = 0 \tag{5.4}$$

This second order equation has two solutions for the tau direction, that gives a well-known two-fold ambiguity (Fig. 5.2). It can be solved by denoting $a = |h_\perp|^2$, $b = -(\vec{H} \times \vec{h}_\perp)_z$ and $c = H^2 - H_z^2 - h_{\perp z}^2$.

$$\begin{aligned}
\tau_z &= \frac{-b \pm \sqrt{b^2 - ac}}{a} \\
\tau_x &= \frac{h_\perp^x}{h_\perp^z}\tau_z + \frac{H_y}{h_\perp^z} \\
\tau_y &= \frac{h_\perp^y}{h_\perp^z}\tau_z - \frac{H_x}{h_\perp^z}
\end{aligned}$$

The two-fold ambiguity can be simply understood by geometrical considerations. In Fig. 5.2, one of the hadron directions is reversed to show the intersections, $\hat{h}_1$ is the reversed direction of $\hat{h}^-$. The two intersections of the cones can be interpreted as the two tau axis solutions, $\hat{\tau}_1$ and $\hat{\tau}_2$. The vector $\vec{H}$ is normal to the plane determined by the two tau axis solutions (*the ambiguity plane*). The vector $\vec{h}_\perp (\equiv \hat{h}^+ \times \hat{h}^-)$ lies in the ambiguity plane and is directed always along the external bisector of $\hat{\tau}_1$ and $\hat{\tau}_2$. A third vector $\vec{A}_h$, the internal bisector of the $\hat{\tau}_1$ and $\hat{\tau}_2$, is along the intersection of the ambiguity plane and the plane defined by the two hadrons.

The vectors, $\vec{H}$, $\vec{A}_h$, and $\vec{h}_\perp$ make a orthogonal coordinate system. In this coordinate system, the two tau axis solutions lie in the $h_\perp$-A_h plane and the two hadrons lie in the A_h-H plane.

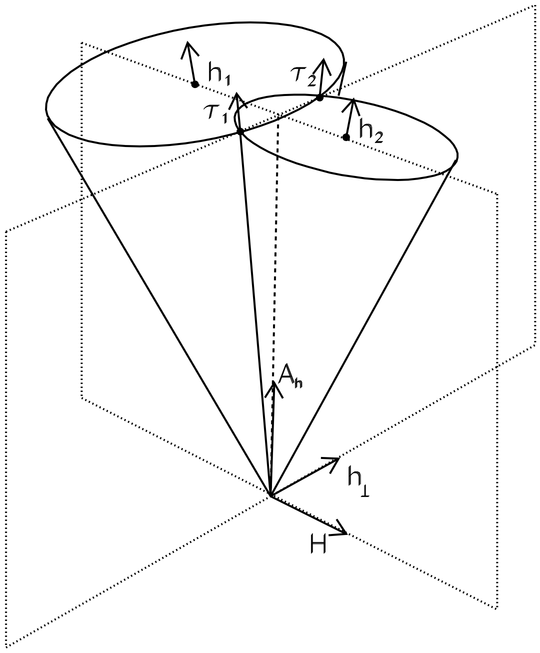

Figure 5.2: Geometrical view of two kinematical tau axis solution

The use of the $H - h_\perp - A_h$ coordinate system in the lifetime measurement is the basic idea of the 3DIP method.

5.3 Configuration of two tau axes and hadron tracks in real space - Case of fully reconstructed hadrons

In this section, we will show the way to resolve the 2-fold ambiguity in case the hadron vectors are fully reconstructed. It is assumed here that we know the hadron direction $\hat{h}$ and some fixed point on the hadron track, for instance, the point of minimum approach to the beam (d_0, z_0). We will show that only one solution is consistent with a tau decay and the other solution has no physical meaning.

Let us define $\vec{\tau}_0$ the tau pair origin and $l^\pm$ the decay lengths of the two taus. In addition, let us define $\vec{h}_0^\pm$ as measured points on the hadron tracks. These can be the points of minimum approach to the beam or any measurable points. For each hemisphere, the decay point in space, $\vec{V}$, is related to $\vec{\tau}_0$ and $\hat{\tau}$, or to $\vec{h}_0$ and $\hat{h}$ as follow (Fig. 5.3):

$$\vec{V} = \vec{\tau}_0 + l\hat{\tau} = \vec{h}_0 + \eta\hat{h}$$

where η is the distance between $\vec{h}_0$ and the decay point along the hadron track. Combining

Figure 5.3: Illustration of the two hadron tracks, $\tau^{\pm}$, and unknowns $\eta^{\pm}$

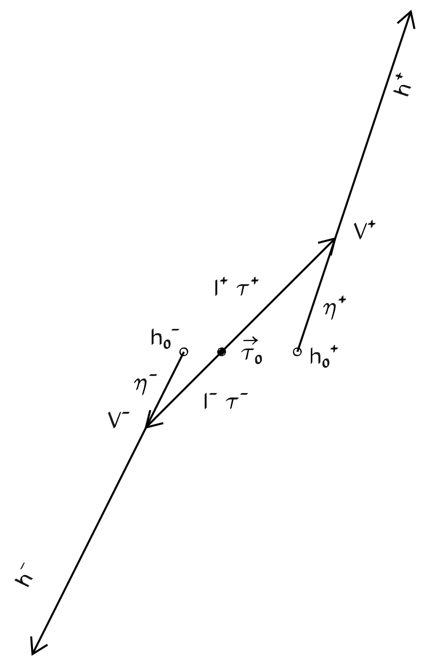

both hemispheres, $\vec{\tau}_0$ cancels out:

$$l^+\hat{\tau}^+ - l^-\hat{\tau}^- = \vec{h}_0^+ - \vec{h}_0^- + \eta^+\hat{h}^+ - \eta^-\hat{h}^-$$

With the assumption of back-to-back taus, $\hat{\tau}^+ = -\hat{\tau}^-$, the above vector equation is simplified as follow:

$$(l^+ + l^-)\hat{\tau} = \delta\vec{h}_0 + \eta^+\hat{h}^+ - \eta^-\hat{h}^- \tag{5.5}$$

where $\hat{\tau} \equiv \hat{\tau}^+ = -\hat{\tau}^-$ and $\delta\vec{h}_0 \equiv \vec{h}_0^+ - \vec{h}_0^-$.

Using the two tau decay angles determined by kinematics, the 3 unknowns, $\eta^{\pm}$ and $l^+ + l^-(\equiv \chi)$, can be reduced to one. Substitution of Eq. 5.5 into the equations of the decay angle constraints (Eq. 5.2) gives the following result (See App. E).

$$\eta^+ = a^+\chi - b^+, \qquad \eta^- = a^-\chi - b^-$$

where,

$$\begin{aligned} a^{\pm} &= \vec{H} \cdot \hat{h}^{\mp}/h_{\perp}^2 \\ b^{\pm} &= \vec{h}_{\perp} \cdot (\delta\vec{h}_0 \times \hat{h}^{\mp})/h_{\perp}^2 \end{aligned}$$

Finally we get the tau axis vector equation with only one unknown, χ:

$$\boxed{\chi\hat{\tau} = \chi\vec{A}_h + \vec{D}_h} \tag{5.6}$$

where,

$$\begin{aligned}\vec{A}_h &= \vec{H} \times \vec{h}_\perp / h_\perp^2 \\ \vec{D}_h &= (\vec{h}_\perp \cdot \delta\vec{h}_0)\vec{h}_\perp / h_\perp^2\end{aligned}$$

The decay length sum χ, then, can be directly derived from Eq. 5.6 using $|\hat{\tau}| = 1$:

$$\begin{aligned}\chi^2 &= (\chi\vec{A}_h + \vec{D}_h) \cdot (\chi\vec{A}_h + \vec{D}_h) \\ &= \chi^2|\vec{A}_h|^2 + |\vec{D}_h|^2\end{aligned}$$

Therefore,

$$\boxed{\chi = \pm\frac{|\vec{D}_h|}{\sqrt{1 - |\vec{A}_h|^2}}}$$

The positive solution corresponds to the good tau direction.

The vector $\vec{A}_h$ was already introduced in the previous section and is parallel to the intersection of the plane containing h^+ and h^- and the ambiguity plane. $|\vec{A}_h|$ is smaller than 1 when the two cones intersect. $(1 - |\vec{A}_h|)$ is identical to the discriminant of Eq. 5.4.

$\vec{D}_h$ is the minimum approach vector between h^- and h^+. $\vec{D}_h$ is along $\vec{h}_\perp$ and consequently orthogonal to $\vec{A}_h$. Fig. 5.4 is the geometrical interpretation of the tau axis vector equation (Eq. 5.6).

Considering that $\vec{D}_h$ is orthogonal to $\vec{A}_h$, $\chi\hat{\tau} \cdot \vec{D}_h = |\vec{D}_h|^2$. Then the real tau axis should satisfy the condition, $\hat{\tau} \cdot \vec{D}_h > 0$, due to the positive decay length. In Fig. 5.4 $\hat{\tau}_1$ represents a real tau solution, *i.e*, $\hat{\tau}_1 \cdot \vec{D}_h > 0$. The second solution, $\hat{\tau}_2$ ($\hat{\tau}_2 \cdot \vec{D}_h < 0$), would result in a backward emission of the hadrons in the τ decays.

Thus when the vector $\vec{D}_h$ is measured, it can be used to select the original tau axis by checking the scalar product:

$$\begin{aligned}\hat{\tau}_{true} \cdot \vec{D}_h &> 0 \\ \hat{\tau}_{false} \cdot \vec{D}_h &< 0\end{aligned}$$

However, the measurement of $\vec{D}_h$ requires the full reconstruction of hadron vectors, in direction and position in space, which is achievable only for $\tau \to \pi(K)\nu_\tau$ decays or in 3 prong decays where the decay vertex can be sufficiently well measured.

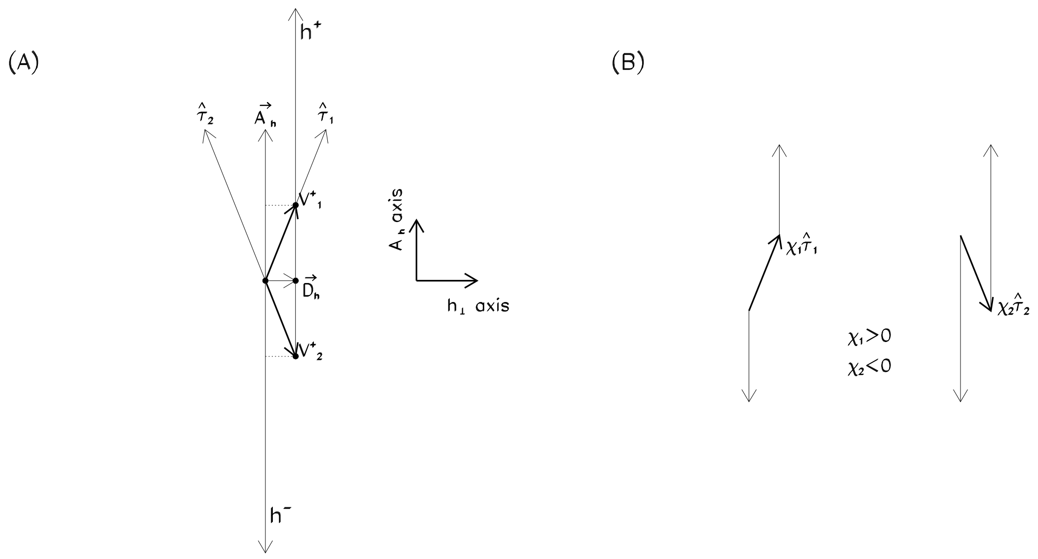

Figure 5.4: (A) τ decay configuration in the $A_h - h_\perp$ plane. The vectors $\vec{h}^+$ and $\vec{h}^-$ appear parallel in that projection. (B) Only one solution, $\hat{\tau}_1$, satisfies the equation $\hat{\tau} = \vec{A}_h + \vec{D}_h/\chi$ with a physically meaningful positive χ.

A similar calculation of the relation between the minimum distance between two pions (here $\vec{D}_h$) and the decay length sum (χ) was performed by J. H. KUHN [66].

The tau axis selection using this idea was checked on Monte Carlo events. In the events where both τs decay to π, the efficiency of *good tau axis* selection is around 85 % , where the *good tau axis* is defined as the solution closer to the MC true tau axis. The 15 % of wrong choice is mainly due to the infinitesimal size of $\vec{D}_h$ and/or its large tracking error. The kinematical tau axis resolution without selection (or in the case of random selection) is $\sim$ 22mrad. When we apply the selection criteria using $\vec{D}_h$, the resolution decreases to $\sim$ 6.7mrad. Fig. 5.5 shows the angle between the selected tau axis and the MC true axis in the $\pi - \pi$ events.

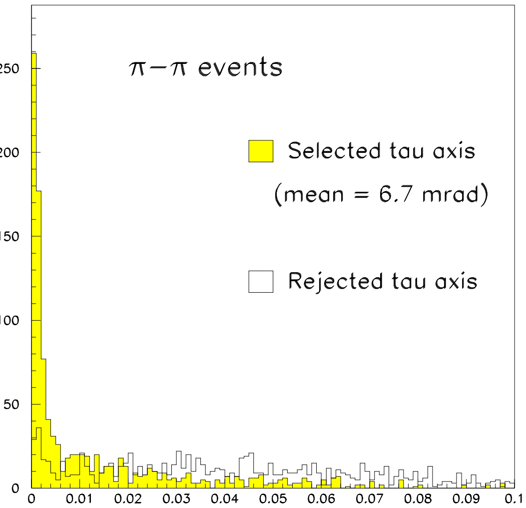

Figure 5.5: Angle between the selected tau axis and the MC true axis in the $\pi - \pi$ events

5.4 Configuration of two tau axes and charged tracks in real space - General case

The ALEPH tracking devices allow a full reconstruction of the charged tracks with high precision ($\Delta p/p^2 \sim 0.6 \times 10^{-3}(GeV/c)^{-1}$ and $\sigma_{d_0} \sim 23\mu$m, $\sigma_{z_0} \sim 29\mu$m). For neutrals, like photons or reconstructed π^0s, the direction is well measured ($\sigma_\theta \approx \sigma_\phi \sim 3/\sqrt{E}$ mrad) with the assumption that the neutrals come from the interaction region. The neutrals have no information corresponding to d_0 and z_0 of a charged track. Therefore, a hadron, mother of charged tracks and neutrals, can not be reconstructed in the direction and the position except in the case of pure charged modes. For this reason, in modes with neutrals, while $\vec{A}_h$ (depending on the direction) can still be reconstructed with a few milli-radian resolution, the vector $\vec{D}_h$ (depending on the direction and position) can not be precisely measured due to the missing d_0 and z_0 of the neutrals. In this section we will study the possiblities of generalization of the selection mechanism to the events with neutrals.

Fig. 5.6 shows a tau decay to a charged track and neutrals. Let us define a 3D-space point $\vec{c}_0$ of a charged track, corresponds to $\vec{h}_0$ in Fig. 5.3, as the point of minimum approach (d_0 and z_0) of the track. Again we can obtain the following equations in both

Figure 5.6: Schematic view of the tau decay to one charged track and multiple neutrals

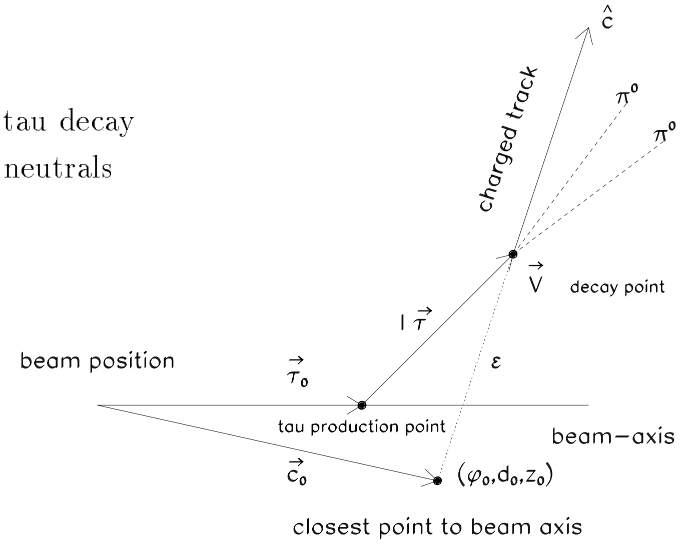

hemispheres:

$$\vec{\tau}_0 + l^+\hat{\tau}^+ = \vec{c}_0^{\,+} + \epsilon^+\hat{c}^+$$
$$\vec{\tau}_0 + l^-\hat{\tau}^- = \vec{c}_0^{\,-} + \epsilon^-\hat{c}^-$$

and the combined result as before is,

$$\chi\hat{\tau} = (\delta\vec{c}_0 + \epsilon^+\hat{c}^+ - \epsilon^-\hat{c}^-) \quad (5.7)$$

where ϵ is the unknown distance between $\vec{c}_0$ and the decay point along the charged track.

The equations are exactly of the same form as the equations of the hadron vectors. Using the tau decay angle constraint, Eq. 5.2, the tau axis satisfies the vector equation similar to Eq. 5.6 (See App. E).

$$\boxed{\chi\hat{\tau} = \chi\vec{A}_c + \vec{D}_c} \quad (5.8)$$

where,

$$\begin{aligned}\vec{A}_c &= \vec{H} \times \vec{c}_\perp / (\vec{h}_\perp \cdot \vec{c}_\perp) \\ \vec{D}_c &= (\vec{c}_\perp \cdot \delta\vec{c}_0)\vec{h}_\perp / (\vec{h}_\perp \cdot \vec{c}_\perp)\end{aligned}$$

The decay length sum [2] can be directly measured using Eq. 5.8 and $\hat{\tau}^2 = 1$.

$$\begin{aligned}\chi^2 &= (\chi\vec{A}_c + \vec{D}_c) \cdot (\chi\vec{A}_c + \vec{D}_c) \\ &= \chi^2|\vec{A}_c|^2 + 2\chi\vec{A}_c \cdot \vec{D}_c + |\vec{D}_c|^2\end{aligned}$$

Therefore,

$$\chi = \frac{\vec{A}_c \cdot \vec{D}_c \pm \sqrt{|\vec{A}_c \cdot \vec{D}_c|^2 + (1 - |\vec{A}_c|^2)|\vec{D}_c|^2}}{1 - |\vec{A}_c|^2}$$

The vector $\vec{D}_c$ is always measurable since the geometrical space quantity $\delta\vec{c}_0$ relies on charged tracks. However, we can not use it to select a tau axis like the vector $\vec{D}_h$ because the scalar product $\vec{A}_c \cdot \vec{D}_c$ does not vanish, so the term $\hat{\tau} \cdot \vec{D}_c$ $(= \vec{A}_c \cdot \vec{D}_c + |\vec{D}_c|^2/\chi)$ can be either positive or negative, irrespective of χ sign.

The vector $\vec{A}_c$ is still in the $A_h - h_\perp$ plane. It is parallel to the intersection between the ambiguity plane and the plane defined by two charged track vectors $\vec{c}^\pm$ like in the case of $\vec{A}_h$. But the vector $\vec{A}_c$ has a different meaning compared with the interpretation of the vector $\vec{A}_h$. The projection of the vector $\vec{A}_c$ to the A_h axis makes $|\vec{A}_h|$. And $\vec{A}_c$ can be interior or exterior of the unit circle (Fig. 5.7, Fig. 5.8).

In the case $|\vec{A}_c| < 1$, *interior*, the sum decay lengths, χ_1 and χ_2, have opposite sign with each other and the tau axis selection using $\vec{D}_c$ can be applied (Fig. 5.7). When $|\vec{A}_c|$ is larger than one, *exterior*, the two tau solutions can not be separated since both solutions give χs of the same sign (Fig. 5.8).

Combining Eq. 5.6 and Eq. 5.8, we can derive the following vector relationship between $\vec{D}_h$ and $\vec{D}_c$:

$$\boxed{\vec{D}_h = \chi(\vec{A}_C - \vec{A}_h) + \vec{D}_c} \tag{5.9}$$

where all the vectors, $\vec{A}_C$, $\vec{A}_h$, and $\vec{D}_c$ are measurable.

[2] A similar calulation of the decay length sum in the general case was made by G. Giannini et al.[65].

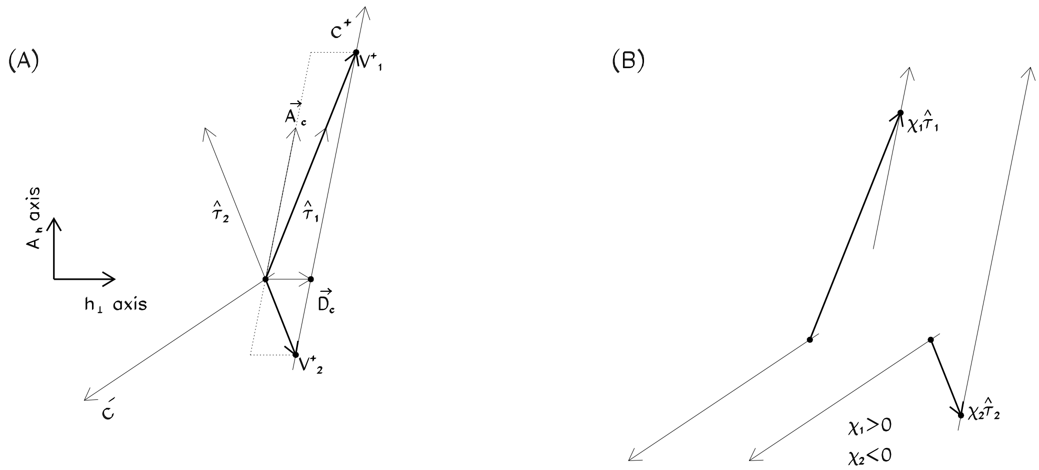

Figure 5.7: (A) Selectable configuration of $\vec{A}_c$ and $\vec{D}_c$. (B) Tau axis can be selected because only one solution, $\hat{\tau}_1$, gives a positive decay length.

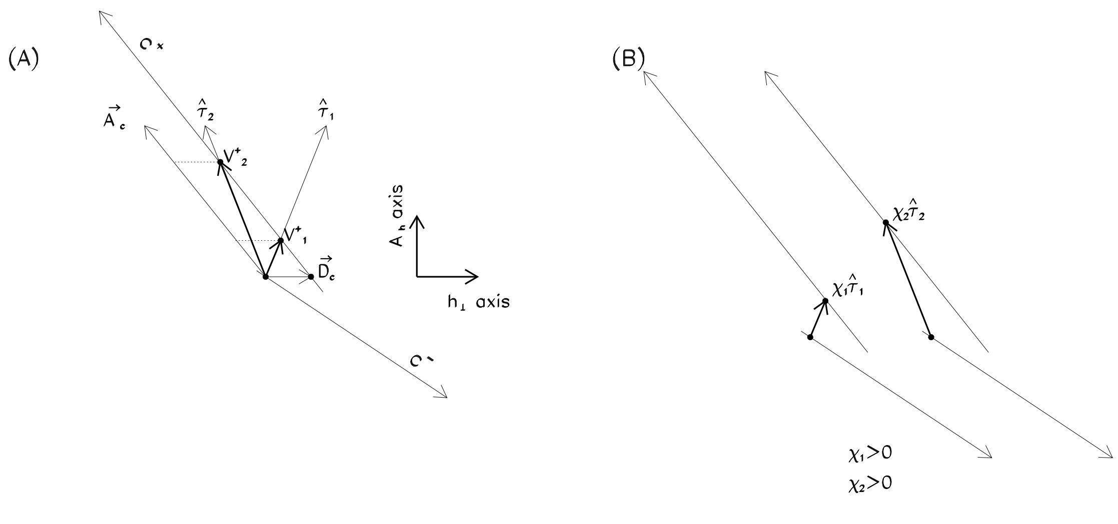

Figure 5.8: (A) Unselectable configuration of $\vec{A}_c$ and $\vec{D}_c$. (B) Tau axis can not be selected because both solutions give positive decay lengths.

Since χ is unknown, $\vec{D}_h$ is not measurable. However an approximate $\vec{D}_h$ can be found by using the expected decay length sum $\bar{\chi}$. The sum of the two decay lengths, χ, has a convoluted exponential distribution:

$$f(\chi) = \frac{\chi}{l_0^2} e^{-\chi/l_0}$$

where l_0 is the τ mean decay length. At LEP, the expected mean value $\bar{\chi}(= 2l_0)$ is about 4.6 mm. With this mean value $\bar{\chi}$, the $\vec{D}_h$ can be approximated to

$$\vec{D}_h \sim \bar{\chi}(\vec{A}_C - \vec{A}_h) + \vec{D}_c = 0.46(\vec{A}_C - \vec{A}_h) + \vec{D}_c \text{ (cm)}$$

Using this approximated $\vec{D}_h$ vector the good tau axis is selected with a lower efficiency than in the $\pi - \pi$ sample. Averaging over all hadronic decay channels, the *good tau axis* selection efficiency is about 69 %.

Usually the event thrust axis is used as an approximation to the tau direction. In the hadronic-hadronic decay events, the kinematical tau axis reconstruction allows an improvement of the tau direction resolution down to 16.5mrad without any selection, compared with $\sim$ 25mrad from the thrust axis.

Fig. 5.9 shows the angles between the selected tau axis and the MC true axis in all hadronic-hadronic tau decay events. We see that the tau direction resolution can be

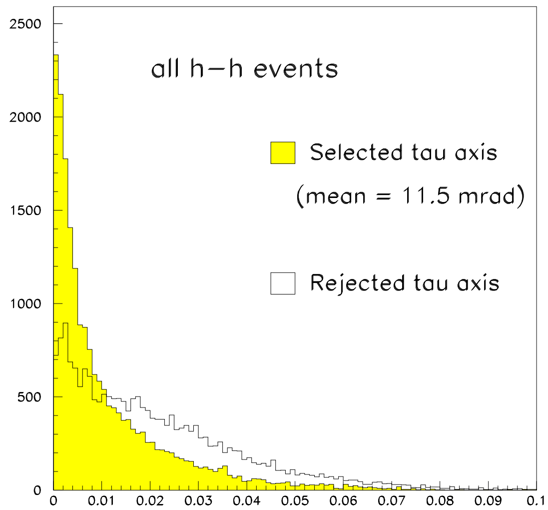

Figure 5.9: Angles between the selected tau axis and the MC true axis in all hadronic tau decay events

improved again by the selection using the approximated $\vec{D}_h$ vector, down to 11.5mrad.

Fig. 5.10 shows the χ distributions of the selected and rejected solutions using the approximated $\vec{D}_h$. The mean value of the selected χ distribution is found to be $\sim$

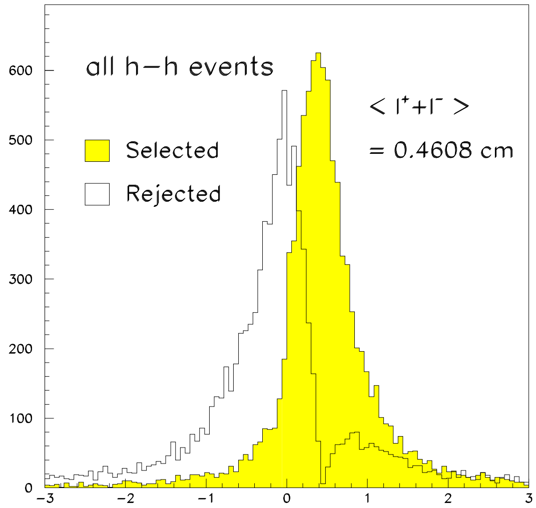

Figure 5.10: Decay length sum distributions from selected and rejected solutions. x-axis is in centimeter

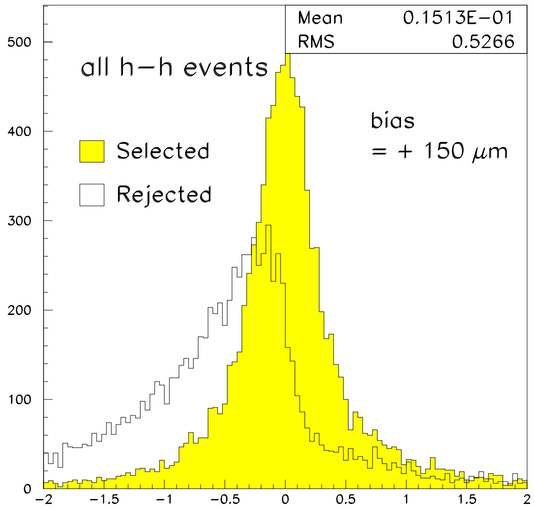

Figure 5.11: Resolution of the decay length sum reconstruction from the selected tau axis ($\chi^{reco} - \chi^{true}$). χ^{true} is Monte Carlo truth decay length sum.

4.6mm as expected. However the distribution has long tails which make large systematic uncertainty on the mean decay length measurement (Fig. 5.11).

5.5 Application of kinematics to lifetime measurement

As discussed in the previous section, the two-fold ambiguity of the tau axis reconstruction can not be fully resolved due to missing information (track parameters of the neutrals). However, the selection mechanism using the reconstructed or approximated vector $\vec{D}_h$ helps reducing the ambiguity, *i.e.* finding a more accurate tau direction than a random choice between the two solutions. Monte Carlo shows that the tau axis resolution is improved by 40 % (16.5mrad $\rightarrow$ 11.5mrad) when the selection mechanism is applied.

But the tau decay length (χ) solution from the selection does not allow to measure the lifetime since the remaining ambiguity makes a non-negligible bias on the decay length. To measure the lifetime, one should remove the two-fold ambiguity. A way to eliminate the ambiguity is introduced now using the projection in the $H - h_\perp - A_h$ coordinate system.

Consider the tau decay vector equation described by charged tracks (Eq. 5.7), $\chi\hat{\tau} = \delta\vec{c}_0 + \epsilon^+\hat{c}^+ - \epsilon^-\hat{c}^-$, and its projection onto the H axis, $h_\perp$ axis, and A_h axis. They are

$$\begin{aligned} \chi\hat{\tau}\cdot\hat{H} &= \delta\vec{c}_0\cdot\hat{H} + \epsilon^+\hat{c}^+\cdot\hat{H} - \epsilon^-\hat{c}^-\cdot\hat{H} && (5.10)\\ \chi\hat{\tau}\cdot\hat{h}_\perp &= \delta\vec{c}_0\cdot\hat{h}_\perp + \epsilon^+\hat{c}^+\cdot\hat{h}_\perp - \epsilon^-\hat{c}^-\cdot\hat{h}_\perp && (5.11)\\ \chi\hat{\tau}\cdot\hat{A}_h &= \delta\vec{c}_0\cdot\hat{A}_h + \epsilon^+\hat{c}^+\cdot\hat{A}_h - \epsilon^-\hat{c}^-\cdot\hat{A}_h && (5.12) \end{aligned}$$

As seen in the section 5.2, $\vec{A}_h$ is the inner bisector of $\hat{\tau}_1$ and $\hat{\tau}_2$. Defining θ as the angle between A_h and either tau axis, the above 3 projections can be written as

$$\begin{aligned} 0 &= \delta_H + \epsilon^+\alpha_H^+ - \epsilon^-\alpha_H^- && (5.13)\\ \pm\chi\sin\theta &= \delta_{h_\perp} + \epsilon^+\alpha_{h_\perp}^+ - \epsilon^-\alpha_{h_\perp}^- && (5.14)\\ \chi\cos\theta &= \delta_{A_h} + \epsilon^+\alpha_{A_h}^+ - \epsilon^-\alpha_{A_h}^- && (5.15) \end{aligned}$$

where δ_i is the projection of $\delta\vec{c}_0$ onto the i axis ($i = H, h_\perp, A_h$) and $\alpha_i^\pm$ are the cosine of the angle between the ($\pm$) charged track and the i axis.

The first and the third equations do not contain any ambiguity. They can be used in the lifetime measurement.

The 3rd projection will however give a poor estimation of the lifetime because of the small sizes of the measured quantities δ_{A_h} and $\pm\alpha^{\pm}_{A_h} - \cos\theta$ with respect to their errors. Fig. 5.12 shows the distributions of δ_i and $\alpha^{\pm}_i$. The average values are to be compared to the tracking error affecting the δ's ($\sim 50\mu$m) and the angular error affecting the $\alpha^{\pm}$'s ($\sim$ 1mrad).

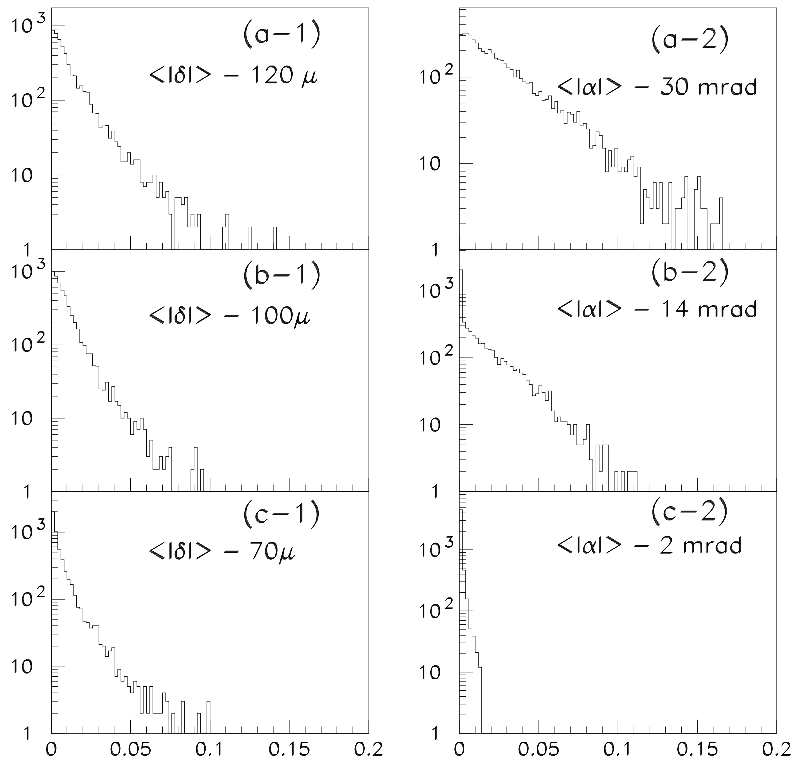

Figure 5.12: (a-1,2) δ_H, α_H, (b-1,2) $\delta_{h_\perp}$, $\alpha_{h_\perp}$, (c-1,2) δ_{A_h}, $\alpha_{A_h} - \cos\theta$

The 3DIP method is an application of the first equation. We will discuss the 3DIP method in the next chapter.

Part III

MEASUREMENT OF TAU LIFETIME USING 3DIP METHOD

Chapter 6

3-D Impact Parameter Method

Kinematics and geometry in the hadronic-hadronic $\tau^+\tau^-$ decay events give a possible way to measure the tau direction and the tau decay length. Especially the projection onto the vector $\vec{H}$ allows an equation which is free from the two-fold ambiguity of tau direction. We then need to know how well the vector $\vec{H}$ can be reconstructed, and how to extract the lifetime from the equation.

In this chapter, we will discuss quantitatively the characteristics of physical observables, δ_H and $\alpha_H^{\pm}$, and introduce the likelihood method to extract the tau lifetime.

6.1 Perpendicular axis

As seen in the previous chapter, once we have the tau decay angles ($\psi^{\pm}$) from the decays of τ^+ and τ^- in the hadronic-hadronic decay events, it is possible to determine the special vector, $\vec{H}$, orthogonal to τ direction, deduced only from kinematics and the reconstructed hadrons ($h^{\pm}$):

$$\vec{H} = \hat{h}^+ \cos\psi^- + \hat{h}^- \cos\psi^+$$

Hereafter, $\hat{H}$ will be called the perpendicular axis or simply H-axis.

Let us recall the tau decay vector equation, $\chi\hat{\tau} = \delta\vec{c}_0 + \epsilon^+\hat{c}^+ - \epsilon^-\hat{c}^-$ which gives

Eq. 5.13 when projected onto $\hat{H}$:

$$0 = \delta_H + \epsilon^+ \alpha_H^+ - \epsilon^- \alpha_H^-$$

where $\delta_H \equiv \delta \vec{c}_0 \cdot \hat{H}$ and $\alpha_H^{\pm} \equiv \hat{c}^{\pm} \cdot \hat{H}$ are three measurable quantities. For simplicity, let us omit the subscript H and redefine $\alpha^+ \equiv \alpha_H^+$, $\alpha^- \equiv -\alpha_H^-$, and $\delta \equiv -\delta_H$. We have

$$\delta = \epsilon^+ \alpha^+ + \epsilon^- \alpha^- \tag{6.1}$$

where $\epsilon^{\pm}$ are unknown.

Fig. 6.1 illustrates the physical quantities used in 3DIP method. The plane normal

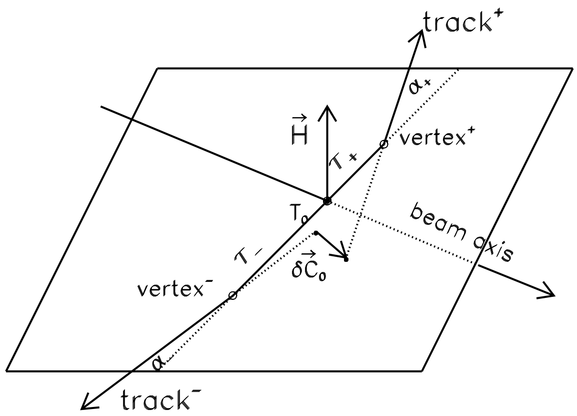

Figure 6.1: Schematic view of 3DIP method

to $\hat{H}$ contains the $\tau^{\pm}$ vectors. Because of the small decay angles, $\alpha^{\pm}(\equiv \hat{c}^{\pm} \cdot \hat{H})$ is almost equal to the angles of the tracks with the plane. $\hat{H}$ axis is random with respect to the beam axis.

Eq. 6.1 is not always realized in real experiments, because the term $\hat{\tau} \cdot \hat{H}$ is not zero when τ^+ and τ^- are not back-to-back, or if $\hat{H}$ is badly reconstructed by loss of some photons, etc.. Fig. 6.2 shows the perpendicularity defined as $\cos^{-1}(\hat{\tau} \cdot \hat{H}) - \pi/2$. The line is fitted by three gaussians in order to estimate the resolution of the perpendicular axis. The width of the central peak (the first gaussian) is 1mrad and the second is $\sim$ 6mrad.

The non-zero term, $(l^+ + l^-)\hat{\tau} \cdot \hat{H}$, introduces about 4.6μ smearing of δ in Eq. 6.1 when assuming a mean decay length $2.3mm$ ($\sim 27\mu$ smearing for the second gaussian). Events

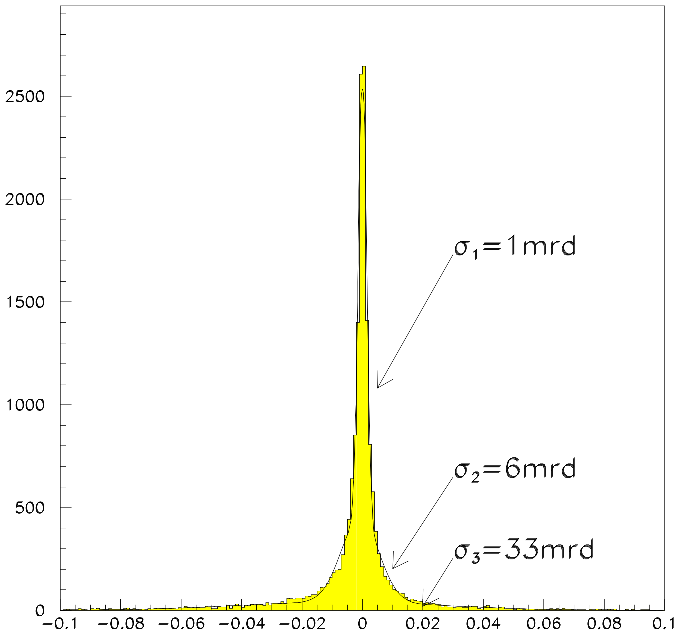

Figure 6.2: Perpendicularity between the vector $\hat{H}$ and $\hat{\tau}$ using MC. $\hat{H}$ is reconstructed using full detector informations. $\hat{\tau}$ is the MC generated tau direction vector.

having bad perpendicularity (events in the third gaussian contribution, $\sigma_3 \sim$ 33mrad) have worse resolution than that of thrust axis and may yield a large smearing. The cut of badly measured H-axis and systematic effects induced by this term will be discussed in Sec. 7.3 and 8.2.1.

6.2 Generalized IPS equation in 3-dimensional space

It can be seen that the unknown $\epsilon^{\pm}$ are nearly equal to the decay length $l^{\pm}$ when $\vec{c}_0^{\pm}$ are chosen as the points of minimum approach of the charged track to the beam. This is due to two reasons: *i*) the tau decay angle ψ is small ($\leq$ 150mrad) even if the momentum of the hadron is as low as 2 GeV. *ii*) the polar angles of both charged tracks are greater than $\sim 50°$ and less than $\sim 130°$ when restricted within the VDET acceptance. Fig. 6.3 shows the distributions of ϵ and l in MC.

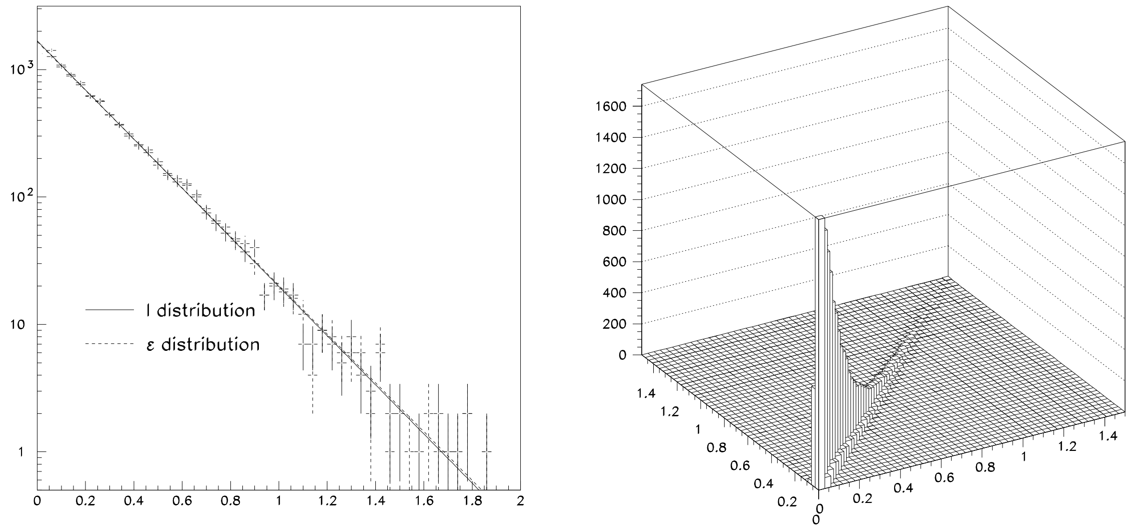

Figure 6.3: (*left*) distributions of ϵ and l in MC, (*right*) scatter plot of ϵ and l

Eq. 6.1 can then be rewritten as:

$$\boxed{\delta = l^+\alpha^+ + l^-\alpha^-} \tag{6.2}$$

This equation is the basis of the 3DIP method for the tau lifetime measurement. It is formally identical to the IPS equation.

To illustrate the relation with IPS, the term δ can be expanded as follows,

$$\begin{aligned}
\delta &\equiv \delta\vec{C}_0 \cdot \hat{H} \\
&= (d_0^+ \sin\phi^+ - d_0^- \sin\phi^-)H_x - (d_0^+ \cos\phi^+ + d_0^- \cos\phi^-)H_y + (z_0^+ - z_0^-)H_z \\
&\sim (d_0^+ + d_0^-)(H_x \sin\bar{\phi} - H_y \cos\bar{\phi}) + (z_0^+ - z_0^-)H_z
\end{aligned}$$

where $\phi^+ \sim \phi^- + \pi$ and $\bar{\phi} \equiv (\phi^+ + \phi^- \pm \pi)/2$. Therefore δ can be regarded as the combined quantity of IPS and z_0 difference in space. An analysis analog to IPS method can be done with the following favorable conditions:

- δ is given from d_0 and z_0 informations, and is typically larger than IPS, $\delta \sim 130\mu m$. σ_δ is dominated by tracking error. σ_δ/δ is thus reduced compared with IPS.
- as it will be shown in the following section the uncertainties of the angles $\alpha^\pm$ are negligible (coming only from tracking, $\sim 0.5mrd$). The method thus does not suffer

from angular uncertainties and does not need to use a numerical integration over the measured angles (h function in IPS method [53]).

- the beam size contributions to σ_δ is very small ($\sim 4\mu$) as in IPS compared with the tracking error ($\sim 50\mu$) since the large uncertainty of the z component ($\sigma_z \sim .7cm$) cancels out in $(z_0^+ - z_0^-)$.
- the method is applicable to 3 prong tau decay as well as 1 prong after reconstruction of the sum track (App. C).

6.2.1 δ resolution and error estimation

Apart from tracking, the experimental error on the 3-D impact parameter comes from various sources: a small smearing from the beam size, badly reconstructed $\hat{H}$, $\tau^+\tau^-$ acollinearity, etc.. The measurable errors are

- Tracking : $\sigma_\delta^{tracking} = \vec{\sigma}(\delta\vec{C}_0) \cdot \hat{H}$; typically $\sim 50\mu m$ for 1-1, $\sim 40\mu m$ for 1-3 sample.
- Beam size and beam position measurement : typically $\sim 4\mu m$

The contributions to $\sigma(\delta\vec{C}_0)$ from the beam size and position measurement error are given in App. D. It is to be noticed that the z-component contribution to σ_δ from the beam size is also parameterized by σ_x^{BP} and σ_y^{BP}; the beam spread along the z-axis does not affect the $\delta\vec{C}_0$ measurement.

The measured δ and the true δ^{tru} ($\equiv -\delta\vec{C}_0^{tru} \cdot \hat{H}^{rec} + (l^+ + l^-)\hat{\tau}^{tru} \cdot \hat{H}^{rec}$) quantities are compared to see how well the errors are estimated (Fig. 6.4). The resolution distribution, $(\delta^{tru} - \delta^{rec})/\sigma_\delta$, is nearly gaussian except for long tails. The sigma fitted in Fig. 6.4 larger than the expected value 1.0, means that the measured errors are under-estimated by about 24% in 1-1 and $\sim$ 26 % in 1-3. The tracking error from JULIA, $\sigma_\delta^{tracking}$, affecting δ through $\delta\vec{C}_0$ is found to be $\sim$ 9 % under-estimated in 1-1 and $\sim$ 13 % in 1-3 MC samples. Using MC true tau directions and decay lengths, we estimate that the smearing from the badly measured H-axis, $(l^+ + l^-)\hat{H} \cdot \hat{\tau}$, is about 12% of $\sigma_\delta^{tracking}$.

The parametrisations of the various kinds of uncertainties are not simple. The sum of d_0's of the $Z^0 \to \mu\mu$ and $\gamma\gamma \to \mu\mu$ can be used to monitor the tracking resolution in the

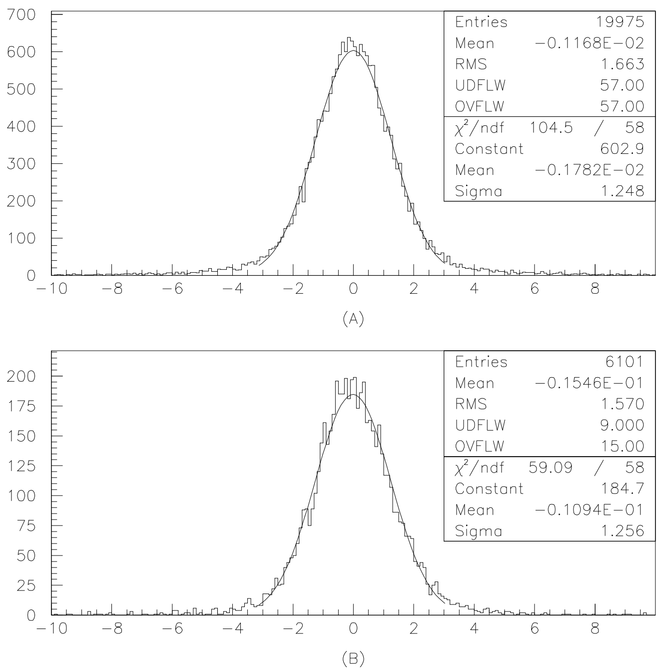

Figure 6.4: Resolution of δ, $(\delta^{tru} - \delta^{rec})/\sigma_\delta$ distribution of (A) 1-1 sample (B) 1-3 sample

high momentum regions and the low momentum regions, respectively. However instead of using these external samples to parameterize σ_δ, we choose to fit the resolution scale factor, κ, together with the decay length:

$$\sigma^{Experiment} = \kappa\sigma_\delta^{tracking} \oplus \sigma_\delta^{BP}$$

in order to reproduce the real experimental error. This cannot be done in the IPS method because the resolution fit and the decay length fit are correlated with each other due to the relative sizes of IPS and errors, and the large error on ψ_{xy}. In the 3DIP method the angles $\alpha^\pm$ are measured very precisely (0.5 mrad, Fig. 6.5), so that the fit of the resolution and the fit of the decay length are decoupled. This point will be addressed again in Sec. 8.3

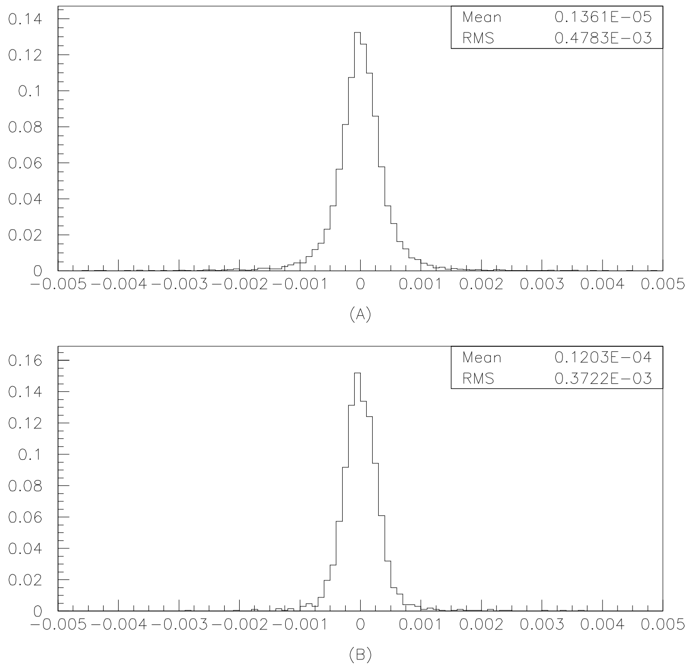

Figure 6.5: $\alpha^{rec} - \alpha^{tru}$ distribution from (A) 1-prong charged tracks (B) sum tracks of 3-prong decays

6.3 Likelihood Approach

6.3.1 Gaussian convoluted double-exponential likelihood function

Assume the lifetime is τ_0 and the number of events is N_0. After t seconds, the number of taus left is, $N(t) = N_0 e^{-\frac{t}{\tau_0}}$. When τ's are monoenergetic, this can be written as the function of the decay length, $N(l) = N_0 e^{-\frac{l}{l_0}}$, where $l_0 = \gamma\beta c\tau_0$.

The true $\delta_i (\equiv (\vec{c}_0 - \vec{\tau}_0) \cdot \hat{H})$ from a hemisphere is related to the decay length l and the decay angle α by $\delta'_i = l\alpha'_i$ where $i = \pm$. Here, we denote the primed quantities as the true ones. The normalized true δ'_i distribution for a given l_0 is

$$F'(\delta'_i, \alpha'_i) = \frac{1}{l_0 \alpha'_i} e^{\frac{-\delta'}{l_0 \alpha'_i}}$$

Ignoring the measurement errors, the expected δ distribution is a double exponential distribution from two tau decays. Considering the two hemispheres together, we redefine λ_+ as the greater one between $l_0\alpha^+$ and $l_0\alpha^-$ and λ_- as the smaller one. Then the convoluted distribution of sum of the impact parameters from the two hemispheres gives:

$$F'(\delta', \alpha^+, \alpha^-) = \int_0^\infty \frac{1}{l_0\alpha'_+} e^{\frac{-\delta'}{l_0\alpha'_+}} \frac{1}{l_0\alpha'_-} e^{\frac{-\delta'}{l_0\alpha'_-}} \delta(\delta' - \delta_+ - \delta_-) d\delta_+ d\delta_-$$

$$\begin{array}{lll} F'(\delta', \alpha^+, \alpha^-) = & \frac{1}{\lambda_+ - \lambda_-}(e^{\frac{-\delta'}{\lambda^+}} - e^{\frac{-\delta'}{\lambda^-}}) & \text{when } \lambda_+\lambda_- > 0, \\ F'(\delta', \alpha^+, \alpha^-) = & \frac{1}{\lambda_+ - \lambda_-} e^{\frac{-\delta'}{\lambda^+}} & \text{when } \lambda_+\lambda_- < 0 \text{ and } \delta' > 0, \\ F'(\delta', \alpha^+, \alpha^-) = & \frac{1}{\lambda_+ - \lambda_-} e^{\frac{-\delta'}{\lambda^-}} & \text{when } \lambda_+\lambda_- < 0 \text{ and } \delta' < 0, \end{array}$$

The real distribution is the above distribution convoluted with the experimental resolution function, $g(\delta, \alpha^+, \alpha^-)$

$$F(\delta, \alpha^+, \alpha^-, \sigma) = \int\int\int g(\delta', \alpha'^+, \alpha'^-) F'(\delta', \alpha^+, \alpha^-) d\delta' d\alpha'^+ d\alpha'^-$$

The resolution function of δ (Fig. 6.4) is well approximated by a gaussian up to 3σ. The errors on $\alpha^\pm$ coming only from tracking are small enough to be neglected ($\sim 0.5mrd$)(Fig. 6.5). g is then a simple gaussian with width σ_δ. The possible effects due to non-gaussian tails will be studied in Chap. 8.

We get the likelihood function for a given l_0 as follows by integration:

$$\mathcal{F}(\delta, \alpha^+, \alpha^-, \sigma; l_0) = \frac{1}{2l_0(\alpha_+ - \alpha_-)} e^{-\frac{\delta^2}{2\sigma^2}} (s_+ e^{Q_+^2} \mathrm{erfc}(Q_+) - s_- e^{Q_-^2} \mathrm{erfc}(Q_-)) \tag{6.3}$$

where $s_\pm$ are the signs of $\alpha^\pm$ and $Q_\pm = \frac{s_\pm}{\sqrt{2}}(\frac{\sigma}{l_0\alpha_\pm} - \frac{\delta}{\sigma})$. erfc is the complementary error function defined as

$$\mathrm{erfc}(x) = 1 - \mathrm{erf}(x) = \frac{2}{\sqrt{\pi}} \int_x^\infty e^{-x^2} dx$$

Chapter 7

Event Selection

In the 1992 ALEPH Data, 27,118 $Z^0 \to \tau^+\tau^-$ events were selected by TSLT02. 157,987 events were selected in 200,000 Monte Carlo generated by KORL06 using 1992 geometry. We checked all detector status (Trigger, VDET, ITC, TPC, ECAL, HCAL) and rejected events when any of these status is not O.K..

7.1 Preliminary selection

The analysis package (TOPCLAS [44]) for the tau branching ratio studies is used to select the hadronic-hadronic $\tau^+\tau^-$ decay events and to improve the hadron reconstruction; namely it is used to

- reject the non-tau backgrounds left after TSLT02,
- identify the hadronic channels,
- treat the gamma conversions,
- avoid summing radiative or fake photons to hadron reconstruction,
- improve the reconstruction of π^0 momenta.

Events having HCAL photons are excluded to ensure good π^0 momentum measurement and the hadron mass is restricted to be less than $2GeV/c^2$. To protect from interactions with detector materials, events with additional bad tracks [1] are rejected and we require that the total charge of each hemisphere is ± 1 and opposite to each other. We do not consider the decays with more than 3 prongs.

Data Samples MC Generator	92 Real	92 MC KORL06
Number of Events		200,000
TSLT02	27118	157987 (79.0%)
Detector status	25712 (94.8%)	157987 (100.%)
Background Rejection	25089 (97.6%)	157766 (99.9%)
Hadron mass cut	24150 (96.3%)	152907 (96.9%)
No additional bad track	21674 (89.7%)	136168 (89.1%)
Sum of charge = ± 1	21216 (97.9%)	133844 (98.3%)
No more than 3-prong	21186 (99.9%)	133626 (99.8%)
GET_BP	20892 (98.6%)	133626 (100.%)
Had-Had decay	8160 (39.1%)	49757 (37.2%)
Basic track qualities	6115 (74.9%)	38115 (76.6%)

Table 7.1: Data reductions after preliminary cuts

We further demand that both hemispheres have at least one track satisfying the following track qualities:

- $p > 2$ GeV/c, $|d_0| < 1.0$ cm, $|z_0| < 5.0$ cm
- $\chi^2/NumDF$ of the helix fit less than 4.0
- at least 8 TPC hits and 2 ITC hits
- at least 1 $r-\phi$ hit and 1 $r-z$ hit at the same time in VDET inner or outer layers.

We will call LCT (Leading Charged Track) a track which fulfills the above conditions. Note that we do not use the track having only $r-\phi$ or $r-z$ VDET hits. A track with $r-\phi$ and $r-z$ hits but in different VDET layers is not used either. When there exist more than one LCT in 3 prong case, we define the most energetic track among them as LCT. For real data, we restrict to events with GET_BP information [69].

[1] 4 TPC hits, $|d_0| < 40$cm but not a good track ($|d_0| < 2$cm, $|z_0| < 10$cm, $p > 0.5$GeV/c, 4 TPC hits)

Tab. 7.1 shows the data reductions after the above cuts.

We analyse separately the 1-1 and 1-3 samples. We ignore the 3-3 sample. Tab. 7.2 shows the data samples.

Data Samples	92 Real	92 MC
1 - 1	3745 (61.2%)	23133 (60.7%)
1 - 3	2103 (34.4%)	13245 (34.8%)
3 - 3	267 (4.4%)	1737 (4.5%)
Total	6115 (100.%)	38115 (100.%)

Table 7.2: Number of event in each sample

7.2 Additional cuts : VDET pattern and vertex χ^2 probability

While the quantities $\vec{c}_0$ and $\hat{c}$ are directly the point of minimum approach to the beam axis and the direction of the charged track in 1-prong decay, they must be computed from the sum track in case of 3-prong tau decay. The sum track helix and its error components are obtained from the fitted vertex, the momenta sum, and their corresponding covariant matrices by using of YTOP package (App. C).

Mismatch between the VDET hits and the track extrapolation from TPC/ITC may lead to large shift on δ while the measurement error σ_δ stays small. This problem happens frequently in 3-prong decays because of the overlapping of the track extrapolations due to the small opening angle. It also happens in 1-prong decays when there exist additional tracks, e.g. tracks from photon pair conversions.

The problem is largely reduced when we do not allow the sharing of VDET hits with another track. Additional track requirements are applied to prevent VDET pattern problems:

- VDET hits ($r-\phi$ and $r-z$) of LCT must not be shared with another track.

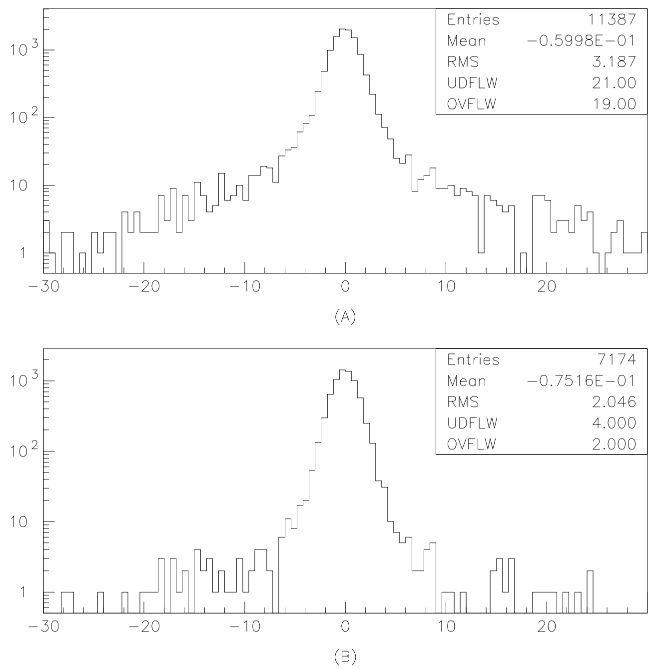

Figure 7.1: (A) $(d_0^{rec} - d_0^{tru})/\sigma_{d_0}$ of the sum track (3-prong) before applying the VDET pattern cut (B) after the cut.

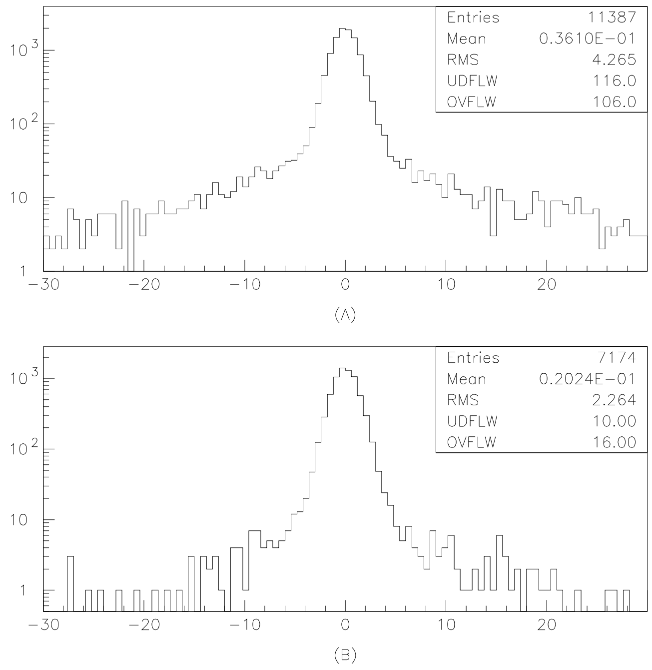

Figure 7.2: (A) $(z_0^{rec} - z_0^{tru})/\sigma_{z_0}$ of the sum track (3-prong) before applying the VDET pattern cut (B) after the cut.

- In case of 3-prong, both non LCT tracks must have at least one VDET hit (again $r-\phi$ and $r-z$ at the same plane) ; these VDET hits are not shared with that of LCT. [2]

Fig. 7.1 and Fig. 7.2 show the d_0 and z_0 resolutions of the sum track in 3-prong decay before and after the above cuts.

For 3-prong decays, a cut on the probability of the secondary vertex in the sum track reconstruction is applied, requiring that $P(\chi^2_{vertex})$ is greater than 0.1 %. Fig. 7.3 and Fig. 7.4 shows the chi square distribution of vertex and the corresponding probability plot.

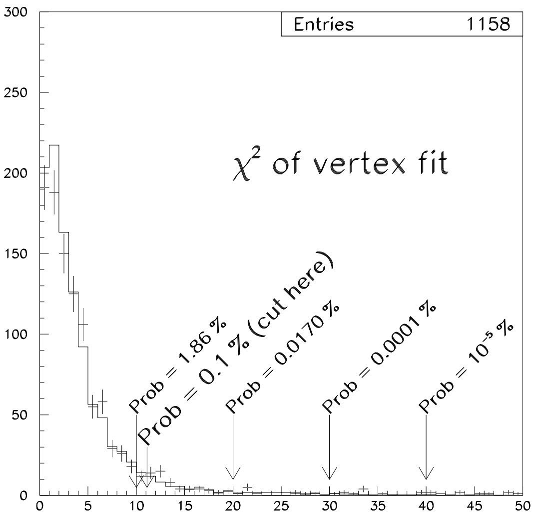

Figure 7.3: χ^2 of vertex fit in 3-prong decay (error bar: data, histogram: MC)

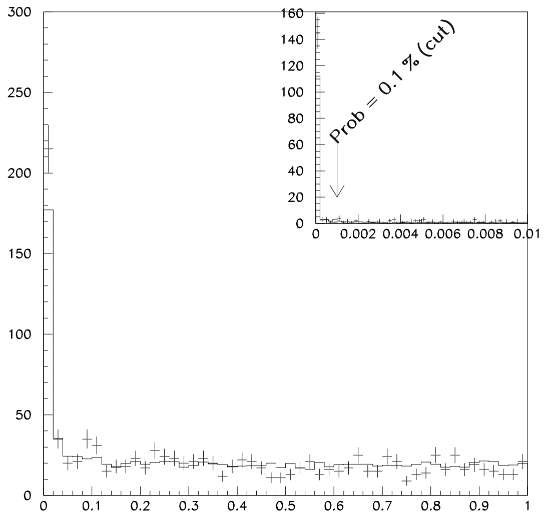

Figure 7.4: Probability of vertex fit

[2]non LCT tracks have less strict conditions; $p > 0.5GeV/c$, $|d_0| < 1.0cm$, $|z_0| < 5.0cm$ and $\chi^2/NumDF < 4.0$, at least 8 TPC hit.

7.3 Additional cut : Badly measured H-axis

As already stressed in Chap. 6, Eq. 6.1 is not exact when the H-axis is not perpendicular to tau. To keep the neglected term, $(l^+ + l^-)\hat{\tau} \cdot \hat{H}$, small we need therefore to cut off the events with badly measured H-axis. The tails ($>$ 20mrad) in the perpendicularity plot (Fig. 6.2) amount to 14 %, 40 % of them originating from hard non-collinear $\tau^+\tau^-$ events [3].

Considering first that the thrust axis is an approximation of tau axis with a 30mrad resolution in space, we calculate the perpendicularity between $\hat{H}$ and the thrust axis and cut at 30mrad. [4] About 10 % of events are removed in 1-1 and 1-3 samples. The cut reduces the tails to 7 %, half of them come from hard non-collinear $\tau\tau$ events.

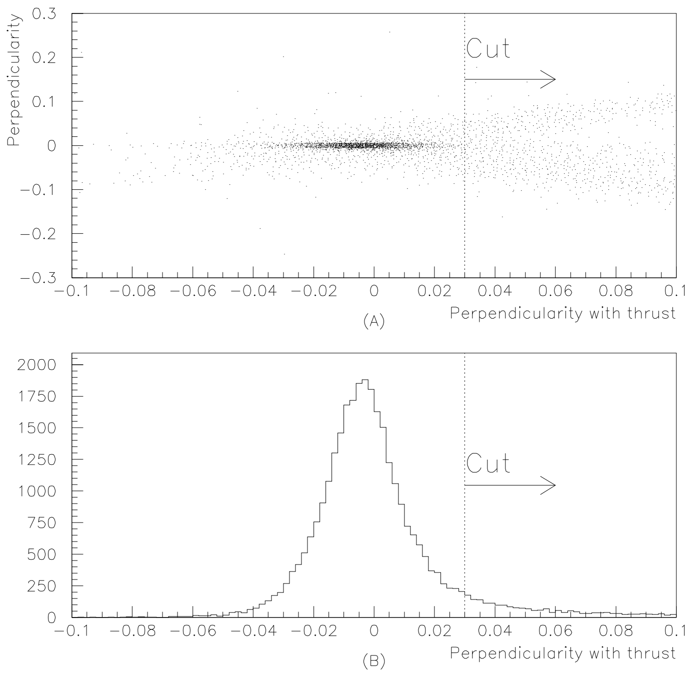

Figure 7.5: (A) perpendicularity between H and thrust versus true perpendicularity (B) perpendicularity between H and thrust

To further reduce the tails, we use the kinematical properties of the H-axis. The cut is based on the fact that the same physical quantities and hypotheses are used in the H-axis

[3] A hard non-collinear $\tau^+\tau^-$ is defined as $\theta^{acol}_{\tau\tau} > 10$mrad.

[4] Thrust axis is reconstructed by all energy flow objects.

measurement and in the kinematical τ axis reconstruction. To understand this, let us return to the kinematical tau direction reconstruction. In each hemisphere, kinematics of the tau decay constrain the unknown tau axis to be on a cone around the reconstructed hadron direction, $\hat{h}$, with the opening angle $\cos\psi$ (Eq. 5.1). As developped in Chap. 5, the hypothesis that the two taus are back-to-back reduces the common tau direction to the two intersections between the cones. But when the hadron is badly reconstructed due to missing photons or undetectable neutral hadrons, e.g. K_L^0, or when the two taus are not back-to-back, it may happen that the cones do not have any intersection.

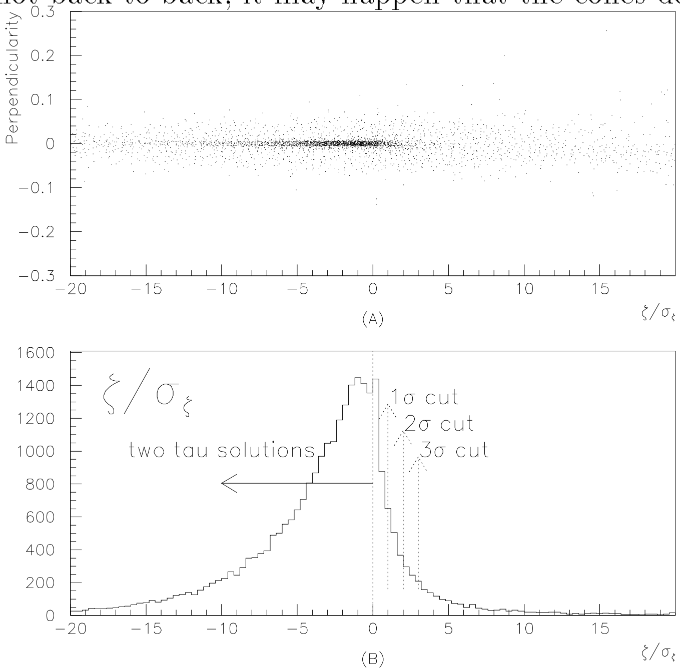

Figure 7.6: (A) ζ/σ_ζ vs Perpendicularity (B) ζ/σ_ζ

Because of their common physics inputs, there is a strong correlation between the perpendicularity of the vector $\hat{H}$ and the kinematical tau solutions. When the cones do not intersect, this means that the taus are not back-to-back or the energy of hadron is badly estimated due to missing neutrals, etc.. This also results in $\hat{H}$ being badly reconstructed. Thus we can control the perpendicularity of H-axis by checking the existence of kinematical tau solutions.

The angular distance, denoted by ζ, between the cones is obtained from the angle ξ between two hadron directions, and the decay angles, ψ^+ and ψ^-:

$$\zeta = 2MAX(\xi, \psi^+, \psi^-) - (\xi + \psi^+ + \psi^-)$$

Notice that when ζ is negative there are two kinematical tau directions, and when ζ is positive the two cones do not intersect.

Fig. 7.6 shows the dependence of the perpendicularity on ζ.

We compute the error on ζ, σ_ζ, assuming $\sigma_\zeta = \sigma_\xi \oplus \sigma_{\psi^+} \oplus \sigma_{\psi^-}$ (App. F).

More than 20 % of the data samples would be rejected if we restrict to events with a tau axis solution. To save statistics, we may accept also the events if the angular distance between the two cones is comparable with its variance σ_ζ, i.e., when they can intersect within their errors in opening angle and directions. We exclude the events with $\zeta > 3\sigma_\zeta$, which are suspected as having badly reconstructed H-axis.

Fig. 7.7 (A) shows the perpendicularity in logarithmic scale. The hatched histograms are the rejected events by $\zeta > 3\sigma_\zeta$ cut.

After the ζ/σ_ζ cut, the tails amount to ~ 5 %. Since the kinematical cut is sensitive to the geometrical configuration of the cones, the ζ/σ_ζ cut is efficient to reject the non-collinear $\tau\tau$ events. The latter now amounts only 20 % of the remaining tails. The final H-axis perpendicularity is within 9mrad.

7.4 Other additional cuts

We exclude the events having an abnormally large $|\delta\vec{C}_0|$ and $|\alpha^+ + \alpha^-|$ which cannot happen in normal two tau decays. We cut off the events when $|\delta\vec{C}_0| > 2mm$ or $|\alpha^+ + \alpha^-| > 0.2$. In real data only 3 and 5 events are rejected respectively by these cuts in 1-1 sample; all 1-3 events pass the cuts.

To fit the lifetime we consider only the events with a large enough likelihood, $\mathcal{F}(l_0, \kappa_0)$. $\mathcal{F}(l_0, \kappa_0)$ is computed with l_0 set to MC input decay length ($l_0 = 0.2279$cm) and κ set to the value κ_0 deduced from maximum likelihood fit without cut. The applied cut is

$$\log(P(\mathcal{F})) > -3$$

This $P(\mathcal{F})$ can be interpreted as a likelihood probability (App. G.2). The cut value $P(\mathcal{F}) > 10^{-3}$ is consistent with our data statistics of few thousand events (Fig. 7.8 and Fig. 7.9).

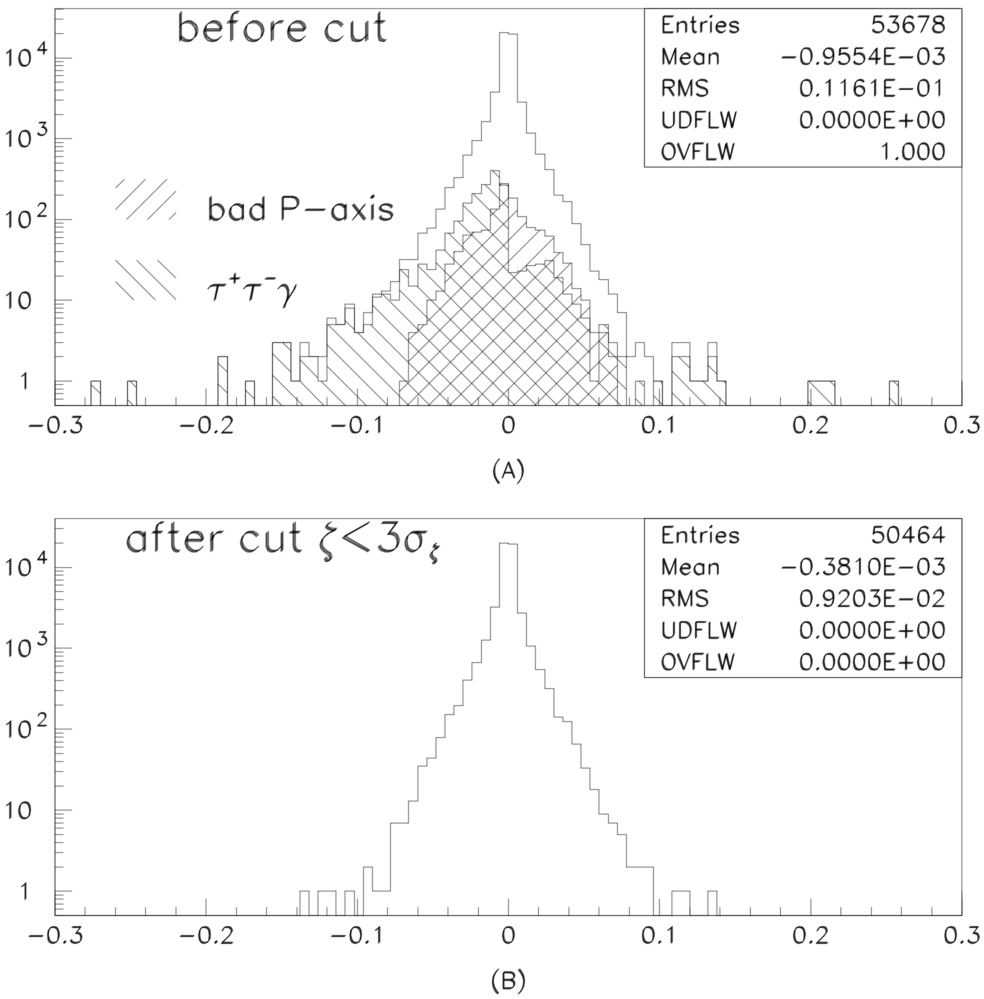

Figure 7.7: Perpendicularity (A) before applying ζ/σ_ζ cut. Superimposed histograms are the events containing badly measured H-axis (left hatched) and hard non-collinear $\tau^+\tau^-$ pair (right hatched) rejected by the ζ/σ_ζ cut. (B) after the cut

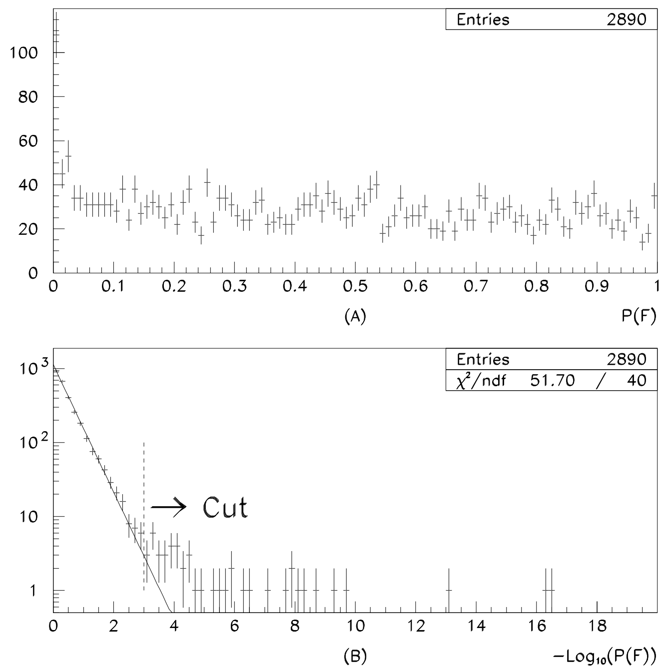

Figure 7.8: (A) Distribution of $P(\mathcal{F})$ (B) $-\log P(\mathcal{F})$ in 1-1 data

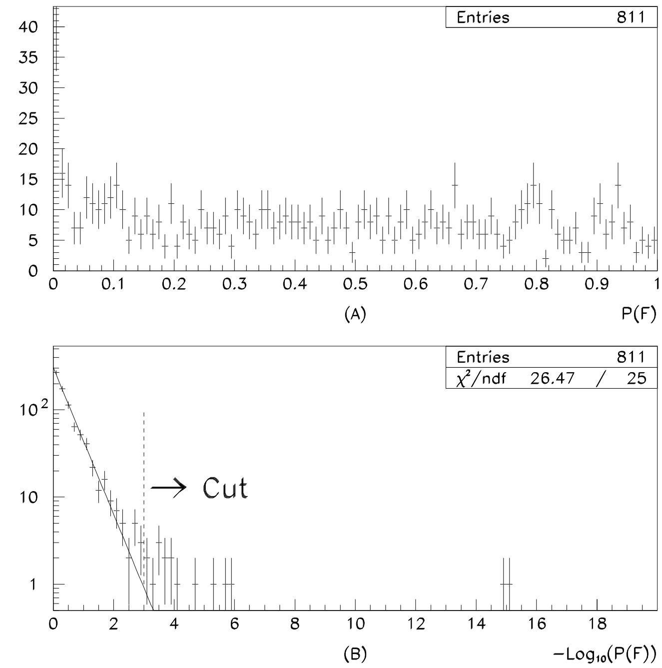

Figure 7.9: (A) Distribution of $P(\mathcal{F})$ (B) $-\log P(\mathcal{F})$ in 1-3 data

7.5 Summary of cuts

Tab. 7.3 shows the number of events in each sample after the above cuts. We will discuss

Data Samples	1 - 1		1 - 3	
Data	Data	MC	Data	MC
Number of events	3745	23133	2103	13245
VDET pattern	3432 (91.6%)	22612 (97.7%)	1158 (55.1%)	8096 (61.1%)
$Prob(\chi^2_{vertex})$	-	-	993 (85.8%)	7162 (88.5%)
Cut on $\hat{H} \cdot Thrust$	3080 (89.7%)	20310 (89.8%)	899 (90.5%)	6529 (91.2%)
$\zeta < 3\sigma_\zeta$	2898 (94.1%)	19263 (94.8%)	811 (90.2%)	5969 (91.4%)
$\delta C_0 < 2mm$	2895 (99.9%)	19222 (99.8%)	811 (100.%)	5962 (99.9%)
$\lvert\alpha^+ + \alpha^-\rvert < 0.2$	2890 (99.8%)	19201 (99.9%)	811 (100.%)	5962 (100.%)
$\log(P(\mathcal{F})) > -3$	2840 (98.3%)	18968 (98.8%)	794 (97.9%)	5888 (98.8%)

Table 7.3: Number of events in each sample after the additional cuts

the systematics related to these cuts in Sec. 8.2.

For sake of comparison with IPS results [53] the δ distributions from 1-1 sample and 1-3 sample are shown in Fig. 7.10 for different ranges of $\alpha^+ + \alpha^-$. For large $|\alpha^+ + \alpha^-|$, clear exponential decreases are observed. Resolution effects are seen around $\delta = 0$.

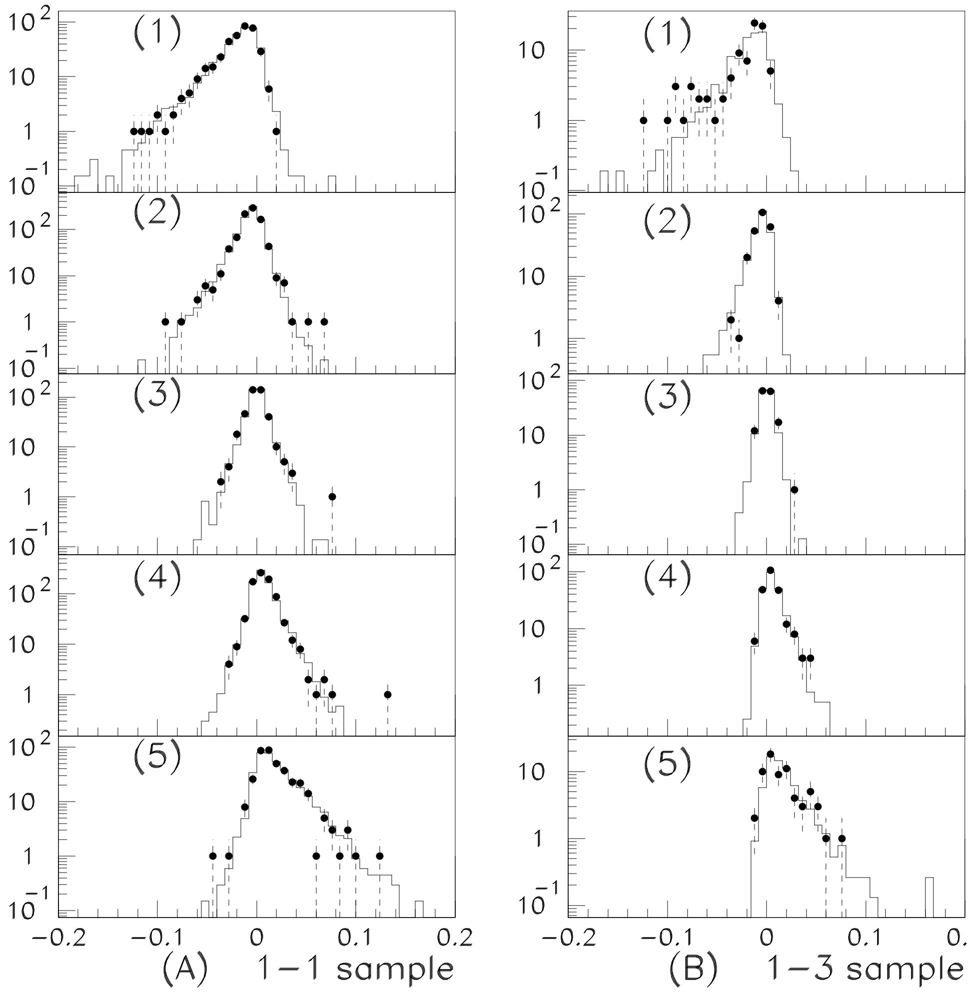

Figure 7.10: (A) δ distribution for various ranges of $\alpha^+ + \alpha^-$ of 1-1 sample; (1) $\alpha^+ + \alpha^- < -0.06$, (2) $-0.06 < \alpha^+ + \alpha^- < -0.01$, (3) $-0.01 < \alpha^+ + \alpha^- < 0.01$, (4) $0.01 < \alpha^+ + \alpha^- < 0.06$, (5) $\alpha^+ + \alpha^- > 0.06$. (B) the same of 1-3 sample. The points are the data and the lines are MC.

Chapter 8

Results and Systematics

8.1 Result of the likelihood fit

8.1.1 1-1 sample

Fig. 8.1 shows the 1σ and 2σ contours of λ_{fit} [1] and κ_{fit}. It appears that λ fit and κ fit

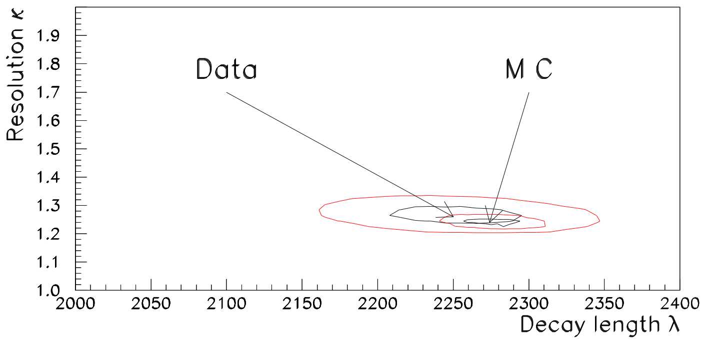

Figure 8.1: λ-κ fit contour for 1-1 sample : inner contour shows 1σ variation and outer is 2σ.

are uncorrelated. This question will be addressed in details in Sec. 8.3.

[1] We denote the fitted decay length λ to distinguish from MC input decay length l_0

The fitted decay length and the factor κ from the 1-1 sample are summarized in Tab. 8.1. The fitted κ is consistent with the resolution distribution in MC (Fig. 6.4).

1-1 sample	Real Data	Monte Carlo
λ (cm)	0.2250 ± 0.0045	0.2274 ± 0.0017
κ	1.26 ± 0.03	1.24 ± 0.01

Table 8.1: The fitted decay length and error factor from the 1-1 sample

The Monte Carlo was generated with a mean lifetime, 296×10^{-15} sec, at a center of mass energy of 91.25 GeV. Ignoring radiative corrections, this value corresponds to a mean decay length of 0.2279 cm. The fitted decay length of MC agrees well with the generated one.

The ratio between Data and MC

$$\frac{\lambda_{data}}{\lambda_{MC}} = 0.989$$

corresponds to a lifetime $292.9 \pm 5.9 \pm 2.2(MCstat)$fs .

The measured 2% statistical error corresponds to $1.07/\sqrt{N}$. This is the best resolution factor among the 1-1 analyses.

8.1.2 1-3 sample

Tab. 8.2 shows the results of the fit for the 1-3 sample. Fig. 8.2 shows the contours of λ_{fit} and κ_{fit}.

1-3 sample	Real Data	Monte Carlo
λ (cm)	0.2106 ± 0.0088	0.2190 ± 0.0034
κ	1.33 ± 0.05	1.26 ± 0.01

Table 8.2: The fitted decay length and factor κ from the 1-3 sample

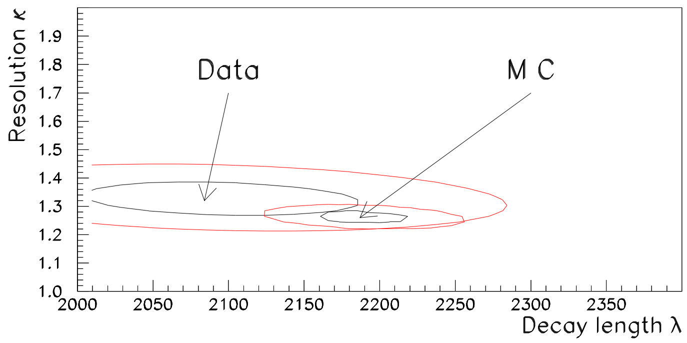

Figure 8.2: λ-κ fit contour for 1-3 sample : inner contour shows 1σ variation and outer is 2σ.

The ratio

$$\frac{\lambda_{data}}{\lambda_{MC}} = 0.962$$

corresponds to a lifetime $284.6 \pm 11.9 \pm 4.4(MCstat)$fs . The statistical error is $1.18/\sqrt{N}$.

8.2 Systematic uncertainties

8.2.1 Cuts on H-axis

In order to estimate the effect of the cut on the H-axis using the perpendicularity to the thrust axis, we switch on and off the cut. We find 0.03% (0.14%) difference in the 1-1 (1-3) sample. Expected statistical fluctuation is 0.4 % (0.6%) which is much larger than the observed fluctuation.

To check the effect of the cut on ζ, we vary the cut value from 0 to $3\sigma_\zeta$. Fig. 8.3 shows the variation of the results with the cut values. We count the maximum variations, 0.22 % in 1-1 and 0.31 % in 1-3, as systematic errors. Expected statistical fluctuations from the cut are 0.4% in 1-1 sample and 1.1% in 1-3.

The actual variations of $\lambda_{data}/\lambda_{MC}$ by the cuts on H-axis are very small compared with the expected statistical fluctuations. We find that the events rejected by the cuts have likelihood derivatives insensitive to the lifetime. This means that the rejected events do

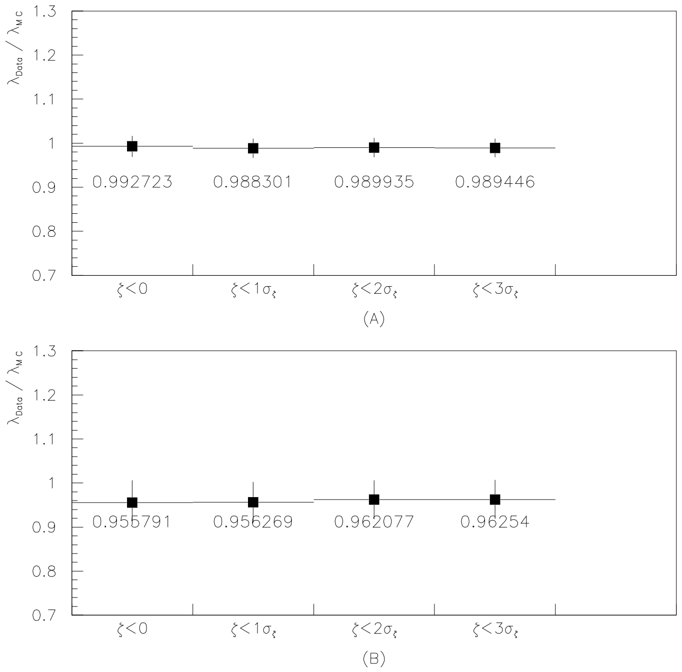

Figure 8.3: Variation of the $\lambda^{Data}/\lambda^{MC}$ with the ζ cut, (A) 1-1, (B) 1-3 sample.

not contribute much to search for λ. The induced fluctuations are consequently smaller than the expected statistical fluctuations which are calculated with the assumption of random variation of the sample.

8.2.2 Cuts on $|\delta\vec{C}_0|$ and $|\alpha^+ + \alpha^-|$ cuts

The cuts are switched on and off and the lifetime shift is taken as a systematic uncertainty. From the $|\delta\vec{C}_0|$ cut, we find ~ 0.13 % differences in our final results in both samples.

From the $|\alpha^+ + \alpha^-|$ cut, affecting only the 1-1 sample, we find 0.17 % difference in our final result.

8.2.3 Cut on the vertex probability in 1-3 analysis

We move the vertex probability cut from 10% to 0. Fig. 8.4 shows the result. Results at 5 % and 10 % include large statistical fluctuations. We take the observed 0.71 % maximum variation between 1 % and 0.01 % as the systematic uncertainty related to this cut. The variations are indeed compatible with the expected statistical fluctuations.

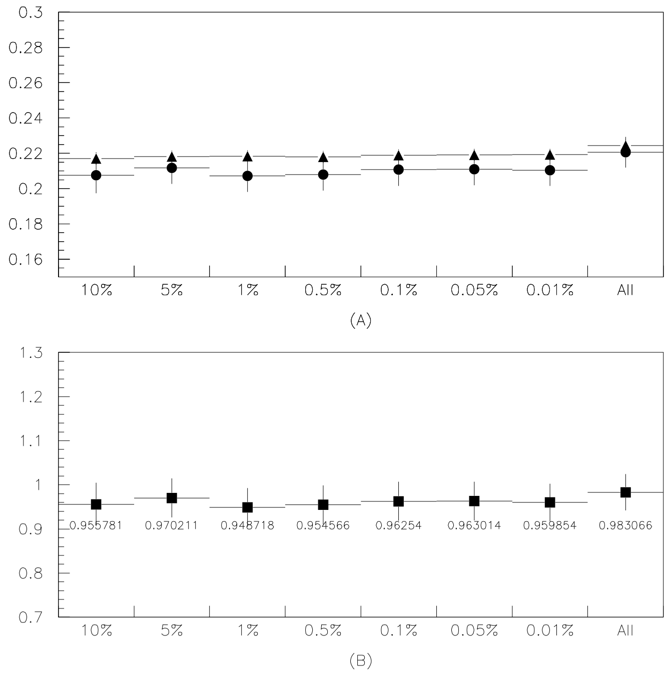

Figure 8.4: (A) Variations of the λ^{Data} and λ^{MC} with the vertex probability cut in 1-3 sample, (B) Variations of the $\lambda^{Data}/\lambda^{MC}$.

8.2.4 Non gaussian tails

Since non-gaussian tails are not considered in our likelihood function, these events could cause a bias in lifetime fit. A discrepancy on the population of this tail in real data compared to MC could induce an additional systematic uncertainty. This gave the most severe contribution of the systematic uncertainty in the IPS method, 1.33 %, [53]. [2]

In the present analysis, there are two sources of non-gaussian tails: (1) tracking, (2)

[2] Total systematic error was 1.49 %

H-axis smearing ($(l^+ + l^-)\hat{\tau} \cdot \hat{H}$).

Let us consider first the non-gaussian tails from tracking. In MC they are defined as the events with $\delta^{rec} - \delta^{tru}_{track}$ larger than $3\sigma_\delta$, where $\delta^{tru}_{track} = \delta \vec{c}_0^{tru} \cdot \hat{H}^{rec}$ and $\vec{c}_0^{tru}$ is the true 3DIP calculated from MC truth. After the likelihood cut ($P(\mathcal{F}) > 10^{-3}$), they amount to 1.3 % and 1.4 % of 1-1 and 1-3 MC samples respectively.

We assume that the uncertainty on the non-gaussian population in real data is not more than 30 %. This assumption relies on the resolution studies of $q\bar{q}$ events in [53] and is conservative comparing with their results. Fig. 8.5 and Fig. 8.6 show the changes of λ, κ and maximum likelihood when increasing the populations of non-gaussian tails in MC by up to 30 %.

We take the systematical uncertainties from the maximum variation of the results, 0.44 % and 0.41 % in 1-1 and 1-3 samples, respectively.

Now we consider the non-gaussian tail effect from H-axis smearing. When defined as $(l^+ + l^-)\hat{\tau} \cdot \hat{H} > 3\sigma_\delta$, they amount to 2.4 % and 1.6% of the 1-1 and 1-3 samples, respectively, after the likelihood cut. The uncertainty on the H-axis tail depends on the accuracy of the $\tau\tau$ event and detector simulations: 1) number of $\tau\tau\gamma$(energetic), 2) branching fractions of the undetectable hadronic channels, e.g. K^0_L. 3) Photon reconstruction efficiency 4) Non hadronic decay contributions from miss-identified electrons or muons, etc.. We find that the H-axis non-gaussian tails have no correlation with the tracking error.

When varying the population of tails in MC as we did for tracking, we find no severe decay length changes neither in 1-1 nor in 1-3 MC samples. On the contrary, we find larger values of κ's as expected. Even if we assume that the tails in real data are twice as large as in MC, κ grows up to 1.28 in both samples, but the fitted decay length is not changed. No systematic error on λ is thus added.

8.2.5 Background

Of the 1,522,800 $q\bar{q}$ MC events, 169 pass the tau selection algorithm ($0.011 \pm 0.03\%$). 48 events have less than $2GeV$ hadronic masses in both hemisphere. Only 1 event survives all cuts. Since the $q\bar{q}$ MC sample is about twice as large as real data, 0.5 $q\bar{q}$ background is expected in real data. The likelihood of the MC background event is 4.36 and $\delta = 27\mu$,

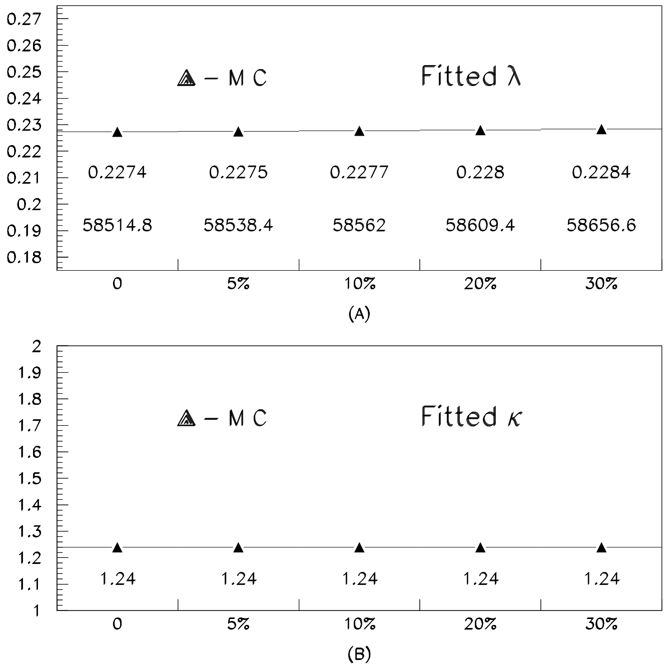

Figure 8.5: Non gaussian tail effect (from tracking) in 1-1 MC sample; (A) change of the decay length (The numbers below the fitted decay lengths are maximum likelihoods) (B) change of the resolution factor κ

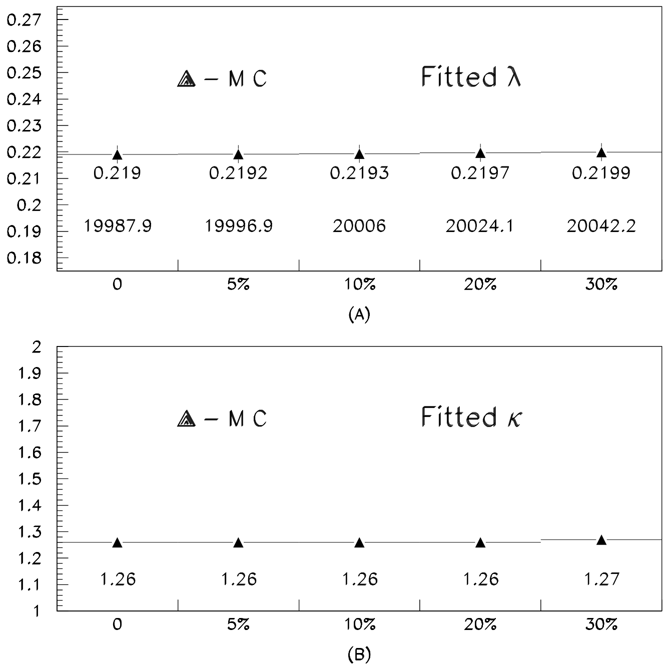

Figure 8.6: Non gaussian tail effect (from tracking) in 1-3 MC sample; (A) change of the decay length (The numbers below the fitted decay lengths are maximum likelihoods) (B) change of the resolution factor κ

$\sigma_\delta = 37\mu$, $\alpha^+ = -0.017$ and $\alpha^- = -0.086$. We simply insert this event into the real sample and we estimate the systematic error as the variation of the result. We find 1μ shift in the final result (corresponds to 0.04 %). It is compatible with the statistical fluctuation.

8.2.6 d_0, z_0 offsets

Unknown offsets on d_0 and z_0 due to possible mis-alignments of VDET layers may cause a systematic bias on the lifetime measurement. The offsets may be a function of the angle ϕ and θ depending on the geometrical alignments of each layer. Up to 50μm d_0 offsets have been observed in data. However, in IPS-like methods (unlike the IPD method), the d_0 offsets do not affect much the lifetime estimation: the effects cancel in Σd_0 due to the azimuthal symmetry of the τ decays. The same arguments apply to Δz_0. Therefore, unless very large z_0 offsets, the 3DIP method is expected to be insensitive to d_0 and z_0 offsets.

Selected $Z^0 \to \mu\mu$ events are used to study the z_0 offsets. 29,278 $Z^0 \to \mu^+\mu^-$ events collected in 1992 are processed by the 3DIP analysis programs and 10376 events pass all cuts of the method. To do this we replace the identification flag of the charged track with that of pion and we do not apply the $Z^0 \to \mu^+\mu^-$ background rejection step.

Fig. 8.7 shows the z_0 offset as a function of θ divided into twelve regions according to the ϕ angle. One can not see any significant z_0 offset when compared with the statistical fluctuations in the bins. No systematic errors are added.

8.2.7 Summary of systematic errors

Even in the case when the maximum variation is compatible with the expected statistical fluctuation, we quote conservatively the maximum variation as a systematic error. The systematic uncertainties are summarized in Tab. 8.3. We assumed no correlations between the systematic sources when adding them in quadrature to get the total systematic uncertainty.

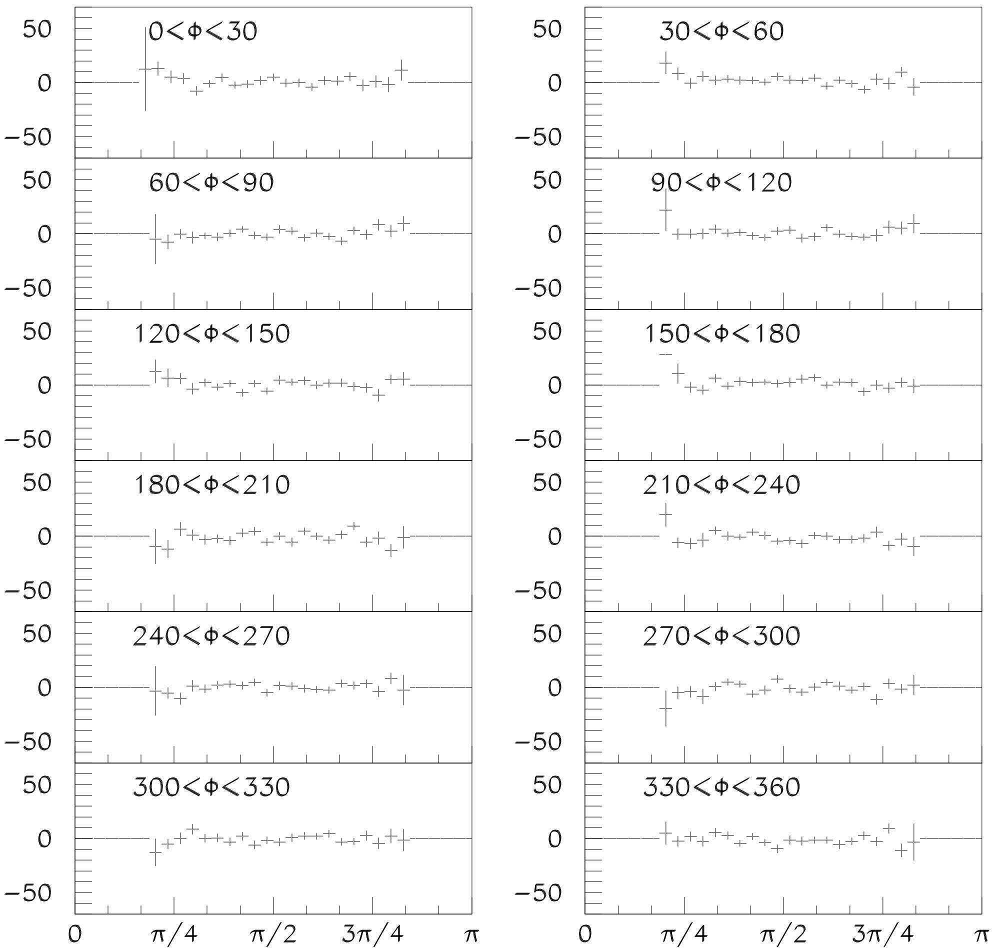

Figure 8.7: z_0 offset (in μm), mean of Δz_0's of muon pairs, as a function of θ per 30° slices of ϕ

Source \	1-1	1-3
Monte Carlo Statistics	2.19 fs	4.42 fs
$q\bar{q}$ background	negligible	negligible
Cut on vertex χ^2	-	2.03 fs
Cut on $\hat{H} \cdot Thrust$	0.08 fs	0.39 fs
Cut on ζ	0.64 fs	0.89 fs
Cut on $\lvert\delta\vec{C}_0\rvert$	0.39 fs	0.37 fs
Cut on $\lvert\alpha^+ + \alpha^-\rvert$	0.51 fs	-
Non-gaussian tail	1.29 fs	1.17 fs
Total	2.70 fs	5.11 fs

Table 8.3: Summary of systematic errors.

8.3 Systematical checks of the method

In this section we discuss various checks of the method. First we discuss the correlation problem of simultaneous λ-κ fitting, which has not been tried before in IPS and/or MIPS. This has been done in DL method where decay lengths are much larger than errors as in the present method. Secondly we consider another fitting scheme where the experimental error is modeled by $\sigma^{Exp} = \sigma^{measured} \oplus \rho$ and check the λ fit dependence on the error scheme. We show also the stability of the method against missing errors. Finally we fit the decay length λ with zero lifetime events to check the behavior of the simultaneous λ-κ fit in the extreme range ($\lambda \sim 0$).

8.3.1 How can λ and κ be fitted simultaneously?

In the IPS or MIPS method, the fitted lifetime is sensitive to the d_0 resolution assumed in the likelihood function. About 10 % uncertainty on d_0 resolution yields more than 1% change of the lifetime in IPS-like methods. The measurement of d_0 resolution is a crucial point and has been done with $Z^0 \rightarrow \mu\mu$ sample which contains no lifetime effect and no beam size contributions in $\sum d_0$. However the momentum characteristics of $\mu\mu$ samples are quite different from $Z^0 \rightarrow \tau\tau$ events since μ pairs carry most of the beam energy. So the IPS resolution studies have been developed using other samples, $Z^0 \rightarrow e^+e^-$ and $\gamma\gamma \rightarrow \mu^+\mu^-$, $\gamma\gamma \rightarrow e^+e^-$, and $Z^0 \rightarrow q\bar{q}$. Furthermore, the present lifetime analysis is applied only to tau decays to hadrons, thus 3DIP might be affected by the scattering of the tracks through strong interactions with matter which is not present in $Z^0 \to \mu^+\mu^-$ events.

We therefore choose to fit λ with κ to compensate the uncertainty of δ resolution. Comparing Fig. 6.4 and Tabs. 8.1 and 8.2, the fitted resolution factors κ of 1-1 ($\kappa = 1.24$) and 1-3 ($\kappa = 1.26$) samples reproduce the MC true resolutions. Furthermore the fit contours of Fig. 8.1 and Fig. 8.2 show little correlation between λ and κ fits. As we discussed shortly in Sec. 6.3, this means that the events split into two different types; one contains the information on resolution and the other contains the information on decay length. The two types can be separated when considering the second derivatives of the likelihood function.

Let λ_{fit} and κ_{fit} be the fitted decay length and the fitted resolution factor corresponding to $(\ln\mathcal{L})_{max}$. It is clear that

$$(\frac{\partial \ln\mathcal{L}}{\partial\lambda})_{\lambda=\lambda_{fit}} = 0$$
$$(\frac{\partial \ln\mathcal{L}}{\partial\kappa})_{\kappa=\kappa_{fit}} = 0$$

Therefore searching for the maximum of $\ln\mathcal{L}$ is identical to finding λ_{fit} and κ_{fit} to make $\sum\frac{F'}{F} = 0$, where $\mathcal{L} = \prod F(\delta, \alpha^+, \alpha^-, \sigma; \lambda, \kappa)$.

The second derivative of $F(\delta, \alpha^+, \alpha^-, \sigma; \lambda, \kappa)$ with respect to λ or κ gives the decline of the first derivative and tells the steepness of the likelihood curve around the maximum. So an event with large second derivatives plays an important role to find $(\ln\mathcal{L})' = 0$. Lifetime is determined by the events where the second derivatives with respect to λ are large. Resolution is mainly determined by the events with large second derivative on κ.

Fig. 8.8 shows the second derivatives for the events with $P(\mathcal{F}) < 0.1$. [3]

The events are clearly subdivided into two groups. Events with large negative $\partial^2F/\partial\lambda^2$ have $\partial^2F/\partial\kappa^2 \sim 0$ (Group A): they are useful to fit λ but are useless to fit κ. Events with large negative $\partial^2F/\partial\kappa^2$ have $\partial^2F/\partial\lambda^2 \sim 0$ (Group B): they contain information on the resolution, but not on the lifetime.

[3]The events with large probability $P(\mathcal{F})$ have nearly same distribution as Fig. 8.8 but both second derivatives $\partial^2F/\partial\lambda^2$ and $\partial^2F/\partial\kappa^2$ are smaller. They contribute weakly to the maximum likelihood determination.

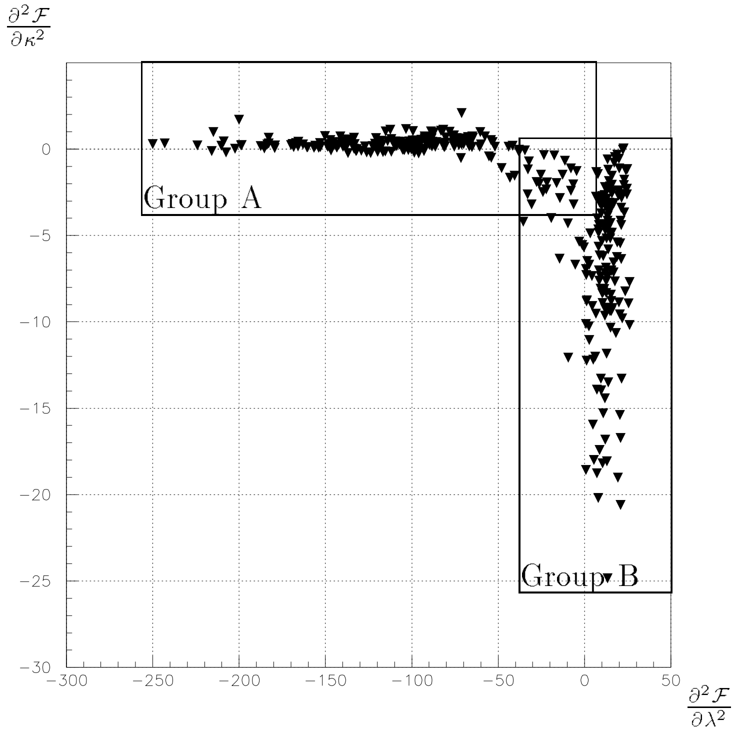

Figure 8.8: Second derivatives on λ and κ

Fig. 8.9 shows the clear difference of the δ distributions between the two groups. The events in the group A show large $|\delta|$ with physical configurations (δ, $\alpha^{\pm}$), and distribute exponentially (Fig. 8.9(A)). Thus, the mean decay length is extracted from the events of Group A. The events in the group B have $\delta \sim 0$ with a gaussian distribution (Fig. 8.9(B)) due to resolution. Group B contains events with unphysical configurations when δ and $\alpha^{\pm}$ have values consistent only within errors. Then the resolution is measured from the events in Group B.

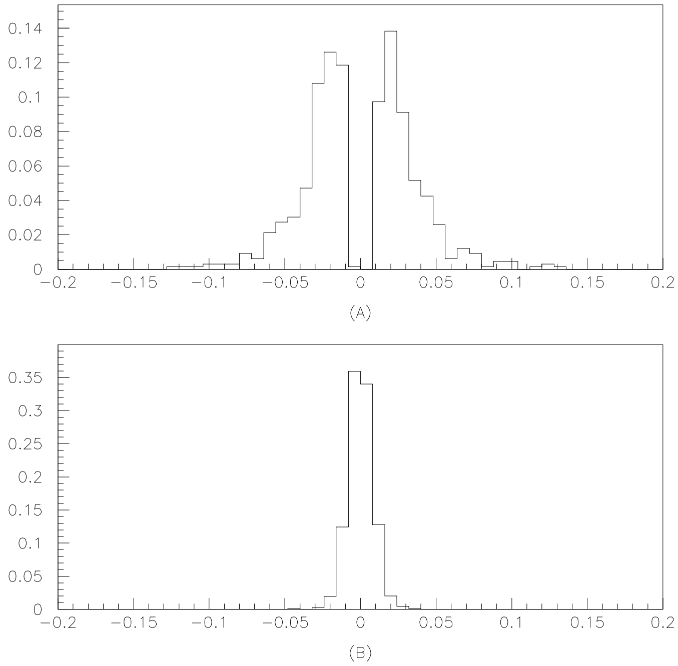

Figure 8.9: δ distribution of (A) the events containing lifetime information (B) the events containing resolution information.

8.3.2 Will λ be stable with an additional gaussian error?

Another way to check the decoupling of λ and κ fits is to check the stability of the lifetime on an artificial increase of the δ uncertainty.

We enter an additional gaussian error which transforms $\delta \rightarrow \delta + \eta$, where η is a random number from a normal distribution with a width η_0 ($\eta_0 = 5\mu$, 10μ, 20μ, 30μ).

Considering the average value of σ_δ ($\sim 50\mu$ in 1-1 and $\sim 40\mu$ in 1-3) an additional error of 30μ is equivalent to a ~ 20 % increase of σ_δ in 1-1 and ~ 25 % increase in 1-3.

Fig. 8.10 and Fig. 8.11 show the results on the 1-1 samples and 1-3 samples, respectively.

Most of the effect of the additional error is swallowed by the κ factor. A change of 5 % in the resolution affects the λ fit less than 0.3 % and the κ fit by 4 %.

8.3.3 The fitting scheme: with κ or ρ?

Instead of the multiplicative κ scheme to describe the uncertainty of d_0 resolution, we can adopt an additive ρ scheme where the formula $\sigma^{exp} = \kappa\sigma^{measured}$ changes to $\sigma^{exp} = \sigma^{measured} \oplus \rho$.

Tab. 8.4 shows the results under the $\lambda - \kappa$ and $\lambda - \rho$ schemes for each samples.

Samples	1 - 1		1 - 3	
Data	Data	MC	Data	MC
λ (cm)	0.2250 ± 0.0045	0.2274 ± 0.0017	0.2106 ± 0.0088	0.2190 ± 0.0034
κ	1.26 ± 0.03	1.24 ± 0.01	1.33 ± 0.05	1.26 ± 0.01
λ (cm)	0.2252 ± 0.0046	0.2281 ± 0.0017	0.2106 ± 0.0088	0.2192 ± 0.0033
ρ (μ)	31 ± 2	29 ± 1	30 ± 5	27 ± 1

Table 8.4: Results from $\lambda - \kappa$ and $\lambda - \rho$ schemes

There is 0.22 % difference of l^{data}/l^{MC} in 1-1 sample and this corresponds to $0.63fs$. In 1-3 sample 0.09 % difference is found and corresponds to $0.25fs$. The differences indicate that there is no severe dependence of λ fit on the resolution scheme.

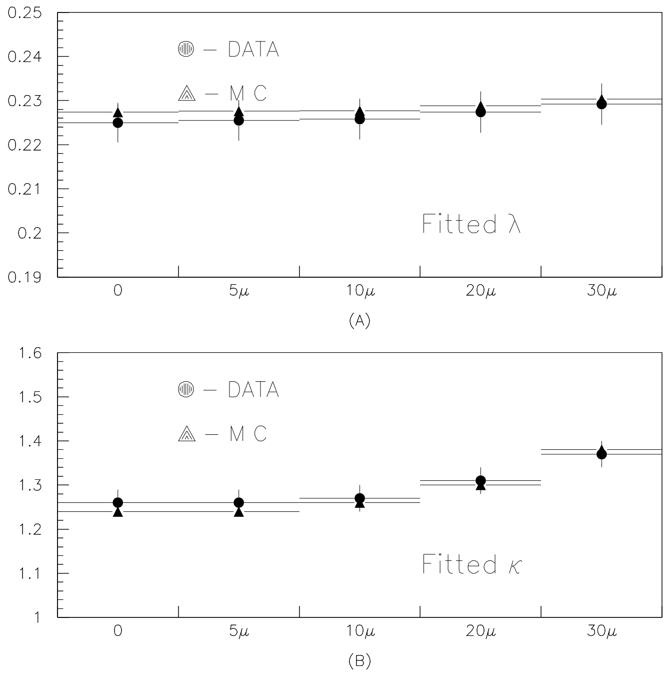

Figure 8.10: Changes of λ and κ with additional gaussian errors in 1-1 sample: (A) Fitted λ (B) Fitted κ

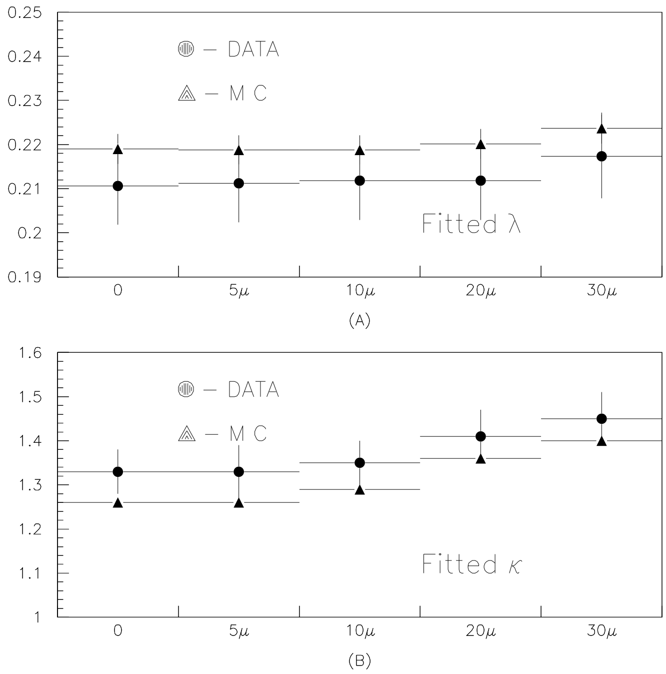

Figure 8.11: Changes of λ and κ with additional gaussian errors in 1-3 sample: (A) Fitted λ (B) Fitted κ

8.3.4 Is $\lambda_{fit} = 0$ for zero lifetime event?

One frequently uses the zero lifetime events, like $Z^0 \to \mu^+\mu^-$, $Z^0 \to e^+e^-$, etc., to obtain the tracking resolution. Conversely these events can be used to check a possible bias on the λ fit.

10376 $Z^0 \to \mu^+\mu^-$ events used in the z_0 offset study are entered to the same likelihood fit program.

Fig. 8.12 shows the contour plot of λ-κ fit.

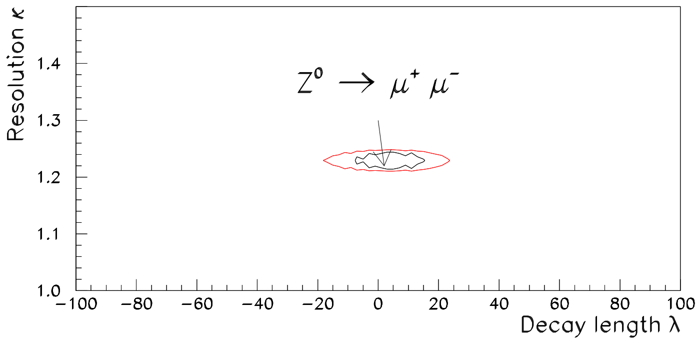

Figure 8.12: λ-κ fit contour for $Z^0 \to \mu^+\mu^-$: inner contour shows 1σ variation and outer is 2σ.

The fitted values

$$\begin{aligned} \lambda_{fit}^{Z^0\to\mu^+\mu^-} &= 2 \pm 14\mu \\ \kappa_{fit}^{Z^0\to\mu^+\mu^-} &= 1.22 \pm 0.01 \end{aligned}$$

rule out a systematic bias of the lifetime and confirm the δ resolution fitting. Assuming the true $\delta = 0$, the plot of δ/σ_δ of $Z^0 \to \mu^+\mu^-$ events (Fig. 8.13) measures the resolution scaling factor κ. The width of the δ/σ_δ distribution, 1.24, is remarkably consistent with κ_{fit}.

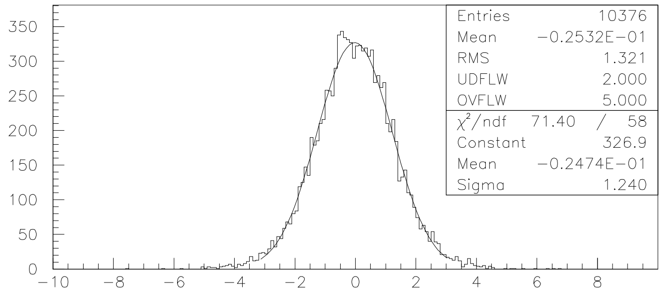

Figure 8.13: δ/σ_δ for $Z^0 \to \mu^+\mu^-$ events

8.4 Correlations with other methods

The present method uses the tau to hadron decay events. Our samples are, therefore, sub-samples of the other methods. The 1-1 analysis uses a sub-sample of the IPS or IPD analyses. The 1-3 analysis uses a sub-sample of the DL method but use also 1-prong hemisphere. It is important to measure the statistical correlations between this method and the others.

8.4.1 1-1 analysis and MIPS method

The quantity δ can be split into $(d_0^+ + d_0^-)$ and $(z_0^+ - z_0^-)$ terms. Since we use d_0 sum, our lifetime measurement is correlated with IPS-like methods. However the correlation is limited because we use $(z_0^+ - z_0^-)$ too and a projection on $\hat{H}$. In order to compute the correlation between 1-1 analysis and MIPS method, the tau MC events are divided into 100 sub-samples and the decay length is fitted separately by the two methods. Fig. 8.14 shows the correlation. The obtained correlation factor is 0.64. We can expect nearly the same correlation with IPS since IPS and MIPS are about 90 % correlated.

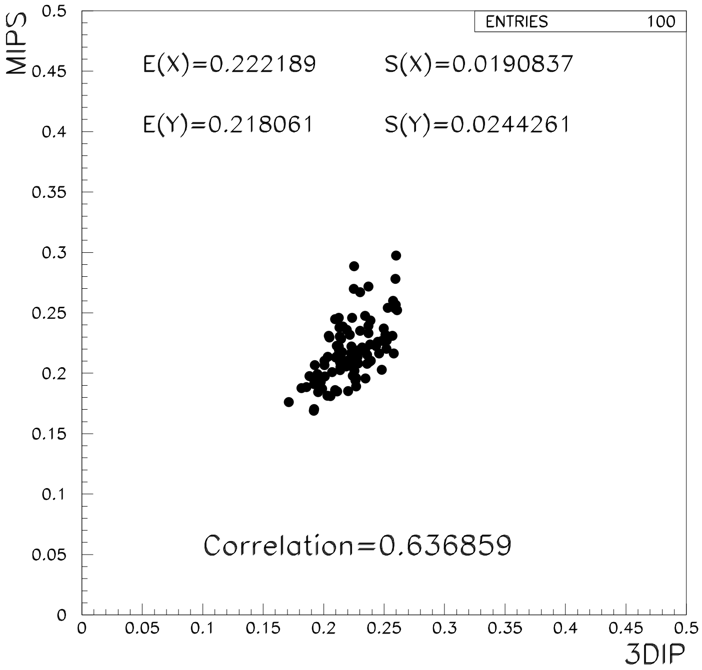

Figure 8.14: Statistical correlation between 3DIP and MIPS using 100 subsample from 1-1 MC

8.4.2 1-3 analysis and DL method

The DL method is done by measuring the distance between the secondary vertex and the primary vertex. The lifetime, therefore, comes only from the 3-prong side.

In the present method as seen in the dependence of the likelihood function $F(\delta, \alpha^+, \alpha^-, \sigma)$ on $\alpha^\pm$, when a hemisphere has $\alpha \sim 0$, the term $e^{Q^2}\mathrm{erfc}(Q)$ goes to zero, and the likelihood is determined only by the other hemisphere. This situation occurs in 1-3 sample.

Fig. 8.15 shows $\alpha^{1-prong}$ and $\alpha^{3-prong}$ in 1-3 sample.

Because the energy of hadron in the 3-prong tau decay is carried mainly by charged tracks, the absolute mean of $\alpha^{3-prong}$ is smaller than that of $\alpha^{1-prong}$: $\sim 9mrd$ on the 3-prong side against $\sim 33mrd$ on the 1-prong side. Therefore the lifetime information from the 3 prong side does not contribute much to the maximum likelihood.

We can then expect that our 1-3 analysis gives a result statistically not much correlated with the DL method in which lifetime is determined only by the 3-prong side.

In order to compute the correlation between 1-3 analysis and DL method, the tau MC

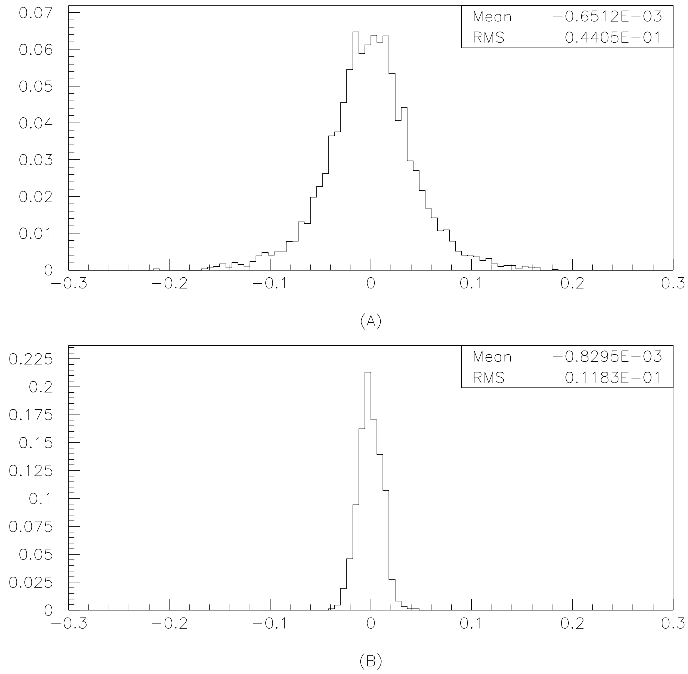

Figure 8.15: (A) $\alpha^{1-prong}$, (B) $\alpha^{3-prong}$ distributions according to their decay topology

events are divided into 100 sub-samples and the decay length is fitted separately by the two methods. As expected, a correlation smaller than 17% is obtained between DL and the present method (Fig. 8.16).

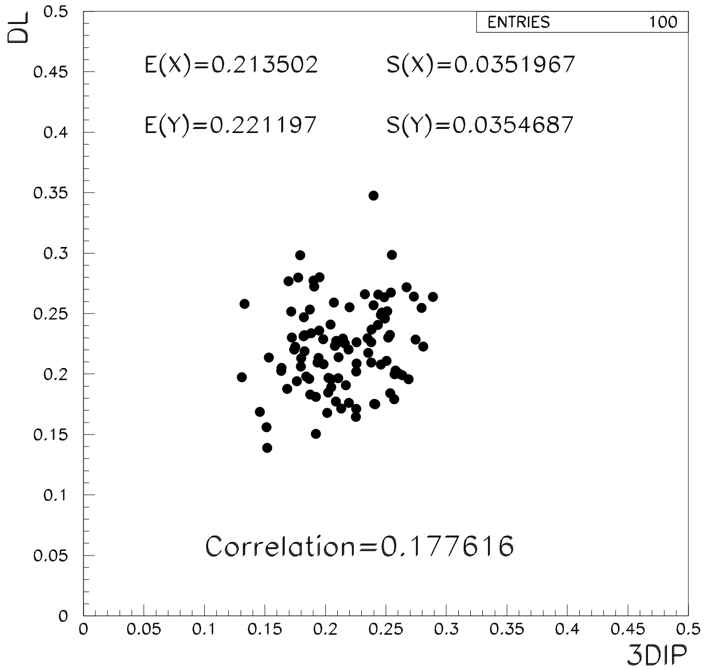

Figure 8.16: Statistical correlation between 3DIP and DL using 100 subsample from 1-3 MC

Chapter 9

Conclusion

9.1 Tau lifetime and universality check

The τ lifetime has been measured by a maximum likelihood fit using the 3-D impact parameter sum in $Z^0 \to \tau^+\tau^-$ events when both τ decay to hadrons.

The results from the 3DIP method for 1-1 and 1-3 samples using 1992 data are, respectively,

$$\begin{aligned} \tau_\tau^{1-1} &= 292.9 \pm 5.9 \pm 2.7\text{fs} \\ \tau_\tau^{1-3} &= 284.6 \pm 11.9 \pm 5.1\text{fs} \end{aligned}$$

where we used 2840 (1-1) and 794 (1-3) accepted $\tau^+\tau^-$ events by the method. The statistical precisions are $1.07/\sqrt{N_{\tau\tau}}$ and $1.18/\sqrt{N_{\tau\tau}}$ respectively.

The two measurements agree within their errors. The combined result of $1-1$ and $1-3$ analyses is

$$\tau_\tau = 290.8 \pm 5.3 \pm 2.7\text{fs}$$

and gives $1.10/\sqrt{N_{\tau\tau}}$ statistical precision.

The lifetime reported here can now be used in the test of universality of lepton couplings to weak charged boson (Eq. 1.4, Eq. 1.5). Since 1992 there has been also a lot of measurements on the tau mass and the leptonic branching ratio, and many measurements on the lifetime with new methods. The current world averages [67]:

$$\begin{aligned} m_\tau &= 1777.0 \pm 0.3\mathrm{MeV/c^2} \\ \tau_\tau &= 291.5 \pm 1.6\mathrm{fs}(\text{ including the present measurement}) \\ B_e &= 17.79 \pm 0.09\% \end{aligned}$$

yield a good agreement of the lepton universality ($\sim 0.5\sigma$):

$$(\frac{g_\tau}{g_\mu})^2 = 0.9964 \pm 0.0055(\tau_\tau) \pm 0.0008(m_\tau) \pm 0.0051(B_e)$$

$$\boxed{(\frac{g_\tau}{g_\mu}) = 0.9982 \pm 0.0038}$$

Fig. 9.1 shows the current status of the universality check.

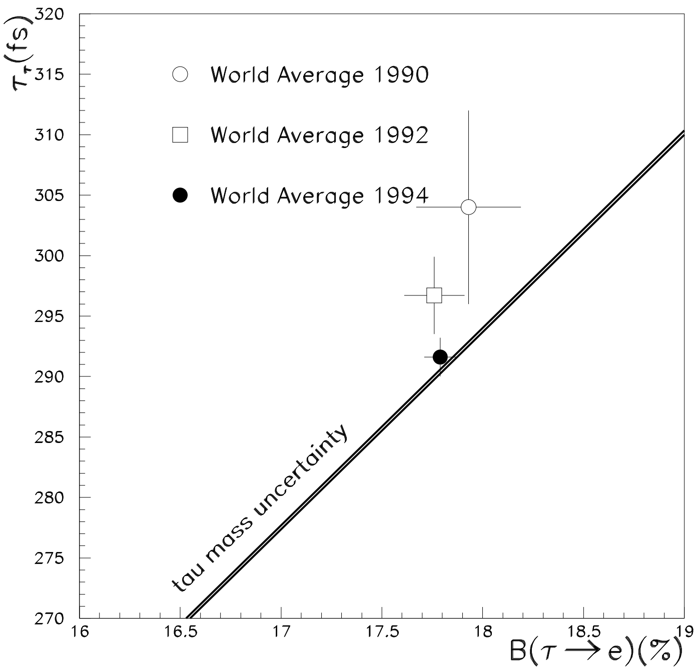

Figure 9.1: Current status of lepton universality checks from τ decay.

The result on the tau to muon branching ratio, $B_\mu = 17.33 \pm 0.09\%$, also gives a good agreement of the lepton universality ($\sim 0.3\sigma$):

$$\boxed{(\frac{g_\tau}{g_e}) = 0.9988 \pm 0.0038}$$

9.2 Prospects

Some important features make the 3DIP method very promising when statistics increase.

- The method makes use of the full detector informations. The detector performance allows a background free selection of hadronic τ decays with very high efficiency. The precise measurements of d_0 and z_0 from VDET and of full charged and neutral energies allow precise measurements of the 3DIP and H-axis.

- The special projection onto H-axis makes the measurement be free from the uncertainty on beam size and the uncertainty on tau direction.

- The experimental resolution can be fitted together with decay length. The fitted resolution scaling factor (κ) is in excellent agreement with resolution distributions in tau Monte Carlo and in $Z^0 \to \mu\mu$ data. This method allows, therefore, a self consistent and self calibrating analysis of tau lifetime independent from the resolution study using $Z^0 \to \mu^+\mu^-$ and/or $\gamma\gamma \to \mu^+\mu^-$ or $Z^0 \to q\bar{q}$.

- The method has good stability against the systematical uncertainties. The main source of systematic error in 3DIP method is presently Monte Carlo statistics (0.8% in 1-1 analysis, 1.5% in 1-3). Intrinsic systematic uncertainties are 0.5% in 1-1 and 0.8% in 1-3, where in 1-3 analysis the uncertainty from vertexing is dominant.

- In 1-3 analysis with the 3DIP method, the lifetime is mainly determined from the 1-prong τ decay. The 1-3 analysis gives a statistically uncorrelated result with DL method (correlation $\sim$ 17 %). This is the first measurement in ALEPH using the 1-prong side of the 1-3 events.

The method works only in the hadronic-hadronic $\tau^+\tau^-$ decay events since it uses 2-body kinematics, therefore, only 40% of the tau pairs can be used according to the hadronic branching fraction. The acceptance of the method is limited by the track quality cut on the full VDET hit ($r\phi$ and rz) in the preliminary selection ($\varepsilon \sim 0.75$), cut on the badly measured H-axis($\varepsilon \sim 0.83$), and cuts on VDET pattern ($\varepsilon \sim 0.55$) and vertex fit probability ($\varepsilon \sim 0.85$) in 1-3 analysis. The overall acceptance of the method is about 11% ($N_{\tau\tau}^{prod}$).

We expect to get about 155K τ pairs at the end of 1994 running, so we may have 13K τ pair events to be used in 3DIP method. With the statistical precision $1.1/\sqrt{N_{\tau\tau}}$, 3DIP method is likely to reach a statistical error of 0.95% which is comparable with other methods. 3DIP method already reaches that level of systematic errors due to stability against possible uncertainties. The increase in statistics will also benefit to the systematic error estimations and the method is likely to be limited by the statistical error up to the end of LEP running. The lifetime result from 3DIP method will have a statistically important meaning since the method has low statistical correlation (~ 0.64 in 1-1 and ~ 0.17 in 1-3) with other precision methods.

Improvement of acceptance of the method by optimization of the inefficient cuts or extension to the leptonic tau decay events may allow more precise result on the lifetime in the future.

Appendix A

Track Fit and Helix Parameter Definition

Charged track reconstruction uses VDET, ITC and TPC hits (a maximum of 31 three dimensional points for each charged track, 21 points from TPC, 8 from ITC, 2 from VDET). Since the magnetic field is rather uniform, the trajectory of a particle can be well described as a helix. The five following helix parameters are chosen to describe a track with respect to the detector origin:

- $1/R_0$: Inverse radius of curvature of a track in the x-y plane (signed)
- $\tan\lambda$: P_z/P_t tangent of the dip angle
- ϕ_0 : angle in the x-y plane at the point of closest approach to the z axis
- d_0 : impact parameter in the x-y plane (signed), radial distance of the point of minimum approach of a track to the z-axis
- z_0 : z-coordinate of the point of minimum approach

The sign of $1/R_0$ is given as positive for a negative charged particle. The sign of d_0 is equal to the sign of the angular momentum of the particle with respect to the z axis (Fig. A.1).

The track reconstructed in the TPC is extrapolated to the ITC and the helix is refitted with the ITC hits which are associated to the particle. VDET hits on both $r\phi$ and z faces

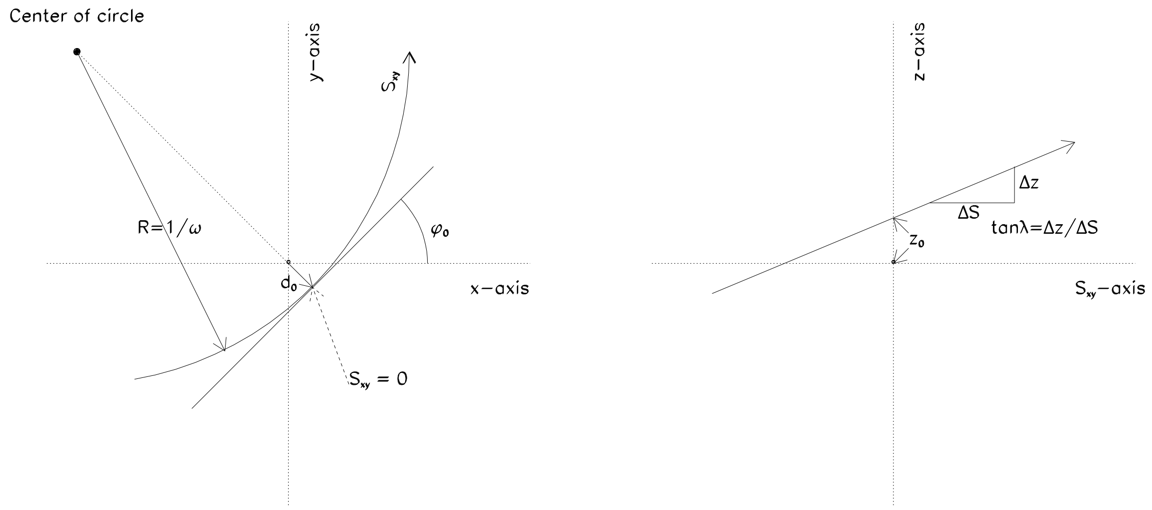

Figure A.1: Helix parameters used in the ALEPH track fit. d_0 and $1/R$ are positive. z_0 is the z-coordinate of the d_0 point in the x-y plane.

from the two layers are associated to the tracks which extrapolate close to them. The extrapolation of the TPC-ITC track is not very precise ($\sim 100\mu$m in $r\phi$, ~ 0.8mm in rz) and frequently more than one VDET hit can be associated with a track. In most cases, this can be resolved by matching the direction of the VDET hits from the 2 layers and the direction of the TPC-ITC track (this can not be done when there exists only one hit in VDET layers). The track-hit association is done on the basis of the following χ^2 minimization:

$$\chi^2 = (x^{VDET} - x^{TPC-ITC})_i^{-1} S_{ij} (x^{VDET} - x^{TPC-ITC})_j$$

where, i and j run from 1 to 4 (1: $r\phi$ inner layer, 2: z inner layer, 3: $r\phi$ outer layer, 4: z outer layer), S_{ij} is the 4×4 matrix of the track extrapolation. It is allowed to share a hit which is already associated with an other track.

The final fit of the helix parameters, $(1/R_0, \tan\lambda, \phi_0, d_0, z_0)$ is done in two consecutive steps:

- Fast estimation: Find $1/R_0, \phi_0, d_0$ by treating a track as a circle in the x-y plane and $\tan\lambda, z_0$ by treating a track as a line in the $S_{xy} - z$ plane.

- Newtonian iteration: Improve the χ^2 of the helix parameters by considering the multiple scattering in the TPC, ITC and VDET materials through Kalman filtering [68]

Appendix B

Transformation of helix parameters with respect to the beam position

The helix parameters of a track with respect to the measured beam position, $\vec{B} = (B_x, B_y)$ can be obtained from the helix parameters in the detector system with respect to the detector origin, $\vec{O} = (0, 0, 0)$. This transformation plays an important role when the average beam position is far from the detector origin.

Let the helix parameters of a charged track with respect to the detector origin be $h = (1/R_0, \tan\lambda, \phi_0, d_0, z_0)$. The projection of the helix is a circle onto the x-y plane, and a straight line onto the r-z plane (Fig B.1).

The center, $\vec{C}$, of the circle in x-y can be obtained from the helix parameters:

$$\begin{aligned} C_x &= (d_0 - R_0)\sin\phi_0 \\ C_y &= -(d_0 - R_0)\cos\phi_0 \end{aligned}$$

The new impact parameter must be calculated with respect to the beam position, $\vec{B}$. The minimum approach point $(\phi_0^{BP}, d_0^{BP}, z_0^{BP})$ can be obtained from the old minimum approach point (ϕ_0, d_0, z_0) by a rotation of the angle Ω with respect to $\vec{C}$,

$$\Omega = \sin^{-1}\left(\frac{\vec{CO}}{|\vec{CO}|} \times \frac{\vec{CB}}{|\vec{CB}|}\right)$$

The new helix parameters are

$$1/R_0^{BP} = 1/R_0$$

Figure B.1: Schematic diagram of the transformation of a helix parameters with respect to the beam position

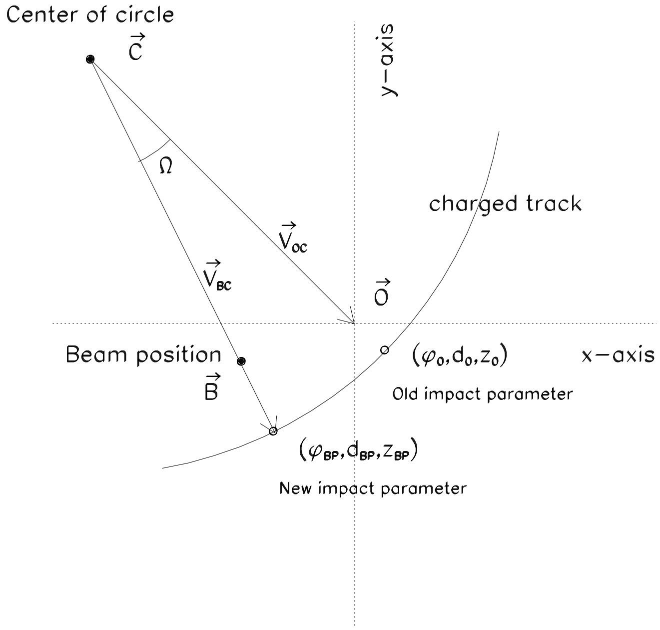

$$
\begin{aligned}
\tan \lambda^{BP} &= \tan \lambda \\
\phi_0^{BP} &= \phi_0 + \Omega \\
d_0^{BP} &= -Q(|R_0| - |\vec{CB}|) \\
z_0^{BP} &= z_0 + R_0 \Omega \tan \lambda
\end{aligned}
$$

where the Q is opposite to the sign of the charged track.

Appendix C

Secondary vertex finding and calculation of the helix parameters of a sum track

C.1 Vertex finding in ALEPH

The τ decay vertex is found by fitting the common vertex of its N charged daughter tracks, minimizing the following χ^2,

$$\chi^2 = \sum_{i=1}^{N} (\vec{h}_v - \vec{h}_0)_i^T C_{h_i}^{-1} (\vec{h}_v - \vec{h}_0)_i + (\vec{v} - \vec{v}_0)^T C_{v_0}^{-1} (\vec{v} - \vec{v}_0) \tag{C.1}$$

where $\vec{h}_v$ is the recalculated helix parameters of each daughter constrainted to have the vertex v and $(\vec{h}_0)_i$ and C_{h_i} are the original helix parameters and the covariant error matrix of the ith track. $\vec{v}$ and $\vec{v}_0$ are the vertex to be fitted and the priori vertex, respectively. Several algorithms are available in the ALEPH experiment (YTOP, FV, ..).

C.1.1 Calculation of the helix parameter of a sum track

Once we have the vertex and momenta of the daughter tracks, the helix parameters of the sum track can be calculated. Let us define the fitted secondary vertex, $\vec{V} = (V_x, V_y, V_z)$,

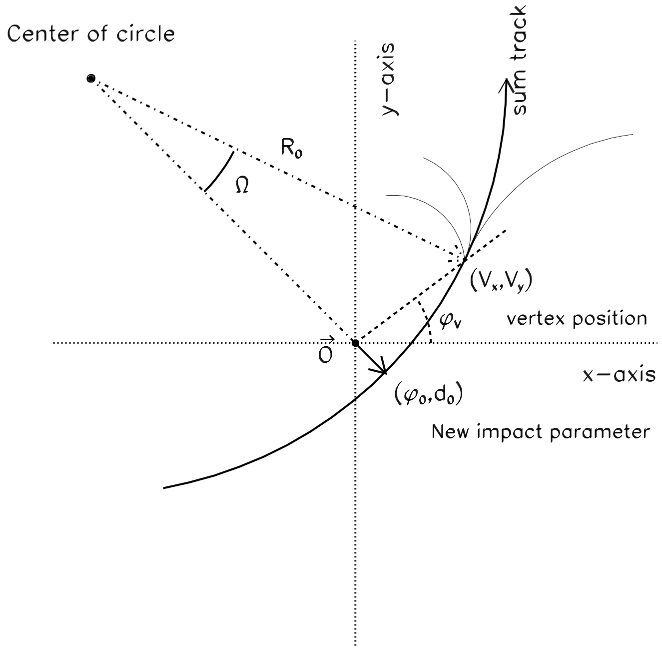

Figure C.1: Illustration of the sum track and its track parameters

and the sum track momentum, $\vec{P} = (P_x, P_y, P_z)$ (Fig. C.1). The first helix parameter, the inverse radius ($1/R_0$), is directly deduced from the transverse momentum of the sum track.

$$1/R_0 = -Q/P_t \times constant$$

where Q is the sum track charge (± 1) and $constant = B(T) \times 0.0029979$. The second parameter is $\tan\lambda = P_z/P_t$. The center of the circle in the x-y plane can be calculated from the direction vectors $u_x = P_x/P_t$ and $u_y = P_y/P_t$.

$$\begin{aligned} x_c &= V_x + Q|R_0|u_x \\ y_c &= V_y - Q|R_0|u_y \end{aligned}$$

With the detector origin ($\vec{O} = (0,0)$), the vertex in the x-y plane ($\vec{V} = (V_x, V_y)$) of the circle, and the coordinates of the center ($\vec{C} = (x_c, y_c)$), we can calculate a rotation angle Ω as seen in the previous section. With the azimuthal angle, $\phi_V = \tan^{-1}(V_y/V_x)$, of the vertex in the x-y plane, the helix parameters of the sum track with respect to the detector origin are

$$\begin{aligned} 1/R_0 &= -Q/P_t \times constant \\ \tan\lambda &= P_z/P_t \end{aligned}$$

$$
\begin{aligned}
\phi_0 &= \phi_v + \Omega \\
d_0 &= -Q(|R_0| - R_c) \\
z_0 &= V_z + R_0 \Omega \tan \lambda
\end{aligned}
$$

where $R_c = \sqrt{x_c^2 + y_c^2}$.

Appendix D

Smearing of 3DIP equation from beam size

When charged tracks are treated as straight lines in a small region (beam envelope) and the tau origin, $\vec{\tau}_0$, is inside the beam envelope, a 3DIP with respect to the true tau origine is related to the reconstructed 3DIP as follows

$$\begin{aligned}
(c_{0x}^{\pm})' &= (d_0^{\pm})'(\sin\phi^{\pm})' = d_0^{\pm}\sin\phi^{\pm} + S_{xy}\cos\phi^{\pm} \\
(c_{0y}^{\pm})' &= -(d_0^{\pm})'(\cos\phi^{\pm})' = -d_0^{\pm}\sin\phi^{\pm} + S_{xy}\sin\phi^{\pm} \\
(c_{0z}^{\pm})' &= (z_0^{\pm})' = z_0^{\pm} + S_{xy}\tan\lambda^{\pm}
\end{aligned}$$

where $(\phi^{\pm})' = \phi^{\pm}$ and $(\lambda^{\pm})' = \lambda^{\pm}$. Then, the 3DIP difference with respect to the true tau origine is,

$$\begin{aligned}
(\delta c_{0x})' &= \delta C_{0x} + S_{xy}^{+}\cos\phi^{+} - S_{xy}^{-}\cos\phi^{-} \\
(\delta c_{0y})' &= \delta C_{0y} + S_{xy}^{+}\sin\phi^{+} - S_{xy}^{-}\sin\phi^{-} \\
(\delta c_{0z})' &= \delta C_{0z} + S_{xy}^{+}\tan\lambda^{+} - S_{xy}^{-}\tan\lambda^{-}
\end{aligned}$$

Considering beam size, σ_x^{BS} and σ_y^{BS}, S_{xy}^{+} and S_{xy}^{-} can be rewritten using these uncertainties.

$$\boxed{S_{xy}^{\pm} = \sigma_x^{BS}\cos\phi^{\pm} + \sigma_y^{BS}\sin\phi^{\pm}} \tag{D.1}$$

Thus,

$$(\delta c_{0x})' = \delta c_{0x} + +\sigma_x^{BS}(\cos\phi^{+}\cos\phi^{+} - \cos\phi^{-}\cos\phi^{-}) + \sigma_y^{BS}(\sin\phi^{+}\cos\phi^{+} - \sin\phi^{-}\cos\phi^{-})$$

$$
\begin{aligned}
(\delta c_{0y})' &= \delta c_{0y} + +\sigma_x^{BS}(\cos\phi^+ \sin\phi^+ - \cos\phi^- \sin\phi^-) + \sigma_y^{BS}(\sin\phi^+ \sin\phi^+ - \sin\phi^- \sin\phi^-) \\
(\delta c_{0z})' &= \delta c_{0z} + +\sigma_x^{BS}(\cos\phi^+ \tan\lambda^+ - \cos\phi^- \tan\lambda^-) + \sigma_y^{BS}(\sin\phi^+ \tan\lambda^+ - \sin\phi^- \tan\lambda^-)
\end{aligned}
$$

Neglecting the errors on the directions of the charged tracks, the error components of the 3DIP difference are

$$
\begin{aligned}
\sigma(\delta c_{0x}) &= \sigma_x^{BS}(\cos\phi^+ \cos\phi^+ - \cos\phi^- \cos\phi^-) \oplus \sigma_y^{BS}(\sin\phi^+ \cos\phi^+ - \sin\phi^- \cos\phi^-) \\
\sigma(\delta c_{0y}) &= \sigma_x^{BS}(\cos\phi^+ \sin\phi^+ - \cos\phi^- \sin\phi^-) \oplus \sigma_y^{BS}(\sin\phi^+ \sin\phi^+ - \sin\phi^- \sin\phi^-) \\
\sigma(\delta c_{0z}) &= \sigma_x^{BS}(\cos\phi^+ \tan\lambda^+ - \cos\phi^- \tan\lambda^-) \oplus \sigma_y^{BS}(\sin\phi^+ \tan\lambda^+ - \sin\phi^- \tan\lambda^-)
\end{aligned}
$$

Appendix E

Tau decay vertex finding using kinematics

In real space, two tau decay vertex $\vec{V}^{\pm}$ can be represented by using the tau origin ($\vec{\tau}_0$) and the tau direction ($\hat{\tau}^{\pm}$) vectors, or using the 3DIP ($\vec{c}_0^{\pm}$) and the charged track direction ($\hat{c}^{\pm}$) vectors:

$$\vec{\tau}_0 + l^{+}\hat{\tau} = \vec{c}_0^{+} + \epsilon^{+}\hat{c}^{+}$$
$$\vec{\tau}_0 - l^{-}\hat{\tau} = \vec{c}_0^{-} + \epsilon^{-}\hat{c}^{-}$$

where $\hat{\tau} \equiv \hat{\tau}^{+} = -\hat{\tau}^{-}$. Subtraction of above two equations makes,

$$\hat{\tau} = \frac{1}{\chi}(\vec{\delta}_0 + \epsilon^{+}\hat{c}^{+} - \epsilon^{-}\hat{c}^{-})$$

where $\chi \equiv l^{+} + l^{-}$ and $\vec{\delta}_0 \equiv \vec{c}_0^{+} - \vec{c}_0^{-}$.

Using $\hat{\tau}^{\pm} \cdot \hat{h}^{\pm} = \cos\psi^{\pm}$,

$$\begin{aligned} \hat{h}^{+} \cdot (\vec{\delta}_0 + \epsilon^{+}\hat{c}^{+} - \epsilon^{-}\hat{c}^{-}) &= \chi\cos\psi^{+} \\ \hat{h}^{-} \cdot (\vec{\delta}_0 + \epsilon^{+}\hat{c}^{+} - \epsilon^{-}\hat{c}^{-}) &= -\chi\cos\psi^{-} \end{aligned}$$

ϵ^{+} and ϵ^{-} can be written as a function of χ.

$$\epsilon^{+}(\hat{h}^{+} \times \hat{h}^{-}) \cdot (\hat{c}^{+} \times \hat{c}^{-}) + (\hat{h}^{+} \times \hat{h}^{-}) \cdot (\vec{\delta}_0 \times \hat{c}^{-}) = \chi\vec{H} \cdot \hat{c}^{-}$$
$$\epsilon^{-}(\hat{h}^{+} \times \hat{h}^{-}) \cdot (\hat{c}^{+} \times \hat{c}^{-}) + (\hat{h}^{+} \times \hat{h}^{-}) \cdot (\vec{\delta}_0 \times \hat{c}^{+}) = \chi\vec{H} \cdot \hat{c}^{+}$$

where $\vec{H} \equiv \hat{h}^+ \cos\psi^- + \hat{h}^- \cos\psi^+$.

Introducing 4 constants, $a^\pm$ and $b^\pm$, and defining $\vec{h}_\perp \equiv \hat{h}^+ \times \hat{h}^-$, $\vec{c}_\perp \equiv \hat{c}^+ \times \hat{c}^-$, ϵ^+ and ϵ^- can be written:

$$\epsilon^+ = a^+\chi - b^+$$
$$\epsilon^- = a^-\chi - b^-$$

where, $a^\pm = \vec{H} \cdot \hat{c}^\mp / \vec{h}_\perp \cdot \vec{c}_\perp$ and $b^\pm = \vec{h}_\perp \cdot (\vec{\delta}_0 \times \hat{c}^\mp)/\vec{h}_\perp \cdot \vec{c}_\perp$. Finally we get by substitution of ϵ^+ and ϵ^-,

$$\boxed{\chi\hat{\tau} = \chi\vec{A}_c + \vec{D}_c}$$

where, $\vec{A}_c = a^+\hat{c}^+ - a^-\hat{c}^-$, $\vec{D}_c = \vec{\delta}_0 - (b^+\hat{c}^+ - b^-\hat{c}^-)$. $\vec{A}_c$ and $\vec{D}_c$ are $\vec{A}_c = \vec{H} \times \vec{c}_\perp / \vec{h}_\perp \cdot \vec{c}_\perp$ and $\vec{D}_c = (\vec{c}_\perp \cdot \vec{\delta}_0)\vec{h}_\perp / \vec{h}_\perp \cdot \vec{c}_\perp$

Appendix F

Calculation of the Errors in Direction Vectors

The hadron 4 momenta are obtained by summing the 4 momenta of the charged tracks and the neutrals:

$$h^\mu = \sum c^\mu + \gamma^\mu$$

Then the covariant error matrix of the hadron is also obtained by summing the contributions of the errors corresponding to c^μ and γ^μ:

$$\sigma_h = \sum \sigma_c + \sigma_\gamma$$

where the covariant error matrix (3×3) has the form of

$$\sigma = \begin{pmatrix} S_{xx} & S_{xy} & S_{xz} \\ S_{yx} & S_{yy} & S_{yz} \\ S_{zx} & S_{zy} & S_{zz} \end{pmatrix}$$

or has the form of (4×4) including the components for the energy measurement.

For a charged track, the 4-momenta and the error matrix are determined by the helix fitting and giving the mass hypothesis.

F.1 Calculation of momentum and covariant error matrix of a neutral track

Assuming the photon originates from the interaction region, we measure the angles, θ, ϕ, and the deposited energy E. Then the momentum of the photon is

$$\vec{\gamma} = (E\sin\theta\cos\phi, E\sin\theta\sin\phi, E\cos\theta)$$

The elements of the covariant error matrix for the neutral track are obtained from the typical errors on θ, ϕ, and E: $\sigma_E \sim 0.01E + 0.18\sqrt{E}$, $\sigma_\phi \sim (0.32 + 2.7/\sqrt{E}) \times 10^{-3}$, and $\sigma_\theta \sim \sigma_\phi \sin\theta$:

$$\begin{aligned}
S_{xx} &= (\sin\theta\cos\phi)^2\sigma_E^2 + E^2((\cos\theta\cos\phi)^2\sigma_\theta^2 + (\sin\theta\sin\phi)^2\sigma_\phi^2) \\
S_{yy} &= (\sin\theta\sin\phi)^2\sigma_E^2 + E^2((\cos\theta\sin\phi)^2\sigma_\theta^2 + (\sin\theta\cos\phi)^2\sigma_\phi^2) \\
S_{zz} &= \cos\theta^2\sigma_E^2 + E^2\sin\theta^2\sigma_\theta^2 \\
S_{xy} &= \cos\phi\sin\phi(\sin\theta^2\sigma_E^2 + E^2(\cos\theta^2\sigma_\theta^2 - \sin\theta^2\sigma_\phi^2)) \\
S_{yz} &= \cos\theta\sin\theta\sin\phi(\sigma_E^2 - E^2\sigma_\theta^2) \\
S_{zx} &= \cos\theta\sin\theta\cos\phi(\sigma_E^2 - E^2\sigma_\theta^2) \\
S_{yx} &= S_{xy}, S_{zy} = S_{yz}, S_{xz} = S_{zx}
\end{aligned}$$

F.2 Calculation of error on ζ

We defined ζ as an angular distance between cones as (Fig. F.1)

$$\zeta = 2MAX(\xi, \psi^+, \psi^-) - (\xi + \psi^+ + \psi^-)$$

Assuming that there is no explicit dependences of the error components in ξ on $\psi^\pm$, the variance of the angular distance ζ is

$$\sigma_\zeta = \sigma_\xi \oplus \sigma_\psi^+ \oplus \sigma_\psi^-$$

where $\sigma_\xi = \sigma_{\cos\xi}/\sin\xi$ and $\sigma_{\psi^\pm} = \sigma_{\cos\psi^\pm}/\sin\psi^\pm$.

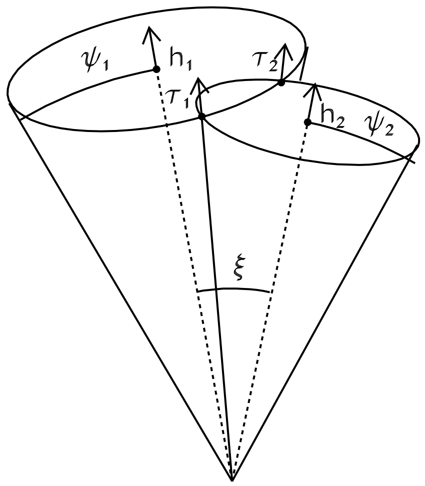

Figure F.1: Definition of ζ, ξ, and $\psi^{\pm}$

F.2.1 Calculation of error on ψ

The tau decay angle (ψ) in the hadronic decay mode can be obtained from 2 body kinematics:

$$\cos\psi = \frac{2E_\tau E_h - m_\tau^2 - m_h^2}{2P_\tau P_h}$$

where P, E, and m denote the momentum, energy, and mass of tau or hadron.

The components of derivatives, $\Delta_{1,2,3,4} \equiv \partial\cos\psi/\partial P_{1,2,3,4}$ where $P = (P_x, P_y, P_z, E_h)$ and $P_h = \sqrt{P_x^2 + P_y^2 + P_z^2}$, are

$$\Delta_i = \begin{pmatrix} (\frac{1}{P_\tau} - \frac{\cos\psi}{P_h})\frac{P_x}{P_h} \\ (\frac{1}{P_\tau} - \frac{\cos\psi}{P_h})\frac{P_y}{P_h} \\ (\frac{1}{P_\tau} - \frac{\cos\psi}{P_h})\frac{P_z}{P_h} \\ \frac{E_\tau - E_h}{P_\tau P_h} \end{pmatrix}$$

and the errors on $\cos\psi$ is

$$\sigma^2_{\cos\psi} = \sum_{i=1}^{4} \Delta_i^T \sigma_h \Delta_i$$

F.3 Calculation of error on ξ

Let us denote the momenta of hadrons, h_1 and h_2, as $\vec{p} = (p_x, p_y, p_z)$ and $\vec{q} = (q_x, q_y, q_z)$. Then the cosine of the angle between the two hadrons (ξ) is

$$\cos\xi = \vec{p}\cdot\vec{q}/|p||q|$$

The components of derivatives, $\Delta_{1,2,3} \equiv \partial\cos\xi/\partial p_{1,2,3}$ and $\Delta_{4,5,6} \equiv \partial\cos\xi/\partial q_{1,2,3}$, are

$$\Delta_i = \left(\begin{array}{c} \frac{1}{qp^3}[q_x(p_y^2 + p_z^2) - p_x(p_y q_y + p_z q_z)] \\ \\ \frac{1}{qp^3}[q_y(p_z^2 + p_x^2) - p_y(p_z q_z + p_x q_x)] \\ \\ \frac{1}{qp^3}[q_z(p_x^2 + p_y^2) - p_z(p_x q_x + p_y q_y)] \\ \\ \frac{1}{pq^3}[p_x(q_y^2 + q_z^2) - q_x(q_y p_y + q_z p_z)] \\ \\ \frac{1}{pq^3}[p_y(q_z^2 + q_x^2) - q_y(q_z p_z + q_x p_x)] \\ \\ \frac{1}{pq^3}[p_z(q_x^2 + q_y^2) - q_z(q_x p_x + q_y p_y)] \\ \end{array} \right)$$

Then, the error on the angle ξ is

$$\sigma^2_{\cos\xi} = \sum_{i=1}^{6} \Delta_i^T \left(\begin{array}{cc} \sigma_{h_1} & 0 \\ 0 & \sigma_{h_2} \end{array} \right) \Delta_i$$

Appendix G

3DIP Likelihood Function

G.1 Derivatives of the likelihood density function

The gaussian convolved double-exponetial function is

$$F(\delta, \alpha^{+}, \alpha^{-}, \sigma) = \frac{1}{2(\lambda_{+} - \lambda_{-})} e^{-\frac{\delta^2}{2\sigma^2}} (s_{+} e^{Q_{+}^2} \mathrm{erfc}(Q_{+}) - s_{-} e^{Q_{-}^2} \mathrm{erfc}(Q_{-})) \tag{G.1}$$

where $s_{\pm}$ are the signs of $\lambda^{\pm}$ and $Q_{\pm} = \frac{s_{\pm}}{\sqrt{2}}(\frac{\sigma}{\lambda_{\pm}} - \frac{\delta}{\sigma})$. To simplify the equations, we denote $A_{\pm} \equiv \frac{s_{\pm}\sigma}{\sqrt{2}\lambda}$ and $\lambda = l\alpha$.

This can be rewritten as $F = f^{+} - f^{-}$ by defining;

$$f^{\pm} = f_0^{\pm} e^{-\frac{\delta^2}{2\sigma^2}} e^{Q_{\pm}^2} \mathrm{erfc}(Q_{\pm}) \tag{G.2}$$

where,$f_0^{\pm} \equiv \frac{s_{\pm}}{2(\lambda_{+} - \lambda_{-})}$.

The derivatives of $\ln \mathcal{L} = \sum \ln F$ are

$$\begin{aligned} (\ln \mathcal{L})' &= \sum \frac{1}{F} F' = \sum \frac{f'_{+} - f'_{-}}{f^{+} - f^{-}} = \sum \frac{F'}{F} \\ (\ln \mathcal{L})'' &= \sum \frac{f''_{+} - f''_{-}}{f^{+} - f^{-}} + (\frac{F'}{F})^2 \end{aligned}$$

The first and second derivatives of f with respect to l are;

$$\frac{\partial f}{\partial l} = f_0 e^{-\frac{\delta^2}{2\sigma^2}} [e^{Q^2} \mathrm{erfc}(Q)(\frac{\delta}{l} - \frac{\sigma^2}{\lambda^2} - 1) + \frac{2}{\sqrt{\pi}} A] \times \frac{1}{l} \tag{G.3}$$

$$\frac{\partial^2 f}{\partial l^2} = f_0 e^{-\frac{\delta^2}{2\sigma^2}}[e^{Q^2}\mathrm{erfc}(Q)(2QA(1+2A^2-\frac{\delta}{\lambda})+(8A^2-3\frac{\delta}{\lambda}+2) \quad \text{(G.4)}$$
$$-\frac{2}{\sqrt{\pi}}A(\frac{\delta}{\lambda}-2A^2-4)] \times \frac{1}{l^2}$$

The first and second derivatives of f with respect to κ are;

$$\frac{\partial f}{\partial \kappa} = f_0 e^{-\frac{\delta^2}{2\sigma^2}}[e^{Q^2}\mathrm{erfc}(Q)\frac{\sigma^2}{\lambda^2} - \frac{2}{\sqrt{\pi}}\tilde{Q}] \times \frac{1}{\kappa} \quad \text{(G.5)}$$
$$\frac{\partial^2 f}{\partial \kappa^2} = f_0 e^{-\frac{\delta^2}{2\sigma^2}}[e^{Q^2}\mathrm{erfc}(Q)(\frac{\sigma^4}{\lambda^4}+\frac{\sigma^2}{\lambda^2}) - \frac{2}{\sqrt{\pi}}(\tilde{Q}(\frac{\sigma^2}{\lambda^2}+\frac{\delta^2}{\sigma^2}-1)+Q)] \times \frac{1}{\kappa^2} \quad \text{(G.6)}$$

G.2 Integration of the likelihood density function

The integration, $Int = \int_{\delta'=\delta}^{\infty} \mathcal{F}(\delta)d\delta'$, gives the likelihood probability as follow:

$$P(\mathcal{F}) = 1 - 2|Int - \frac{1}{2}|$$

The integral, Int, is:

$$\begin{aligned} Int &= \int_{\delta'=\delta}^{\infty} \mathcal{F}(\delta)d\delta' \\ &= \frac{1}{2(\lambda_+ - \lambda_-)}[(\lambda_+ - \lambda_-)\mathrm{erfc}(\frac{1}{\sqrt{2}}\frac{\delta}{\sigma}) \\ &\quad + e^{-\frac{\delta^2}{2\sigma^2}}(s_+\lambda_+ e^{Q_+^2}\mathrm{erfc}(Q_+) - s_+\lambda_+ e^{Q_+^2}\mathrm{erfc}(Q_+))] \end{aligned}$$

The P(F) uniformly distributes from 0 to 1.

Bibliography

[♣] Preface

[1] Y.-S. Tsai, *"Decay Correlations of Heavy Leptons in $e^+ + e^- \to l^+ + l^-$"*, Phys. Rev. D4, 2821 (1971)

[2] M. L. Perl, *"The Discovery of the Tau and its Major Properties: 1970-1985"*, Proceeding of the 1st Workshop on the Tau Lepton Physics at Orsay, 3 (1990)

[3] M. Davier, *"Review of lifetime, leptonic B.R. and Michel parameters"*, talk given in the 3rd Workshop on Tau Lepton Physics, Montreux, 1994

[♣] Chap. 1

[4] V. Barger & R. Phillips, *"Collider Physics"*, Addison-Wesley, 1987

[5] F. Halzen & A. D. Martin, *"Quarks & Leptons"*, John Wiley & Sons, 1984

[6] J. Lefrançois, *"Precision tests of the Standard Model. The experimental results"*, ALEPH 93-180, PHYSIC 93-155

[7] talk given by Andrei Kounine, *"Review of neutral couplings"*, 3rd Workshop on Tau Lepton Physics, at Montreux, Sep. 1994

[8] E. Blusher, *"Properties of the τ lepton"*, ALEPH 92-151, PHYSIC 92-139

[9] R. Brandelik et al., *"Measurements of Tau Decay Modes and a Precise Determination of the Mass"*, Phys. Lett. 73B, 109 (1978)

[10] W. Bacino et al., *"Measurements of the Threshold Behavior of $\tau^+\tau^-$ Production in e^+e^- Annihilation"*, Phys. Rev. Lett. 41, 13 (1978)

[11] J. Z. Bai et al., SLAC-PUB-5870, 1992

[12] Z. Zhang, *"Study of tau lepton decays with the ALEPH detector at LEP"*, thesis, Universite de Paris Sud, 1992

[13] R. Alemany & M. Davier, *"Tau Hadronic Branching Ratios"*, ALEPH 94-148, PHYSIC 94-128

[14] T. N. Truong, *"Hadronic τ Decay, Pion Radiative Decay, and Pion Polarizability"*, Phys. Rev. D30, 1509 (1984)

[15] F. J. Gilman and S. H. Rie, *"Calculation of Exclusive Decay Modes of the Tau"*, Phys. Rev. D31, 1066 (1985)

[16] G. J. Feldmann et al., *"Measurement of the τ lifetime"*, Phys. Rev. Lett. 48, 66 (1982)

[17] C. Bebek et al., *"Measurement of the Tau Lifetime"*, Phys. Rev. 36, 690

[18] W. T. Ford et al., *"Lifetime of the Tau Lepton"*, Phys. Rev. Lett. 49, 106 (1982)

[19] H.-J. Behrend et al., *"Measurements of the τ Lifetime"*, Nucl. Phys. B211, 369 (1983)

[20] The ALEPH Collaboration, *"Measurement of the Tau Lifetime"*, Phys. Lett. B 279, 411-421 (1992)

[21] The ALEPH Collaboration, *"A precise measurement of the τ lifetime"*, Phys. Lett. B 297, 432-448 (1992)

[22] talk given by Michel Davier, *"Summary talk"*, 2nd Workshop on Tau Lepton Physics, at Ohio, Sep. 1992, and references herein

[♣] Chap. 2

[23] W. Brum, *"The ALEPH Handbook"*, ALEPH 89-077, NOTE 89-003

[24] The ALEPH Collaboration, *"Performance of the ALEPH detector at LEP"*, CERN-PPE/94-170, 1994

[25] The ALEPH Collaboration, *"ALEPH: A Detector for Electron-Positron Annihilations at LEP"*, CERN-EP/90-25, 1990

[26] D. Schlatter & G. Redlinger, *"$\aleph$ in Numbers"*

[27] T. Lohse & W. Witzeling, *"The Time Projection Chamber"*, ALEPH 91-156, TPC-GEN 91-005

[28] W. B. Atwood et al., *"Performance of the ALEPH Time Projection Chamber"*, ALEPH 91-20, TPCGEN 91-01

[29] P. S. Marrocchesi et al., *"The spatial resolution of the ALEPH TPC"*, ALEPH 90-10, TPCGEN 90-02

[30] D. Colling & B. Wolf, *"First results of the ITC/TPC Alignment from the 1991 Cosmics Run"*, ALEPH 91-065, TPCGEN 91-002

[31] *"Letter of Intent to Study e^+e^- Annihilation Phenomena at LEP"*, CERN-LEP-LI(1), 1982

[32] A. Schwart, *"Silicon Strip Vertex Detectors at Z^0 Factories"*, ALEPH 92-097, MINIV 92-003

[33] L. Bosisio et at., *"ALEPH Minivertex Detector - Update of the design"*, ALEPH 84-130

[34] A. Bonissent & J. Carr & J. Drinkard, *"Searching for the origin of VDET pattern recognition errors using Monte Carlo truth"*, ALEPH 93-023, MINIV 93-001

[35] R. Della Marina, *"Study of Pattern Recognition in the $\tau \to 3\pi\nu$ events"*, ALEPH 92-022, PHYSIC 99-019

[♣] Chap. 3

[36] L. Duflot, *"Nouvelle méthode de mesure de la polarisation du τ. Application au canal $\tau \to a_1\nu_\tau$ dans l'expérience ALEPH"*, LAL 93-09, Thesis, 1993

[37] G. Ganis & L. Duflot & F. Le Diberder, *"New selection for $e^+e^- \to \tau^+\tau^-$ events"*, ALEPH 92-142, PHYSIC 92-130

[38] G. Ganis & M. Girone & L. Rolandi, *"Improved $Z \to \tau^+\tau^-$ selection"*, ALEPH 93-184, PHYSIC 92-159

[39] G. Ganis & M. Girone & L. Rolandi, *"TSLT01 selection efficiency on 92 Monte Carlo events"*, ALEPH 94-31, PHYSIC 94-27

[40] G. Ganis & M. Girone & L. Rolandi, *"Measurement of $\sigma_{\tau^+\tau^-}$ ans $\mathcal{A}_{FB}^{\tau^+\tau^-}$ with 92 data"*, ALEPH 94-31, PHYSIC 94-27

[41] G. Ganis & M. Girone & A. Gregorio, *"Study of the background in the $\tau^+\tau^-$ event selection"*, ALEPH 94-182, PHYSIC 94-154

[42] M. Davier & Z. Zhang, *"Particle Identification For Tau Physics"*, ALEPH 91-093, PHYSIC 91-085

[43] Z. Zhang, *"Study of tau lepton decays with the ALEPH detector at LEP"*, LAL 92-15, Thesis, 1992

[44] R. Alemany et al., *"TOPCLAS"*, ALEPH note in preparation

[45] S. Jadach & B. F. L. Ward & Z. Was, *"The Monte Carlo program KORALZ, version 3.8, for the lepton or quark pair production at LEP/SLC energies"*, CERN-TH-5994/91, 1991

[♣] Chap. 4

[46] Harris Kagan, *"Present Status and Future Prospects of Precision Measurements of τ Lifetime."*, 1st Workshop on Tau Lepton Physics, at Orsay, Sep. 1990

[47] Ll. M. Mir & S. Orteu, *"Measurement of the Tau Lifetime"*, ALEPH 91-141, PHYSIC 91-124

[48] M. Carpinelli & A. Ciocci & I. Ferrante & F. Fidecaro, *"Tau lifetime with the decay length method using VDET"*, ALEPH 92-25, PHYSIC 92-22

[49] S. Wasserbaech, *"The lifetime of the τ lepton"*, ALEPH 91-140, PHYSIC 91-123

[50] S. Wasserbaech, *"Measurement of the τ lifetime using the Impact Parameter Difference method: 1991 Data with VDET"*, ALEPH 92-73, PHYSIC 92-64

[51] S. Wasserbaech, *"Measurement of the τ lifetime using the Impact Parameter Difference method: 1991 Data with VDET"*, ALEPH 92-73, PHYSIC 92-64

[52] M. Carpinelli, A. Ciocci, I. Ferrante, F. Fidecaro, A. Messineo, *"Using the sum of Impact Parameter to measure the τ lifetime"*, ALEPH 92-27, PHYSIC 92-24

[53] F. Fidecaro, A. Lusiani, A. Messineo, A. Sciaba *"Measurement of the τ lifetime with the Impact Parameter Sum method, using the 1992 ALEPH data sample"*, ALEPH 94-115, PHYSIC 94-100

[54] Hwi Yong Kim, *"Tau Lifetime with Momentum-dependent Impact Parameter Sum Method: 1992 data"*, ALEPH 94-050, PHYSIC 94-048

[55] talk given by Steven Wasserbaech, *"A precise measurement of the τ lepton lifetime"*, 2nd Workshop on Tau Lepton Physics, at Ohio, Sep. 1992

[56] talk given by William Trischuk, *"DELPHI τ lifetime measurement"*, 2nd Workshop on Tau Lepton Physics, at Ohio, Sep. 1992

[57] talk given by M. P. Yzerman, *"L3 tau lifetime measurement from 1991 data"*, 2nd Workshop on Tau Lepton Physics, at Ohio, Sep. 1992

[58] talk given by Paul Weber, *"Tau lifetime measurements using the OPAL detector at LEP"*, 2nd Workshop on Tau Lepton Physics, at Ohio, Sep. 1992

[59] talk given by Richard Kass, *"A measurement of tau lepton lifetime"*, 2nd Workshop on Tau Lepton Physics, at Ohio, Sep. 1992

[60] talk given by Isidoro Ferrante, *"Tau lifetime in ALEPH"*, 3rd Workshop on Tau Lepton Physics, at Montreux, Sep. 1994

[61] talk given by Attilio Andreazza, *"Tau lifetime in DELPHI"*, 3rd Workshop on Tau Lepton Physics, at Montreux, Sep. 1994

[62] talk given by Maurizio Biasini, *"Tau lifetime in L3"*, 3rd Workshop on Tau Lepton Physics, at Montreux, Sep. 1994

[63] talk given by Catriona Charlesworth, *"Tau lifetime in OPAL"*, 3rd Workshop on Tau Lepton Physics, at Montreux, Sep. 1994

[64] talk given by Christopher White, *"Tau lifetime in CLEO"*, 3rd Workshop on Tau Lepton Physics, at Montreux, Sep. 1994

[♣] Chap. 5

[65] G. Giannini, B. Gobbo & L. Pitis, *"A 3-D reconstruction of tau decay points"*, ALEPH 93-79, PHYSIC 93-65

[66] J.H. Kuhn, *"Tau Kinematics from Impact Parameter"*, TTP93-14, May 1993

[♣] Chap. 9

[67] talk given by Michel Davier, *"Review of lifetime, leptonic branching ratio, and Michel parameters"*, 3rd Workshop on Tau Lepton Physics, at Montreux, Sep. 1994

[♣] Miscellaneous

[68] J. Knobloch & P. Norton, *"Status of Reconstruction Algorithms for ALEPH"*, ALEPH 88-046, NOTE 88-006

[69] D. Brown & G. Redlinger, *"1991 Beam Spot and Beam Envelope measurement"*, ALEPH 92-008, PHYSIC 92-008

[70] G. P. Yost, *"Maximum Likelihood Approach to Lifetime Estimation in the Presence of Large Experimental Errors"*, Nucl. Inst. & Meth. 224(1984) 489-507